# Ice-structure Interaction Analysis: Inverse Ice Force Prediction for Stiffened Plate and Dynamic Simulation

by

Yuxi Zhang

A dissertation submitted in partial fulfillment
of the requirements for the degree of
Doctor of Philosophy
(Naval Architecture and Marine Engineering)
in the University of Michigan
2018

Doctoral Committee:

      Associate Professor Dale G. Karr, Chair
      Associate Professor Matthew D Collette
      Professor Sherif El-Tawil
      Professor Nickolas Vlahopoulos

Yuxi Zhang

yuxiz@umich.edu

ORCID iD: 0000-0002-6576-5413

For my parents, who give me possibilities and love.

## Acknowledgements

On a sunny afternoon at the bench outside NA&ME department, I was kind of frustrated and lost about my future career paths, though frustration is normal for research struggling. "It is not about training," Prof. Karr said to me, "it is all about education".

This lightened my day. It is not because that I felt finally competent to do whatever I would like, but that I felt the strength and responsibility to be whom I am, and to trust deeply in myself and in the scientific process of the education journey. Weirdly, I did not favor less about research after that, my interest for mathematical derivation for stiffened plates and for the finite element analysis grows stronger. The *unseen* parts of research lie in the awakening of the courage to overcome any difficulties and challenges, the process to look at things differently, the enjoyment of the enlightenment of learning, the possibilities to seek facts for improvements, and the goal to understand one single problem to better bridge to a bigger world.

I sincerely feel thankful for my adviser, Prof. Dale G. Karr. For his guidance through my academic path with his great patience, wisdom and insights through my 5-year Ph.D study. We started the research journey from an independent study on the mathematical Matlock's dynamic ice-structure interaction model. Now working back on this model for validation, I still found it challenging and interesting and of course, a lot of improvement to be done. I am thankful to my dear committee members, Prof. Nick Vlahopoulos, Prof. Matthew Collette and Prof. Sherif El-Tawil. For your valuable inputs and for your intellectually intriguing discussion to help me see deeper insights of the research. I would like to thank Prof. Armin Troesch for being point of reference for my application for Link Foundation fellowship. I would also like to thank Dr. Lin Van Nieuwstadt, and Dr. Roger De Roo for the cooperation on my very first DoE sponsored project, which was challenging and fun as an interdisciplinary 3-year project.

# Table of Contents

# CHAPTER 4

# CHAPTER 5

# CHAPTER 6

# List of Tables

# List of Figures

# List of Appendices

# ABSTRACT

Offshore regions of the Arctic and the Great Lakes hold valuable resources in many respects for harvesting energy and serving as important shipping lanes. Ice loading poses a threat to structures in these regions with high local pressure and various failure modes. It is thus essential to evaluate the ice peak loadings using limited and site-specific data. This thesis aims to better predict the peak ice loading by developing an efficient inverse ice loading prediction methodology and accurate stiffened plate analysis for marine structure design. Additionally, the behavior of the ice-structure interaction is studied mathematically to understand the cyclic dynamic ice-loading applied on offshore structures during continuous ice crushing.

Multiple inverse algorithms are presented for calculating the variable ice pressure acting on a stiffened steel plate. The analytical models are formulated to calculate the quasi-static pressure caused by contact of lake ice driven primarily by thermal expansion and winds. Loading pressures are calculated using strain measurements from a stiffened plate installed on a Keweenaw Peninsula lighthouse in Lake Superior. The ice sheet was essentially stationary through the winter months. The linear relationships between pressure and strain values are obtained by both strip beam theory and orthotropic plate theory. The inverse solutions are by nature not necessarily unique. Two inverse approaches using orthotropic plate theory show results with satisfying accuracy and efficiency compared to the finite element analysis. In addition, laboratory calibration and an examination using the recorded data from field measurements exhibit the effectiveness of the presented approach.

Continuous ice brittle crushing occurs in the movement of an ice sheet against an offshore structure. Matlock's ice-structure interaction model is used to simulate the behavior of the ice crushing by modeling ice teeth indentation contacting a spring-mass-dashpot structure. The dynamic behavior of the model is studied using Fourier analysis to predict the response of specific periodicity. The time histories of tooth deflections are expressed through non-linear dynamic equations. The kinematic initial conditions can be predicted at targeted periodicity via the Fourier analysis. Given a representative offshore wind tower system, the first mode shape of the physical system is calculated as input for the ice-structure interaction model as an extended validation. The amplitudes of the structural dynamic vibrations predicted by the analytical model at specific periodicity are compared to the mathematical numerical simulations.

A discrete energy method is applied to accurately calculate the deformation of either unidirectional or cross-gridded stiffened panels. This approach obtains the strain energy of the plate and stiffeners using double Fourier series for the displacement fields. Two models are described assuming different reference planes. The first model presumes that the reference planes are located at the effective centroids which are calculated from the cross-sectional properties. The second model formulates the in-plane displacement fields at the mid-plane of the plate. The plate is simply supported along all four edges at the effective centroids for the first model, and at the mid-plane of the plate for the second model. Both methods accurately capture the deformations between stiffeners and the second model eliminates the complicated calculation for effective breadth which is an unavoidable effort for stiffened plate analysis using conventional orthotropic

plate theory. The methods presented provide efficient design tools and can be applied to light weight structural design in various fields.

<div align="center">

Chapter 1

**Introduction**

</div>

## 1.1    Motivation

Offshore regions of the Arctic and the Great Lakes hold valuable resources in many respects for harvesting energy and serving as important shipping lanes. Ice loading poses a threat to structures in these regions; it is thus essential to evaluate the ice peak loadings using limited and site-specific data (Fig. 1.1). Researchers have termed local ice pressure as "high-pressure zones" (Jordaan, 2000) or "line-like loads" (Riska and Kämäräinen, 2011) with multiple formulations to predict the high local ice pressures. Croasdale et al (1977) carried out indentation tests to investigate maximum ice pressures on vertical piers in the Arctic area at low strain rate. It is concluded that the laboratory tested ice results in a higher strength of ice compared to the field measured ice property. Sanderson (1988) observed that global ice pressures are significantly lower than local ice pressures during ice crushing events; Palmer et al. (2009) developed an ice-pressure to ice contact area curve to address this issue.

**Figure 1.1:** Photograph of the Molikpaq in the Canadian Beaufort Sea covered with ice (Timco and Johnston, 2003)
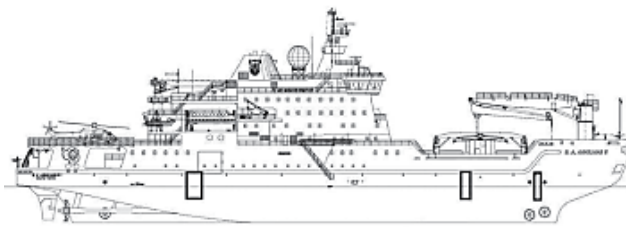


(a)
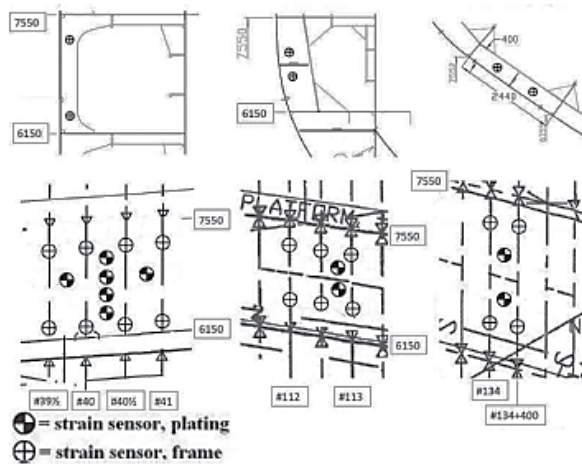


(b)

**Figure 1.2: (a):** Instrumented areas of hull indicated with black boxes for the Polar Supply and Research Vessel (PSRV) S.A. Agulhas II; **(b):** Instrumentation of the frames and hull plating at the bow (on the right), bow shoulder (in the middle), and stern shoulder (on the left) (Suominen et al., 2013)

However, Suominen et al. (2013) discussed the knowledge of the load characteristics used by the classification societies (FSCR 2010, IACS 2011) comparing the measured ice loads to the design ice loads for PSRV S.A Agulhas II (Fig. 1.2) during March 2012. Also, Kim et al. (2016)

argued that the assumptions regarding the pressure-area relationship, ice edge spalling characteristics, dynamic viscosity and strength of crushing ice should be evaluated with further validation as the simplified models are referenced by classification rules. It is thus concluded by previous researchers that full-scale load measurements are needed to obtain more accurate descriptions of local ice loads (Jordaan 2000, Suominen et al. 2013, Kim et al. 2016).

Stiffened plates have been commonly used in various applications such as naval structures, and marine platforms as efficient light weight structures to reach maximum strength requirements. Examples of full-scale ice force measurements have been carried out on stiffened structures like offshore drilling platforms, framed ship scantlings etc. (Sodhi 2001, Timco and Johnston 2003, Suominen et al. 2013). Many previous investigations have been devoted to formulating the stiffened structure as structurally orthotropic plate using classical plate theory. Hoppman et al (1956) used an orthotropic formulation for analyzing simply supported orthogonally stiffened plates under static and dynamic loading. The calculated plate rigidities and stiffness compare well with the experimental results and it is argued that cross-contraction or Poison's effect is negligible for flexural deformation. However, the orthotropic models "smear" the effect of the stiffeners over the entire plate for simplified approximation. As is summarized by Ventsel and Krauthammer (2001), the orthotropic plate theory is considered applicable only to cases with closely spaced stiffeners. A novel analytical model for variously stiffened panels is needed for efficient and accurate process of marine structure design. Also, the success of obtaining an accurate structural model for stiffened panel would prominently improve the inverse ice prediction algorithms applied in full-scale ice-load measurements on stiffened frames.

## 1.2     Background on Ice Force Measurement and Ice-structure Interaction Analysis

While extensive research on ice-structure interaction has been conducted over the past several decades, much attention has focused on sea ice (Bjerkås 2006, Palmer and Croasdale, 2013). Bjerkås (2006) described several methods for measuring the full-scale ice forcing for first year ice in either arctic areas (Zone II) or sub-arctic areas (Zone I) as shown in Fig. 1.3. His research revealed the average peak ice pressures to be in the range of 0.6 to 1.8 MPa along the American shorelines. Riska and Kämäräinen (2011) reviewed the principles under the important Finnish-Swedish Ice Class Rules (FSICR) by investigating the design points and statistics of ice loads in the Baltic Sea. Ralph and Jordaan (2013) explored the probabilistic method for ships that navigate in the Arctic. Dempsey (2000) discussed the ice mechanics research development from geophysical scale and floe scale to structural scales for both sea ice and river ice. However, few records can be found for ice loadings on stiffened offshore structures in the Great Lakes area.

There are various ice-structure interaction modes with different ice failure modes depending on different ice indentation speed or strain rate. Sodhi (2001) observed three different modes of ice failure depending mainly on the indentation rate: ice fails from ductile deformation through "intermittent" crushing to brittle failure when the indentation rate increases from low to high. Jordaan (2001) described an ice-structure interaction model using a probabilistic approach and suggested that the high pressure zones appear most likely in the confined areas (Fig. 1.4). It is however pointed out by Jordaan (2001) that the measurements of ice loads, both local and global, in the full scale, demonstrate great randomness. While both Sodhi (2001) and Jordaan (2001) modeled ice structure interaction through elastic-brittle failure, other research addressed ice forces during impact in which the ice fails against the structure in dynamic fashions, often with the ice crushing or spalling against the structure or against a ship hull (Sodhi, 1991; Jordaan 2001;

4

Dempsey et al. 2001; Riska et al. 2002, Leira et al. 2009; Kim et al. 2015). The highly localized

pressures, found to be as high as 50 MPa by Joensuu and Riska (1989), and Riska (1991), develop

in line-like regions during indentation tests and during icebreaking experiments in which the ice

is crushed and pulverized. It is thus necessary to predict the peak ice loading and the cyclic

dynamic ice-structure interaction process during the ice crushing event.



**Figure 1.3:** The Northern hemisphere with three zones studied by researchers as the severity of ice conditions. (Bjerkås, 2006)
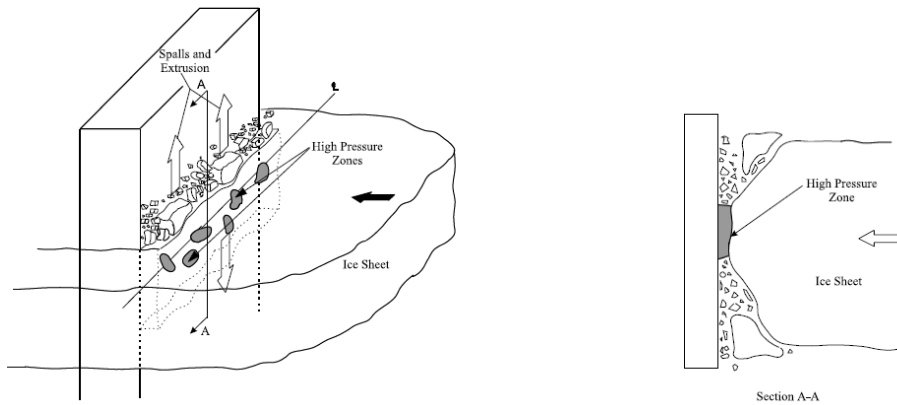


**Figure 1.4:** Schematic illustration of the main process of spalling, extrusion and high-pressure zone formation (Jordaan, 2001)

This present thesis has focused on forces occurring in freshwater ice in situations in which

the ice acts against the structure by wind and thermal forcing (IEC 61400-3-1, 2009) as part of the

Department of Energy (DoE) sponsored project with the installation of an Ice Force Measurement

System (IFMS) for the winter 2013 – 2014 in Lake Superior. Photographs were taken on a daily

basis throughout the winter season showing constant contact with the ice force measuring plate.

The structure's stiffness is extremely high relative to the ice so there is essentially no dynamic interaction in the usual sense of ice-structure interaction dynamics. At low velocities (0.005-0.01m/s), the ice fails in buckling and bending (Jordaan 2000; Bjerkås and Skiple, 2005; Ziemer and Ever, 2016). Because the ice strain rates are therefore very low and the ice is not fracturing or spalling, it is reasonably presumed the interface of the fast ice and the structure to be continuous through the width of the plate.

Driven by the need to evaluate the peak ice-loading in the Great Lakes area, hence freshwater ice as opposed to sea ice, and to develop efficient algorithms to accurately determine the ice force distributions, this thesis involves the development of cost-efficient analytical models to inversely predict ice-pressure distributions from the limited measurements of ice thickness and structural strains. The strain measurements were routinely collected at 1Hz and when high winds developed leading to increased forcing on the structure, data was collected at 5 Hz. The input measurements of the ice thickness and the strains used in the analysis discussed here are obtained from the stiffened panel deployed in Lake Superior. These results are considered to have practical applications for the design of Great Lakes structures such as for potential offshore wind turbine platform design. Design standards (e.g. IEC 2009, Tarp-Johansen et al. 2006) for such facilities require estimates for ice forcing from thermal expansion of and wind action on the surface ice.

## 1.3    Background on Stiffened Plate Analysis

The widely applied orthotropic plate theory for analysis of stiffened plate can yield inaccurate results for sparsely-stiffened plates. Eagle and Sewall (1968) considered stringers as discrete elements for study of the orthogonally stiffened cylindrical shells and found that the stringers couple the circumferential modes. It is noted that the mode shapes determined by their

discrete-stiffener approach can differ substantially from the harmonic mode shapes using traditional orthotropic plate analysis with an averaging effect from stiffeners.

Other methods of calculating the structural response of stiffened plates involves the evaluation of edge forces, effective breadth or effective width. Rigo (1992) applied the Fourier series expansion as an analytical solution for the stiffened sheathing with the improvement to allow spacing and dimension changes of ribs. This stiffened sheathing method requires edge forces and moments as the dynamic boundary conditions for the mathematical formulation. Wang and Rammerstorfer (1996) used a finite strip method to investigate both the effective breadth and the effective width. However, the coupling effect of Fourier terms in the stiffness matrices is observed to cause an extensive increase in computational effort. Sapountzaki and Katsikadelis (2001)'s analysis isolated the beams from the plate and established continuity conditions at the interface. The variation of the effective breadth may also require large computational effort which is not ideal in terms of a general ribbed plate analysis.

Some more advanced FEA models are developed through separate consideration of the plate and stiffener while maintaining compatibility (Mukherjee and Mukhopadhyay, 1987). Shi et al (2015) introduced a local coordinate system and employed the first order shear deformation theory to the finite element analysis of shell and beams, obtaining precise structural results for arbitrarily spaced stiffener distribution. Barik and Mukhopadhyay (2002) developed a four-nodded stiffened plate element to model arbitrary shaped plates without the disadvantage of shear-locking phenomena. More research works have been carried out to achieve accurate structural behavior through discrete treatment of stiffeners and the plates. Samanta and Mukhopadhyay (2003) derived a stiffened shell element by modeling the stiffeners as discrete elements to allow various placement of stiffeners within the shell elements. Good correlation is found for this shell element with

improved accuracy by including the element's curvature and obviating its mesh grading restriction. However, the FEA modeling using shell element with discrete treatment of stiffener elements still require extensive modeling, which may not be ideal compared to an efficient analytical solution, particularly at the structure design stage.

## 1.4    Contributions

The thesis aims at developing an efficient inverse ice loading prediction algorithm to effectively reflect the variable ice loading from limited and site specific experimental measured data in Great Lakes area. Also, the dynamic ice-structure interaction is studied using Matlock's model to predict the cyclic ice-loading applied on offshore structures during continuous ice crushing. As an extended study from the inverse ice loading algorithm development, an efficient and more accurate analytical model is established using discrete energy method to evaluate the structural response of variously stiffened plate as they are applied in marine structures.

The first contribution of the thesis is the development of multiple inverse ice-loading prediction algorithms that well reflect the peak ice pressure among the variable quasi-static ice loading on offshore structure using strain gage measurements, with or without the input of ice-thickness:

- In the effort to reflect the variability of the ice-forcing, the plate is formulated as a structurally equivalent orthotropic plate in two models: OPT I OPT II. OPT II incorporates the input of ice-thickness and constrains the ice loading area to be within the ice-covered patch on the structure. OPT II is notable for its faster convergence, especially when the ice-covered area is comparatively thin.

- The inverse counterpart of OPT II is stabilized through a Truncated Singular Value Expansion (TSVE) optimization procedure, thus the stability of the matrix operation is retained.

- The strain gage data is measured by the IFMS instrumentation through the winter season 2013-2014 at Lake Superior: Maximum pressure forcing of 3.54 MPa is observed on May 01 by OPIT II calculation, while a peak average pressure about 0.90 MPa to 1.30 MPa were on April 17 and March 18, 2014. The results match well with the peak ice loads measured on lighthouses as are summarized by Bjerkås (2007) through different measuring programs.

Second contribution of the thesis lies in the prediction of the structural motion of amplitude for cyclic dynamic ice structure interaction using Matlock's model to simulate the continuous ice crushing as the common ice failure mode at a higher indentation speed:

- This approach establishes the non-linear dynamic equations through Fourier analysis with respect to the number of tooth-breakages, N per cycle. This method allows rapid estimation for the range of motion and the evaluation of structural contact forces.

- The amplitudes predicted by this Fourier analysis solution correspond well to the simulation results obtained from direct simulation solutions with various initial condition selections.

- The previously un-detected periodic response of a Periodic-4 is found through our Fourier solution. Furthermore, the time ratios of breakage are accurately predicted thus the cyclic behavior can be analyzed *a priori*.

Further contributions lie in the analyses of variously stiffened plates using Fourier series to accurately capture the deformation of the stiffened structure under two different boundary conditions:

- Two sub-models using discrete energy methods, abbreviated as DEM I and DEM II, are developed to predict the response of variously stiffened plates using the discrete

energy component method via Fourier series formulation with different assumptions of the neutral planes. DEM I is valid and efficient assuming the dominance of bending effect for plates with pinned ends. DEM II formulates the in-plane displacement fields at the mid-plane of the plate.

- Compared to DEM I, the DEM II captures the in-plane deformation caused by the Poisson's effects of contraction which is noticeable with various stiffening patterns. DEM II presents substantial accuracy improvement in prediction of either uni-directionally or orthogonally stiffened plates for stress evaluation.

- The improved efficiency and accuracy of formulating the displacement fields highlight the advantage of DEM I and DEM II in terms of design evaluation compared to traditional computationally expensive FEA analyses or orthotropic plate theory.

## 1.5    Dissertation Outline

This thesis reports the extensive research efforts on ice-structure interaction with focus on the inverse ice loading prediction, ice-structure interaction analyses and extended analytical analyses for stiffened panels.

**Chapter I** is an introduction. It summarizes the background on the different ice failure modes at different structure indentation speed. This chapter provides a literature review of ice-structure interaction and explains the scope of the thesis with respect to different ice failure modes and the extended focus on structural analysis of the stiffened plate.

**Chapter II** and **Chapter III** give detailed experimental set up information for Ice Force Measurement System (IFMS) and explain how the inverse algorithms as the counterpart of forward formulations, specifically OPIT I and OPIT II, are developed and compared well with FEA models. **Chapter III** incorporates the strain gage data measured in the experiments described in **Chapter II** and compares with historically observed peak ice load for first year ice in the lake areas.

Chapter IV is an extended study on the dynamic ice-structure interaction process to understand the continuous ice crushing failure using Fourier series analysis, while **Chapter II** and **Chapter III** studies the quasi-static ice loading for ice failing in creep and bending at low indentation speed. The ice crushing failure is modeled as the Matlock's spring mass dashpot system with a single degree of freedom by assuming continuous ice breakage and continuous ice contact with the structure. The cyclic behavior of a given system is predicted for its motions and amplitudes. The predicted results compare well with numerical simulation solution.

**Chapter V** presents a novel discrete energy method using Fourier series for stiffened plate analysis. This chapter serves as an extended study from **Chapter II** and **Chapter III** to prepare for future inverse load prediction on variously stiffened plates. DEM I and DEM II methods are developed based on different assumptions of reference planes and boundary conditions. Both DEM methods well reflect the deformation of the plate as an amendment over the smearing effect presented in classical orthotropic theory. The DEM II method is able to capture the in-plane Poison's effect with notably improved accuracy compared to DEM I.

**Chapter VII** draws the conclusions.

Chapter 2

## Ice Force Measurement System

## 2.1    Introduction for IFMS Experiment Set Up

The installation and operation of the Ice Force Measuring System (IFMS) were completed as a portion of Department of Energy sponsored project entitled "Measurement and Analysis of Extreme Wave and Ice Actions in the Great Lakes for Offshore Wind Platform Design." Instrumentation was deployed in Lake Superior on a Keweenaw Peninsula lighthouse, where a large-scale laboratory for cold regions engineering experimentation is naturally formed. A data acquisition system captured readings from strain gages encased in the IFMS plate and ice thicknesses were monitored from a radiometer located on the deck of the lighthouse (Fig. 2.1a and 2.1b). The physical dimensions of the IFMS plate with the numbering of ribs and the allocation of linear strain gages are sketched in Fig. 2.2a:  a=1.5 m is the depth of the plate defined along the vertical x-direction, b=0.6 m is the width of the plate along the horizontal y-direction. Nine stiffeners are evenly distributed from the top to the bottom of the plate and are sequentially numbered from #0 to #8. The vertical spacing of the two near stiffeners $t_1$ is 0.15 m. Also, the upper right unloaded zero strain gage $R_0$ is used to diminish temperature effect on the readings and determine the change of strains caused only by the effects of ice.
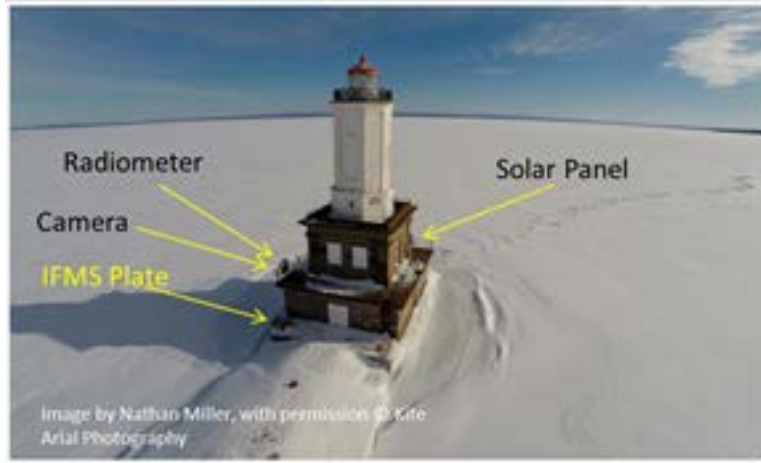
(a)
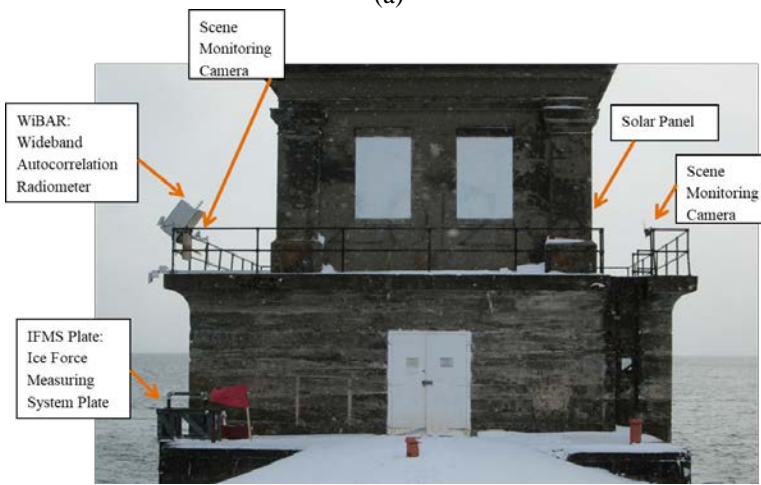


(b)
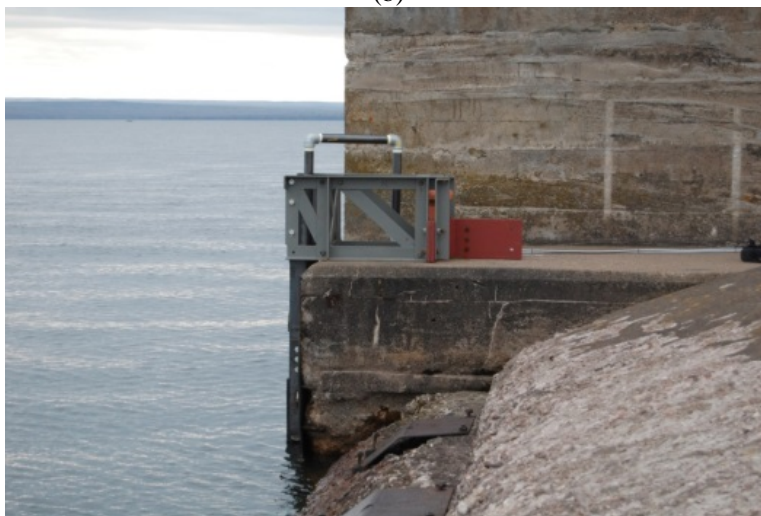


(c)

**Figure 2.1: (a)** South Portage Entry Lighthouse and deployment IFMS (image by Nathan Miller, with permission); **(b)** view of the Lighthouse looking south for the deployment of the instrumentation (image by Dr. Lin Van Nieuwstadt, with permission); **(c)** side view of the framing for the IFMS plate after installation (image by Dr. Lin Van Nieuwstadt, with permission)
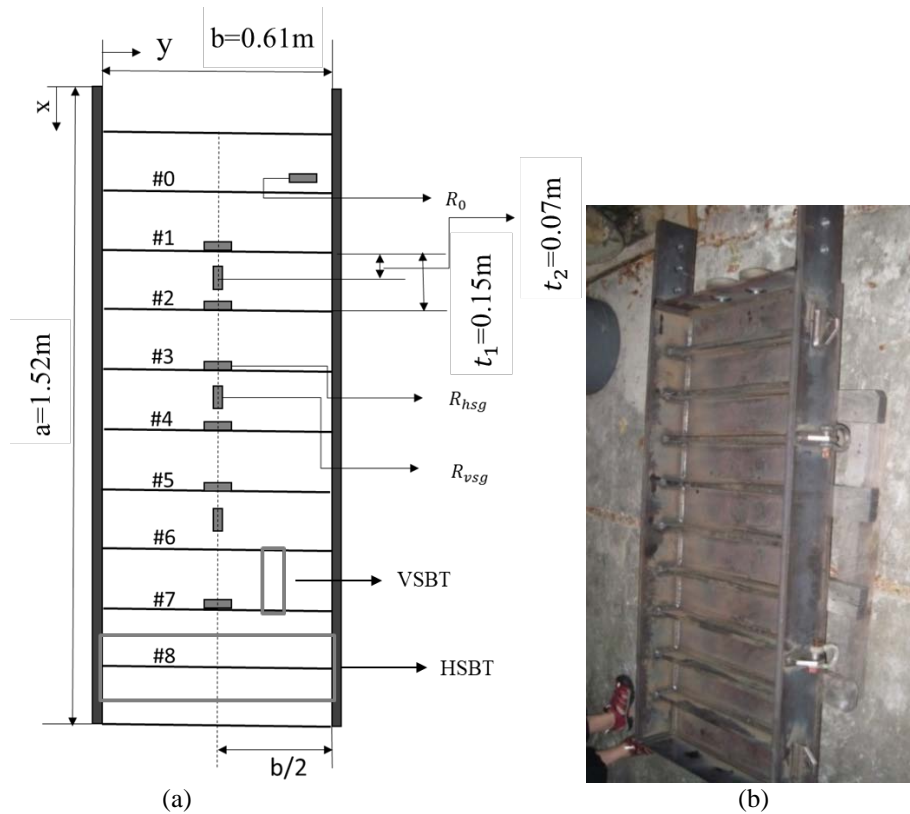
**Figure 2.2: (a)** Dimensions of the IFMS plate, arrangement of linear strain gages; **(b)** IFMS plate during strain gage installation (image by Dr. Lin Van Nieuwstadt, with permission)

The linear horizontal strain gages $R_{hsg}$ are located at the middle span of the ribs from rib #1 to rib #7. The vertical strain gages $R_{vsg}$ are located at the back of the face plate and are aligned through the vertical midline of the plate. The center of the vertical strain gage is located midway between stiffeners. The vertical boundaries of the IFMS face plate are constrained by two stiff steel side-bars as shown in Fig. 2.2b.

## 2.2 IFMS Pre-Testing at CEE Lab

Mechanical testing of the IFMS plate was undertaken for calibration and data acquisition verification prior to field deployment. The IFMS plate load test (without the back plate) was performed at the Civil and Environmental Engineering (CEE) Structural Engineering Laboratory

14

at the University of Michigan. The 14-inch diameter loading cylinder with a 14-inch square steel plate attached to the bottom of the cylinder was used (Fig. 2.3a). The IFMS face plate was loaded gradually from zero to 20 Kips in the first round. In the second round, the plate was reloaded at 5 Kip or 10 Kip per step until a maximum of 50 Kips. Considering the stiffness of the loading cylinder and the attached square plate, the contact area between the loading panel and the back of the IFMS plate is reasonably assumed as the circumferential line of the cylinder as shown the respective FE analysis (Fig. 2.3b). The displacements are prescribed in the FE model at the "line-shaped" contact area.



(a)                                                                (b)
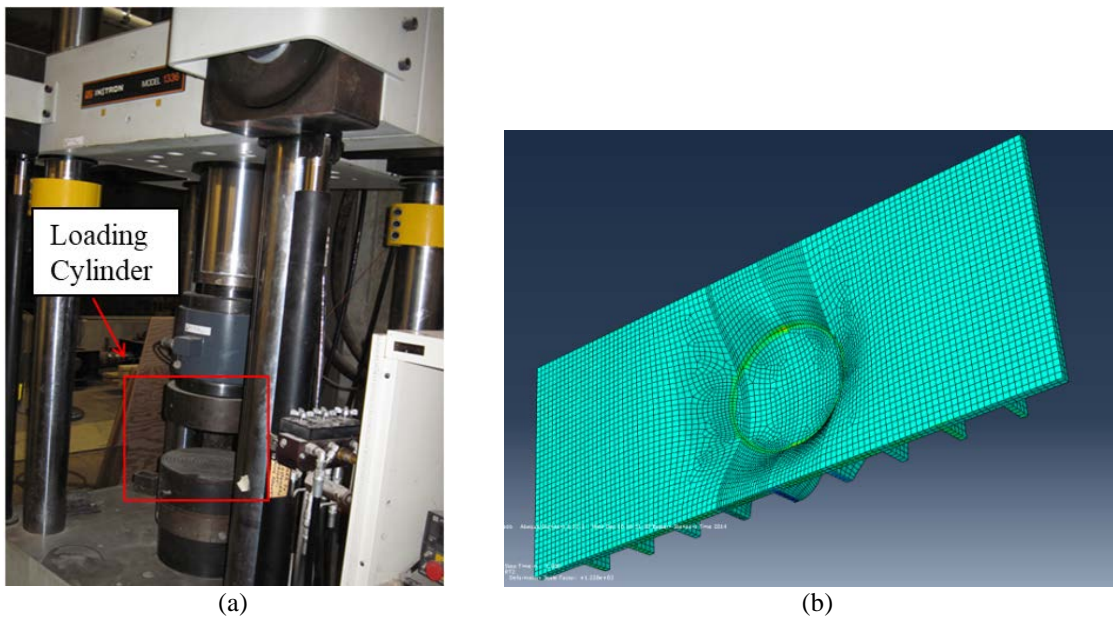
**Figure 2.3: (a)** Test device for laboratory calibration; **(b)** FEA model of the loaded IFMS plate subjected to prescribed ring loading

The resistance variation $\delta R$ measured in the CEE lab tests is converted to linear strain values $\epsilon_{linear} = 0.0014 \delta R$ ohms$^{-1}$. Results from comparisons of two horizontal linear strain values on rib #3 and rib #4 from the FEA model are shown in Fig. 2.4. It is observed the prescribed circular displacement from the finite element analysis gives satisfactory correlation for the total

force. Taking into account that the FEA model calculated strains are very sensitive to the location of the loading area, it can be observed that both the linear horizontal strain gages and the linear vertical strain gages compare reasonably to the strains obtained from the loading tests conducted in the CEE lab. These results provided support for the conclusion that the linear strain gauges were behaving healthily.

The IFMS was then transported to Universal Metals of Calumet, MI, for welding and field installation of the IFMS. Also at Universal Metals, the vertical frame for the IFMS support structure was manufactured and attached to the ice force measuring plate in October, 2013. A second test was performed at Michigan Technological University to check the performance of the system before the installation of the IFMS at the lighthouse.

The deployment was in Lake Superior on an existing lighthouse at the Keweenaw Peninsula. The facilities were in land-fast ice most of the season and substantial quasi-static forces were measured. A data acquisition system included transmission of data from strain gages encased in the IFMS to a data logger and measurements were taken during the 2013-2014 winter season. These data added to our knowledge of (fresh water) ice forces driven primarily by wind and thermal forcing. A more detailed derivation of the inverse ice force prediction algorithm and the in-field ice force estimation will be discussed in the following chapter.
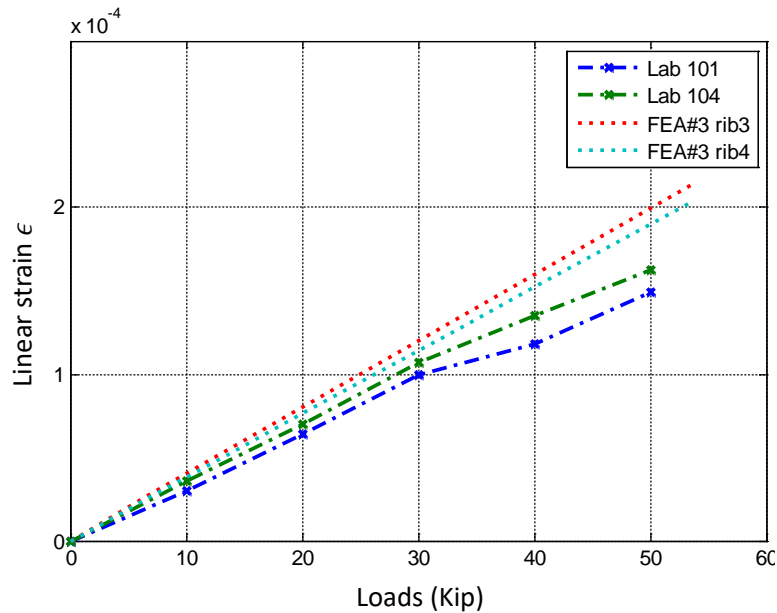
**Figure 2.4:** Linear strain $\epsilon_{linear}$ variation from the lab results compared to the strain on rib 3 and 4 from the FEA model

## 2.3    IFMS Post Calibration at MHL

The IFMS force measuring panel and the other system were uninstalled, and the panel was transported back to Marine Hydrodynamic Lab (MHL) at university of Michigan in May 2015. A post-deployment check was carried out by the IFMS team members (Yuxi Zhang and Dr. Roger D. Roo) to calibrate the sensitivity level for the data acquisition system (DAQ) equipment for strain gage reading with internal and external interruptions.

Detailed tests and the recorded data are attached in Appendix – Post-deployment Calibration Test. It is observed from the post calibration test that the IFMS DAQ system is sound as the whole system is generally robust to small external disturbance of cable flex, noise vibration and small temperature change. The DAQ system is quite sensitive moisture change which is given special attention to. The moisture change was negligible in the field tests as the system is housed

in lighthouse-room and measures are analyzed during small time windows. It is concluded for the

readiness of the equipment for further tests and strain gage allocation improvements.

Chapter 3

**Inverse Ice Force Prediction**

## 3.1    Introduction

Inverse algorithms are presented for calculating the variable pressure acting on a stiffened steel plate. The analytical models are formulated to calculate the quasi-static pressure caused by contact of lake ice driven primarily by thermal expansion and winds. Loading pressures are calculated using strain measurements from a stiffened plate installed on a Keweenaw Peninsula lighthouse in Lake Superior. The ice sheet was essentially stationary through the winter months. The linear relationships between pressure and strain values are obtained by both strip beam theory and orthotropic plate theory. Because the inverse solutions are not necessarily unique, multiple approaches are developed and compared. Fourier pressure terms are calculated from the strain measurements using the inverse orthotropic plate theory algorithms.

In this chapter, two of the approaches are applied using orthotropic plate theory to reflect the variability of the ice: the first sub-model presumes the pressure acts over the entire plate; the second sub-model presumes the pressure acts only within the depth of the measured ice thickness. Favorable comparisons are made of results determined from orthotropic plate theory to results from finite element analyses. A truncated singular value expansion method is applied to retain the robustness of the inverse process for the second sub-model. Both inverse approaches show results

with satisfying accuracy and efficiency compared to the finite element analysis. In addition, laboratory calibration and an examination using the recorded data from field measurements exhibit the effectiveness of the presented approach. Inverse strip beam theory and the inverse orthotropic methods are applied for the evaluations. Through the recorded winter season 2013-2014, the peak ice pressures calculated by the inverse orthotropic plate theories are in the range of 3.5 MPa for the local contact ice pressures, and a maximum of 3.0 MPa for the average ice pressures over the entire plate.

## 3.2    Literature Review for Inverse Load analysis for Stiffened Plate

The plate is composed of evenly distributed stiffeners and readily lends itself to application of orthotropic plate theory (OPT). Boot and Moore (1988) argued that the centroidal neutral axis of the cross section suffices for stress and displacement calculations if the shear deflection is negligible. Moreover, Deb and Booton (1988) recommended using the technical orthotropic plate under uniform load after comparison of two linear finite element models using discrete plate beam formulation.  Here, the IFMS stiffened panel is reasonably idealized as a structurally orthotropic plate given the feature of the uniformly distributed flexural rigidities along plate orthogonal directions (Shimpi and Patel, 2006).

While most analyses are forward calculations for structural response under known pressure, the inverse problem is to extract a physically practical pressure distribution caused by the effect of ice with limited structural measurements. Infinite degrees of loading conditions exist with respect to finite structural response inputs. Due to the lack of uniqueness, the inverse calculation is an optimization procedure for load parameter identifications and load extractions (Engl and Kügler 2005; Chock and Kapania 2003; Li and Kapania 2007). In many cases, small

changes in the input strain readings will possibly result in extreme variations out of the physically feasible range in the forcing predictions (Starkey and Merrill 1989).

Classic methods to overcome these difficulties involve a regularization procedure to convert the ill-posed matrix to neighboring well-posed matrixes (Hansen and O'Leary 1993; Engl and Kügler 2005), thus to eliminate the instability of inverse matrix operation. However, this procedure may introduce extra error caused by a different level of approximation of the reciprocity gap of each simulation (Bonnet and Constantinescu 2005), when usually no a priori knowledge is available. The concept of reciprocity gap is introduced by Andrieux and Abda (1996) to describe the identified difference between the forward input and its inverse calculation of the inputs. Additionally, Ma et al. (2003) argued that a recursive inverse method may be applied to extract the forcing from noisy measurements of a structural response. However, the accuracy of these calculations depends strongly on the initial knowledge of force parameters, information which is unavailable in many cases. Furthermore, the key point towards a well-established inverse problem is the consistency of the description of the class of models to its input data (Snieder 1998). Thus, these iterative computation methods for a recursive process can be expensive and will not be an ideal consideration when limited accuracy is achievable with a few noise-encased inputs.

In the case of limited structural measurements and no a priori knowledge for ice forcing, the inverse problem can be defined as an under-determined problem with ill-posed relationships between the pressure and the structural response. Chock and Kapania (2003) applied a singular-value decomposition (SVD) technique followed by classic least-square methods to identify the pressure parameters for ill-posed inverse systems. Ewing et al. (1999) observed that the presented error percentages by SVD are of the same order to the input noise level from the recorded simulations.

Another widely applicable and similar approach is the truncated singular value expansion (TSVE) method (Engl and Kügler 2005, Semnani and Kamyab, 2008), where the singular values of the matrix are filtered by a "low pass filter" to retain the robustness of the matrix in dominant dimensions. Andrews and Patterson (1976) discussed the application of TSVE in image processing to best restore the original image by retaining the value of the condition number of the matrix. Leone and Soldovieri (2003) argued that the truncated domains of the matrix are observed to affect mainly the dimensions orthogonal to the aimed reconstruction space. More importantly, both SVD and TSVE are considered optimal when the coefficient matrix and its singular value decompositions are available (Engl and Kügler, 2005).

Furthermore, the forms of ice loading may remain in question. Kim et al. (2015) took the form of the ice load as a triangular prism, given that the peak ice pressure occurs at the frame supports. Riska et al. (2002) argued that, for stiffened ship hull plating, the pressure distribution of the ice load is affected by the rigidity ratios of the plate, the stiffeners and the ice during the ice-structure interaction process. Dempsey et al. (2001) discussed the line-like contact forces identified by Riska and high localized pressure zones which may fluctuate rapidly during indentation. In fact, the process of indentation usually involves the development of damaged ice zones adjacent to the indenter or structure due to spalling and macro- or micro-fracturing (Jordaan, 2001). The modes of failure are also velocity dependent (Sodhi, 1991).

In this study however, the ice is considered to be deforming in a ductile manner due to the low drift speed (Bjerkås and Skiple, 2005; Wells et al., 2011). Based on the observations of limited ice motion, this approach studies the quasi-static ice-pressure acting on the plate. Considering the high rigidity of the IFMS plate, the medium-to-high ice thickness measurements, the panel aspect ratio, and the very low ice-contact velocities, the pressure field is initially presumed as uniform

over the width of the panel. This assumption leads to a simple horizontal strip beam formulation as a fast approach to estimate the averaged ice forcing. Furthermore, the vertical strip beam model is formulated to predict the contact ice pressure between two ribs. This second model allows access to estimate the deformation of the plate between stiffeners. These forward strip beam models and their inverse counterparts compare well to the finite element results under the assumed uniform pressures.

Next, the orthotropic plate theory is applied to capture the variability of the pressure over the plate. In the plate analyses, a trigonometric deflection field that satisfies the approximate boundary conditions is assumed. To calculate the Fourier pressure terms from limited strain inputs, two forward orthotropic models are derived with respect to the prescribed area over which the ice pressures are presumed to act: the first model presumes the pressure acts over the entire plate; the second model presumes the pressure acts only within the depth of the measured ice thickness. The convergence of the two approaches is studied through strain evaluations. The inverse counterparts of these models and the applications are discussed in detail. Results by the orthotropic plate theory and the inverse calculations agree well with the finite element model under various loading situations.

## 3.3    Forward Force Prediction Model

### 3.3.1 Strip Beam Theory (SBT)

A horizontal portion of the plate evenly spaced between two stiffeners is considered to form an Euler-Bernoulli strip beam (Fig. 3.1a). The dimensional parameters of a resulting T-

shaped cross section are sketched in Fig. 3.1b. The beam ends are reasonably considered as fixed as a reflection of the constraints from the stiff side bars and back plate. In an effort to obtain a first estimation of the average ice pressure, a uniform ice-pressure $p$ is assumed when the entire plate is fully covered by ice. The uniformly distributed load $q$ on the horizontal beam is calculated by the product of the pressure $p$ and the strip beam cross-section width $t_1 = 0.15$ m. The effective elastic modulus of the upper flange (assumed to be in plane strain) $E_1$ is 220 GPa, and the elastic modulus of the steel of the web $E_2$ is 200 GPa. Thus, the distance $C$ from the effective centroid of the cross-section to the bottom of the fiber is 0.08 m. The effective flexural rigidity $E_e I_y$ of the cross section is $6.49 \times 10^5$ N · m². The relationship for strains located at the bottom of the mid-span of the stiffener under a given distributed load q is as follows:

$$\varepsilon_{yy} = \frac{Cb^2 q}{24 E_e I_y} = 1.85 \times 10^{-9} q \cdot \text{m/N} \tag{3.1}$$

Similarly, a vertical strip beam of width $t_v = 0.03$ m and of length $a_1 = 0.14$ m is analyzed between the span of two neighboring ribs. The dimensions of the vertical strip are sketched in Fig. 3.2. The distributed vertical-beam load is calculated as $q_v = pt_v$. Note that the three vertical linear strain gages are aligned along the middle of the plate at $y_0 = 0.31$ m as denoted by the vertical gray rectangles in previous chapter in Fig. 2.2.

The flexural rigidity is calculated $E_{ev} I_x = t_v h_p^3 E / 12(1 - \mu^2) = 7.71 \times 10^3$ N · m² with the effective elastic modulus $E_{ev}$ as 220 GPa under the plain stress assumption for strip beam theory. In this expression, $t_v$ and $h_p$ are the width and height for the cross-section respectively, and $I_x$ is the moment of inertia for the vertical strip beam cross-section. Using the Euler-Bernoulli strip beam theory, the strain-loading relationship for a mid-point at the bottom of the ideal beam under the distributed load $q_v$ for fixed ends is:

$$\varepsilon_{xx} = \frac{h_p a_1^2 q_v}{48 E_{ev} I_x} = 1.30 \times 10^{-9} q_v \cdot \text{m/N} \qquad (3.2)$$



(a)

(b)
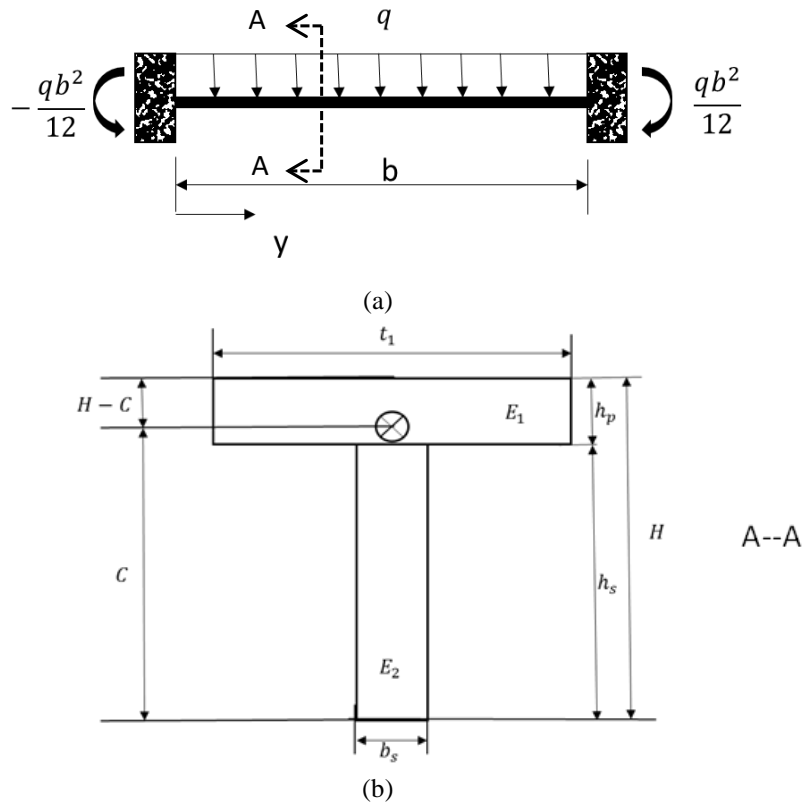
**Figure 3.1: (a)** Euler-Bernoulli beam described for horizontal strip beam; **(b)** T-shaped cross section of the horizontal SBT
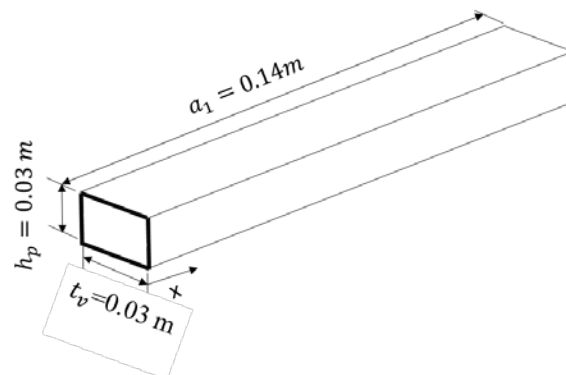


**Figure 3.2:** Dimensions of the vertical strip beam between two ribs

### 3.3.2 Structural Orthotropic Plate Theory (OPT)

To evaluate the ice loading over the plate, the panel with closely distributed stiffeners is formulated as a structurally equivalent orthotropic plate. This idealization models the stiffened plate by an orthotropic homogeneous plate with rigidities averaged in orthogonal directions over the plate with respect to the form of orthotropy (Ventsel and Krauthammer 2001). Ice thickness is found to mainly affect the variability of ice forcing in the vertical direction for narrow structures (Frederking and Schuwarz, 1982; Leira et al., 2009). Thus, a uniform loading is assumed along the horizontal direction in the current analysis for the narrow IFMS plate.

Note the net deflection of the stiffeners does have some component due to shear deformation in addition to bending deflections. However, considering the geometric symmetry of the location of the horizontal linear strain gages, the contribution due to shear deformation is negligible in the calculation of the strain. The current analysis thus uses the small-deflection theory of thin-plate bending in the orthotropic plate theory (OPT) formulation to calculate the response of the plate. Two forward structural calculation models are set up via OPT analyses; both models apply the Navier's equations to simulate the deflection surface and to express the distributed load through the terms of Fourier coefficients. The first OPT model (OPT I) assumes the Fourier coefficients of the pressure to be expanded over the entire plate; the second OPT model (OPT II) constrains the pressure coefficients to be expressed within the area covered by the ice thickness. Moreover, the OPT II model focuses on extracting the maximum peak ice pressure, and thus it is presumed that no pressure from current or wave acts on the plate beneath the ice. The ice thickness is measured from a deployed radiometer included in the IFMS instrumentation. Both forward

calculations give accurate strain evaluations with great efficiency for the quasi-static stress analysis.

Based on the IFMS geometry, clamped boundary conditions are applied along the vertical edges of the plate (i.e. $x$-direction), and pinned boundaries are applied along the top and bottom edges of the plate (i.e. $y$-direction). The stiffened panel is first modeled with two stiff side bars and with the back plate on as a reflection of the actual construction of the IFMS plate. The second model consisting of only the stiffened face plate is fixed along the vertical edge and pinned along the horizontal edge. The designated strains calculated by these two FE models are observed to differ by less than 1%, thus justifying the boundary conditions of the second model as reasonable constraints in the OPT analysis.

To satisfy the boundary conditions, a double Fourier series function is composed for the displacement field $w(x, y)$. Let $m = 1..M$, $n = 1..N$, where $M$ is the order of coefficient terms to be retained along the $x$ direction, and $N$ is the order of terms along the $y$ direction:

$$w(x, y) = \sum_{m=1}^{M}\sum_{n=1}^{N} W_{mn} \sin(\frac{m\pi x}{a})[1 - \cos(\frac{2n\pi y}{b})] \tag{3.3}$$

### 3.3.2.1 OPT I—Pressure Acting Over the Entire Plate

For OPT I, the coefficients $P_{I_{mn}}$ are used to express the pressure coefficients over the entire plate for the double series pressure solution $p_I(x, y)$:

$$p_I(x, y) = \sum_{m=1}^{M}\sum_{n=1}^{N} P_{I_{mn}} \sin(\frac{m\pi x}{a}) \sin(\frac{n\pi y}{b}) \tag{3.4}$$
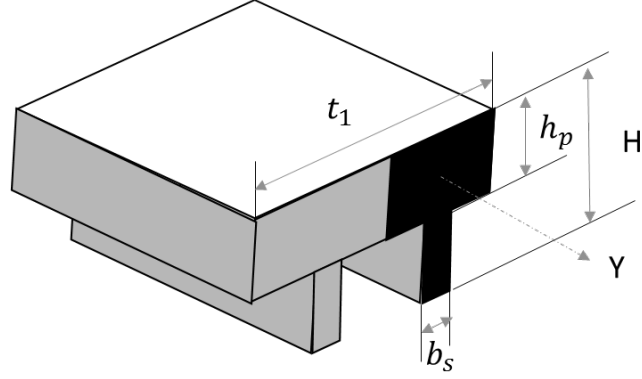
**Figure 3.3:** T-shaped cross sections of the representative OPT I model

Using the assumption of uniform pressure along the y direction, the Fourier series of the pressure field $p_I$ is expressed by retaining the coefficient terms over the x direction as denoted by $P_{I_m}$:

$$p_I(x, y) = \sum_{m=1}^{M} \sum_{n=1,3..}^{N} P_{I_m} \frac{4}{n\pi} \sin(\frac{m\pi x}{a}) \sin(\frac{n\pi y}{b}) \tag{3.5}$$

Based on the Kirchhoff's small-deflection plate bending theory and orthotropic plate theory, the strain energy $U$ of bending for orthotropic plate is expressed in integral form over the entire plate surface area $A$:

$$U = \frac{1}{2} \iint_A [D_x(\frac{\partial^2 \omega}{\partial x^2})^2 + D_y(\frac{\partial^2 \omega}{\partial y^2})^2 + 2D_{xy}\frac{\partial^2 \omega}{\partial x^2}\frac{\partial^2 \omega}{\partial y^2} + 4D_s(\frac{\partial^2 \omega}{\partial y \partial x})^2] dA \tag{3.6}$$

Substituting (3) into (6) and integrating, the strain energy of bending for the plate is expressed by Fourier displacement terms:

$$U = \frac{1}{2} \sum_{m=1}^{M} \sum_{n=1}^{N} (\frac{3bm^4\pi^4}{4a^3} D_x W_{mn}^2 - \frac{2m^2n^2\pi^4}{ab} D_{xy} W_{mn}^2 + \frac{4an^4\pi^4}{b^3} D_y W_{mn}^2 + \frac{4m^2n^2\pi^4}{ab} D_s W_{mn}^2) \tag{3.7}$$

To calculate the flexural rigidities, the representative T-shaped cross section for the OPT model is of the same dimensions as described for the horizontal strip beam (Fig.3.3). The flexural and torsional rigidity formulas of the equivalent orthotropic plate are given by Ventsel and

Krauthammer (2001) for several commonly encountered stiffener formations. The rigidities of the IFMS plate in Eq. (3.6) and Eq. (3.7) are calculated as:

$$D_y = \frac{EI_y}{t_1}, D_x = \frac{Eh_p^3}{12(1-\frac{b_s}{t_1}+\frac{h_p b_s^3}{H^3})}, D_{xy} = 0, D_s \approx \frac{Gh^3}{12} + \frac{C_t}{2t_1} \tag{3.8}$$

where $G$ is the torsional rigidity of the rib about its centroidal axis. Also, the external potential energy $V$ is written as a function of the displacement and pressure terms integrated over the plate volume $v$:

$$V = \iiint_v w(x,y)p_I(x,y)dv = \sum_{m=1}^{M}\sum_{n=1}^{N}\sum_{j=1,3..}^{N} P_{I_m} \frac{4abW_{mn}}{\pi^2 j}[\frac{1}{j}-\frac{1}{2(j+2n)}-\frac{1}{2(j-2n)}] \tag{3.9}$$

Note that the same number of deformation coefficients are retained as that of the pressure coefficients, in which case $m = 1..M$, $n = 1..N$. Applying the principle of stationary total potential energy $\partial U/\partial W_{mn} - \partial V/\partial W_{mn} = 0$, the deformation coefficients are obtained in relation to the Fourier pressure terms:

$$W_{mn} = \sum_{j=1,3..}^{N} P_{I_m} \frac{\frac{4ab}{\pi^2 j}[\frac{1}{j}-\frac{1}{2(j+2n)}-\frac{1}{2(j-2n)}]}{(\frac{3bm^4\pi^4}{4a^3}D_x - \frac{2m^2n^2\pi^4}{ab}D_{xy} + \frac{4an^4\pi^4}{b^3}D_y + \frac{4m^2n^2\pi^4}{ab}D_s)} \tag{3.10}$$

The horizontal strains are found from the displacement Fourier series and the strain-displacement relations:

$$\varepsilon_{yy} = -z_0 \sum_{m=1}^{M}\sum_{n=1}^{N} W_{mn}(\frac{2n\pi}{b})^2 \sin(\frac{m\pi x}{a})\cos(\frac{2n\pi y}{b}) \tag{3.11}$$

where $z_0$ is the distance of the point to the centroidal plane. The linear relationship of the strain value to the pressure Fourier coefficient term $P_{I_m}$ is:

$$\varepsilon_{yy} = -z_0 \sum_{m=1}^{M}\sum_{n=1}^{N} P_{I_m}(\frac{2n\pi}{b})^2 \sin(\frac{m\pi x}{a})\cos(\frac{2n\pi y}{b}) \frac{\sum_{j=1,3..}^{N}\frac{4ab}{\pi^2 j}[\frac{1}{j}-\frac{1}{2(j+2n)}-\frac{1}{2(j-2n)}]}{\frac{3bm^4\pi^4}{4a^3}D_x - \frac{3m^2n^2\pi^4}{ab}D_{xy} + \frac{4an^4\pi^4}{b^3}D_y + \frac{4m^2n^2\pi^4}{ab}D_s} \tag{3.12}$$

### 3.3.2.2 OPT II— Pressure Acting Over the Ice-covered Area

To capture more accurately the peak pressure over the ice covered area, the pressure coefficients of the Fourier series are constrained to act within a specific area defined by the measured ice thickness $t_{ice}$. Satisfying the same displacement boundary conditions stated in the previous model, the same displacement expression Eq. (3.3) is used, and the ice-covered area is assumed to be $t_{ice}b$. The pressure field $p_{II}(x, y)$ on the constrained area is then expanded by the coefficients $P_{II_i}$, where $i$ is the order of the pressure coefficient along the $x$-direction. Similar to the OPT I summation, $M$ and $N$ are the total coefficient terms along $x$ or $y$ coordinate respectively:

$$p_{II}(x, y) = \sum_{i=1}^{M} \sum_{j=1,3..}^{N} \frac{4}{\pi j} \sin(\frac{i \pi \tilde{x}}{t_{ice}}) \sin(\frac{j \pi y}{b}) \cdot P_{II_i} \tag{3.13}$$

Here $\tilde{x} = x - x_1$, $\tilde{x} \subseteq [0, t_{ice}]$, $x_1$ is the starting coordinate along x for the ice contact area.

Substituting (3.13) into Eq. (3.6), considering the external energy integral Eq. in (3.9), and applying stationary total potential energy, the relationship of Fourier coefficients for $W_{mn}$ as a function of pressure coefficients $P_{II_i}$ over the confined ice-covered area is obtained. Let $k = m/a$, where $a$ is the depth of the plate vertically, $W_{mn}$ is then expressed as follows:

if $ai \neq mt_{ice}$:

$$W_{mn} = \sum_i \sum_j \frac{4b}{k\pi^3 j}[\frac{1}{j} - \frac{1}{2(j+2n)} - \frac{1}{2(j-2n)}] \cdot \frac{a^2 it_{ice}[(-1)^{i+1} \sin(\frac{m\pi(x_1+t_{ice})}{a}) + \sin(\frac{m\pi x_1}{a})]}{\pi(a^2 i^2 - m^2 t_{ice}^2)(\frac{3bm^4\pi^4}{4a^3}D_x - \frac{2m^2n^2\pi^4}{ab}D_{xy} + \frac{4an^4\pi^4}{b^3}D_y + \frac{4m^2n^2\pi^4}{ab}D_s)} P_{II_i}$$

if $ai = mt_{ice}$:

$$W_{mn} = \sum_i \sum_j \frac{4b}{k\pi^3 j}\left[\frac{1}{j}-\frac{1}{2(j+2n)}-\frac{1}{2(j-2n)}\right]\frac{[\cos(k\pi x_1)k\pi t_{ice}-\frac{1}{2}\cos(k\pi x_1)\sin(2k\pi t_{ice})+\sin(k\pi x_1)\sin^2(k\pi t_{ice})]}{\frac{3bm^4\pi^4}{4a^3}D_x-\frac{2m^2n^2\pi^4}{ab}D_{xy}+\frac{4an^4\pi^4}{b^3}D_y+\frac{4m^2n^2\pi^4}{ab}D_s}P_{II_i}$$

(3.14)

where $i = 1,2,\ldots M$, $j = 1,3,\ldots,N$, $m = 1,2,\ldots M$, and $n = 1,2,\ldots N$.

The linear relationship of the strain value $\varepsilon_{yy}$ at (x, y) to the pressure Fourier coefficient terms for OPT II is calculated by substituting Eq. (3.14) into Eq. (3.11):

if $ai \neq mt_{ice}$:

$$\varepsilon_{yy}(x,y) = -z_0\sum_{m=1}^{M}\sum_{n=1}^{N}(\frac{2n\pi}{b})^2 \sin(\frac{m\pi x}{a})\cos(\frac{2n\pi y}{b})\cdot$$

$$\sum_{j=1,3..}^{N}\sum_{i=1}^{M}\frac{4b}{k\pi^3 j}\left[\frac{1}{j}-\frac{1}{2(j+2n)}-\frac{1}{2(j-2n)}\right]\cdot\frac{a^2 it_{ice}[(-1)^{i+1}\sin(\frac{m\pi(x_1+t_{ice})}{a})+\sin(\frac{m\pi x_1}{a})]}{\pi(a^2 i^2-m^2 t_{ice}^2)(\frac{3bm^4\pi^4}{4a^3}D_x-\frac{2m^2n^2\pi^4}{ab}D_{xy}+\frac{4an^4\pi^4}{b^3}D_y+\frac{4m^2n^2\pi^4}{ab}D_s)}P_{IIi}$$

if $ai = mt_{ice}$:

$$\varepsilon_{yy}(x,y) = -z_0\sum_{m=1}^{M}\sum_{n=1}^{N}(\frac{2n\pi}{b})^2 \sin(\frac{m\pi x}{a})\cos(\frac{2n\pi y}{b})\cdot$$

$$\sum_{j=1,3..}^{N}\sum_{i=1}^{M}\frac{4b}{k\pi^3 j}\left[\frac{1}{j}-\frac{1}{2(j+2n)}-\frac{1}{2(j-2n)}\right]\cdot\frac{[\cos(k\pi x_1)k\pi t_{ice}-\frac{1}{2}\cos(k\pi x_1)\sin(2k\pi t_{ice})+\sin(k\pi x_1)\sin^2(k\pi t_{ice})]}{(\frac{3bm^4\pi^4}{4a^3}D_x-\frac{2m^2n^2\pi^4}{ab}D_{xy}+\frac{4an^4\pi^4}{b^3}D_y+\frac{4m^2n^2\pi^4}{ab}D_s)}P_{II_i}$$

(3.15)

## 3.4    Evaluation of Forward Formulation

To compare the analytical solutions with the finite element verification results, three loading cases are considered: Loading Case # 1 (LC#1) is a uniform pressure of 0.69 MPa over the entire plate; Loading Case # 2 (LC#2) is a single half-sinusoidal pressure between two neighboring ribs with amplitude of 1.08 MPa; Loading Case # 3 (LC#3) is a constant patched pressure of 0.69 MPa distributed over the first four ribs from the top of the plate. LC#1 and LC#3

31

are applied to extract the average global ice pressure over the entire plate or the designated ice-covered area; the loading area of LC#3 approximates the measured ice-structure contact area with an example of the ice thickness of $0.6\ m$. Additionally, LC#2 is used to simulate a local peak ice pressure between ribs. The Finite Element (FE) model is set up for the verification effort using the 3D solid element analysis, where shear effect is included.

Both the horizontal and vertical strains calculated by the SBT and OPT I are compared to the FE model results under LC#1, and the results are given in Table 1. It is observed that the horizontal linear strains $\epsilon_{yy}$ calculated by the SBT and by OPT I at the order of 6 satisfyingly agree with the values predicted from the FE model. In a closer evaluation, the absolute error ratio by SBT is to the mean value obtained by FEA calculated to be within 3.4%.

The error percentage presented by OPT I at the order of 6 to the mean value obtained by FEA is also approximately 3.4%. The close approximation achieved by both SBT and OPT I for uniform loading LC#1 for the horizontal linear strain evaluations validates the accuracy of neglecting the shear effect in the specific strain evaluations. It is noted that using Timoshenko beam theory including the shear deformation approximates better the displacements; however the strains at the HLSG remain unaffected by the shear deflection effect.

The vertical SBT agrees well with the FE analyzed in the vertical strain evaluations $\varepsilon_{xx}$ at the VLSG locations. The calculated vertical strains by OPT I along the plate mid-line are compared with those obtained from the FE analysis, as is shown in Fig. 3.4. It is found that the vertical SBT model with fixed ends is 2% more rigid than the finite element model based on the calculated bending strains (Table 3.1). Thus the vertical SBT can be applied inversely to extract the contact ice-pressure between the ribs using the fixed end conditions for the IFMS plate analysis. The vertical linear strains $\epsilon_{xx}$ calculated by the OPT I are not comparable to the FE model at the

designated vertical linear strain gages (VLSG) due to the smearing effect of the structural orthotropic plate assumption.

In further efforts to evaluate the OPT formulation, the horizontal strain solutions $\varepsilon_{yy}$ are calculated by OPT I through Eq. (3.12) at the designated locations of the horizontal linear strain gages (HLSG). The strains are calculated at different orders as is shown in Fig 3.5. It is found that the OPT I converges very accurately at the order M=9 by the observation of an overlapping of its results to those at the order M=11 under all three loading conditions. In Fig. 3.5, The FEA results are represented by crosses, and the strain solutions obtained by OPT I at the order of 6 are depicted by solid lines. The calculated strain lines at the order of 6 suffice for reasonable accuracy. The error percentage defined by the difference ratio between the forward calculated analytical strains to those from the FE analysis is approximated to be within the range of 1.0% to 13.5% at the order of 6 or above.

The forward pressure simulation and strain solution under LC#1 by OPT II is the same as by OPT I. The exact pressure formulation is achieved at the order M=1 for LC #2, and the pressure field is then considered convergent at the order M=3 for LC #3, by OPT II (Fig.3.6). Compared to OPT I, OPT II converges faster in the forward pressure and strain evaluations; this faster convergence is more obvious when the ice-covered area is thinner. The strains calculated by OPT I are converging to the FE results more accurately with increased coefficient terms. However, this is not necessarily true for the strains calculated by OPT II to converge to the FE solution. Thus, in a forward simulation, OPT I is recommended for its accuracy and is applicable without the necessary input of ice thickness; while OPT II is considered more efficient in describing the pressure distribution over a thinner ice-covered area, where the knowledge of ice thickness is necessary. The strain to pressure relationships expressed through Eq. (3.15) are observed to be

coupled and thus may yield ill-posed coefficient matrixes for a direct inverse of the OPT II algorithm. However the inverse of OPT II will be optimized through a process of system parameter identification to retain the stability of the inverse calculation, which is discussed later.
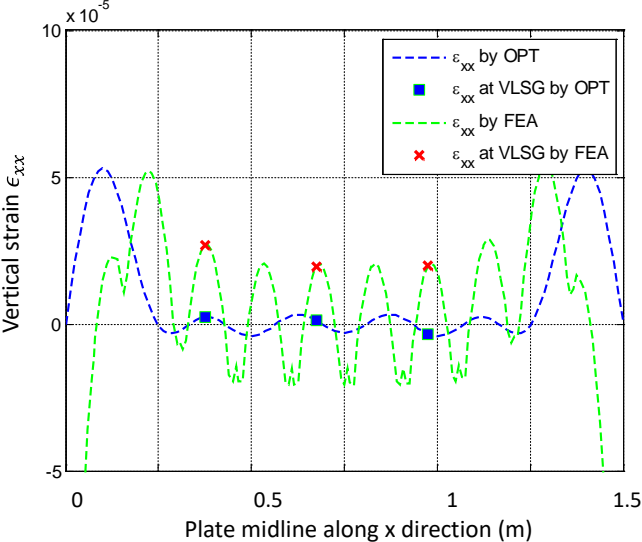


**Figure 3.4:** Vertical linear strains ε_xx calculated by OPT I compared to FEA results, under LC#1
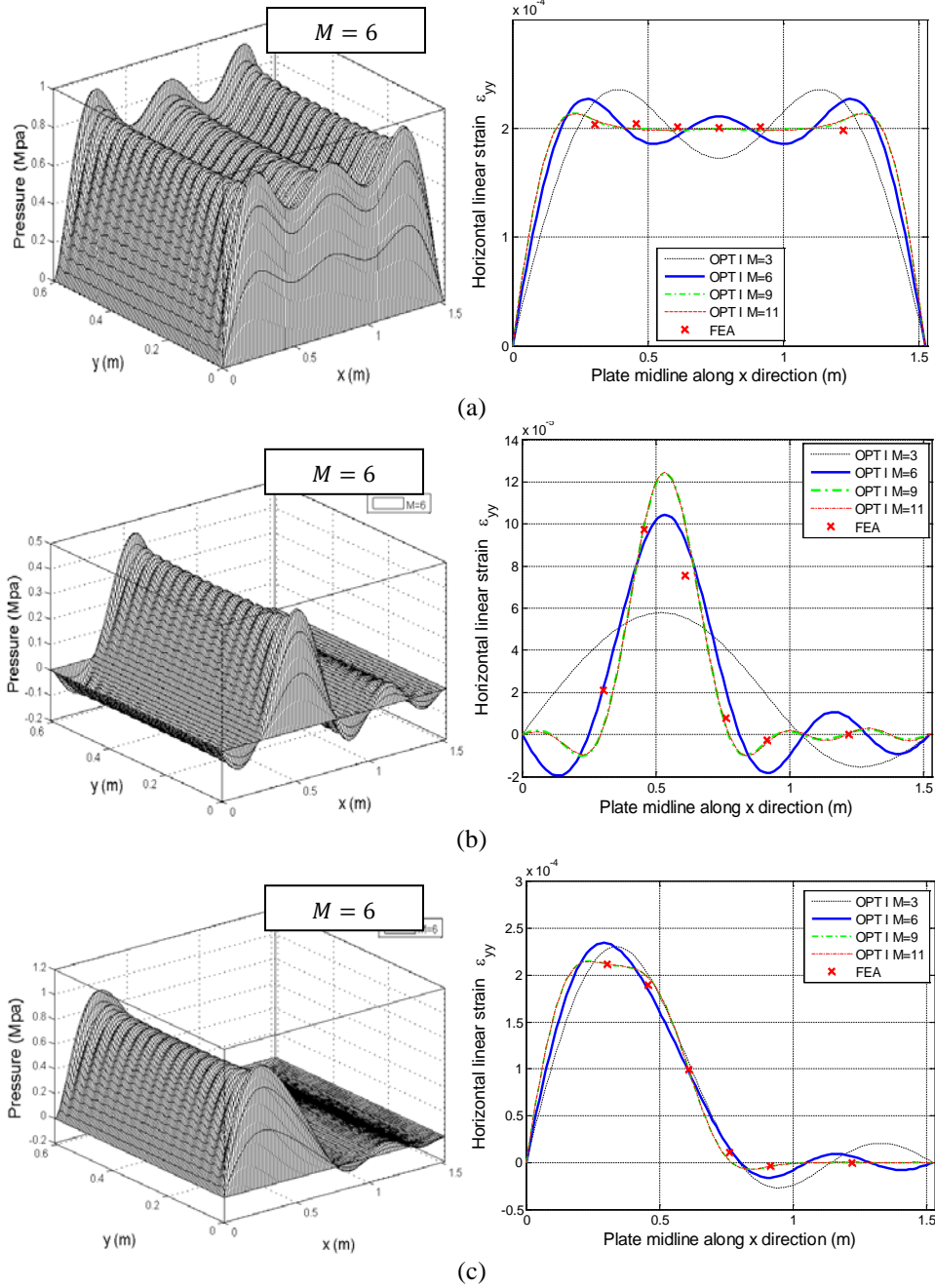
**Figure 3.5:** Pressure predicted by OPT I and the Convergence of $\epsilon_{yy}$ by OPT I at different orders of M for: **(a)** LC#1; **(b)** LC#2; **(c)** LC#3
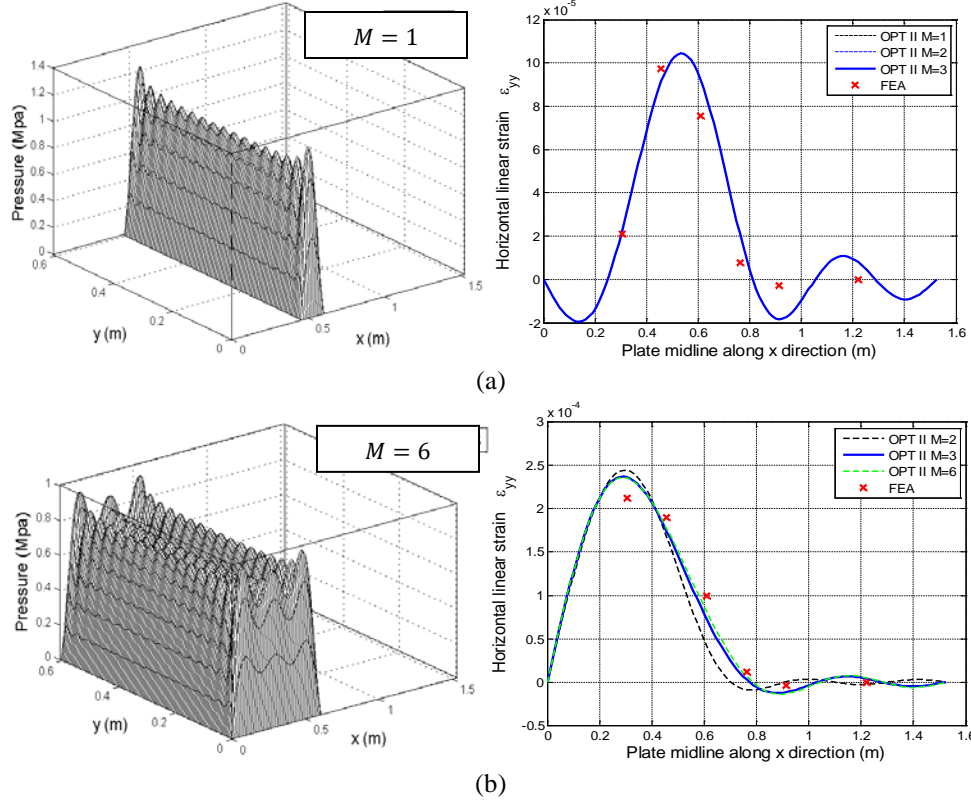
**Figure 3.6:** Pressure predicted by OPT II and the calculated strains for: **(a)** LC# 2 M=1; **(b)** LC#3 M=3

## 3.5 Orthotropic Plate Inverse Theory (OPIT)

The orthotropic plate inverse theory (OPIT) is derived from the forward OPT formulations to obtain the pressure coefficient terms $\mathbf{P_I}$ or $\mathbf{P_{II}}$ through the established relationships from the strain measurements $\boldsymbol{\varepsilon_{yy}}$. Using the Fourier displacement coefficients $W_{mn}$ in Eq. (3.10) and Eq. (3.14), the deformation terms can be expressed in linear matrix form:

$$\mathbf{W_{l_n}} = \mathbf{A_{l_n}}\mathbf{P_l} \qquad\qquad l = I, II \qquad\qquad (3.16)$$

The column matrix $\mathbf{W_{l_n}}$ represents the $n^{th}$ column of the $\mathbf{W_l}$ matrix, where $l = I$ indicates the OPT I algorithm and the $\mathbf{W_l}$ is then expressed though Eq. (3.10); $l = II$ indicates the OPT II algorithm and the $\mathbf{W_{II}}$ is thus expressed through Eq. (3.14). $\mathbf{A_{l_n}}$ is the displacement-pressure coefficient matrix; $\mathbf{P_l}$ represents the vector of Fourier coefficients for the pressure field with M

elements; $n$ ranges from 1 to $N$, and $N$ is the total order satisfying the convergence of uniform pressure along the y-direction.

Similarly, the strain-displacement relationship in Eq. (3.11) is configured using the matrix $\mathbf{S_n}$ with the subscript $n$ representing the order along y-direction; the strain vector is expressed for the $l_{th}$ OPT algorithm as follows:

$$\boldsymbol{\varepsilon_{yy}} = \sum_{n=1}^{n=N} \mathbf{S_n} \, \mathbf{W_{l_n}} \tag{3.17}$$

Here the $I_{inp}$ input strains compose the strain vector $\boldsymbol{\varepsilon_{yy}}$. For example, $I_{inp} = 6$ may be used based on the number of linear strains gages allocated on the IFMS. Substituting Eq. (3.16) into Eq. (3.17), the strain vector is expressed by the pressure terms as:

$$\boldsymbol{\varepsilon_{yy}} = \sum_{n=1}^{n=N} \mathbf{S_n} \, \mathbf{A_{l_n}} \mathbf{P_l} \tag{3.18}$$

Assuming the coefficient matrix to order of $N$, the general orthotropic inverse coefficient matrix operation is obtained in the following form:

$$\mathbf{P_l} = \sum_{n=1}^{n=N} \mathbf{A_{l_n}}^{-1} \mathbf{S_n^{-1}} \cdot \boldsymbol{\varepsilon_{yy}} \tag{3.19}$$

### 3.5.1 OPIT I-Inverse Model I

The maximum number of coefficients is $M_1$ to be retrieved through the linear matrix operation described in (3.19); in OPIT I, $M_1 = I_{inp}$. For example, $I_{inp} = 6$, the coefficient vector is thus described as:

$$\mathbf{P_I} = [P_{I_1} \, P_{I_2} P_{I_3} \, P_{I_4} \, P_{I_5} \, P_{I_6}]' \tag{3.20}$$

The total HLSG measurements are taken from ribs #1 to rib #5 plus rib #7; the six linear strain input elements are defined in the strain vector:

$$\boldsymbol{\varepsilon_{yy}} = [\varepsilon_{yy_1}\varepsilon_{yy_2}\varepsilon_{yy_3}\varepsilon_{yy_4}\varepsilon_{yy_5}\varepsilon_{yy_6}]' \tag{3.21}$$

The strain values can be calculated from Eq. (3.11) via both OPT methods. In the case of the horizontal linear strain gages: $y_0 = b/2$; $x_g$ are the coordinates of the horizontal linear strain gages, here $g = 1..I_{inp}$. It is found:

$$\varepsilon_{yy}(x_g, y_0) = \varepsilon_{yy_g} = z_0(\frac{2\pi}{b})^2 \sum_{m=1}^{6}\sum_{n=1}^{N} \sin(\frac{m\pi x_g}{a})\cos(\frac{2n\pi y_0}{b})W_{mn} \tag{3.22}$$

The elements for the $n^{th}$ strain-displacement matrix $\mathbf{S_n}$ are:

$$S(g,m)_n = z_0(\frac{2\pi}{b})^2 \sin(\frac{m\pi x_g}{a})\cos(\frac{2n\pi y_0}{b}) \tag{3.23}$$

It is observed that $N = 33$ will sufficiently allow for the convergence of uniform pressure along the y direction, thus, $N = 33$ is used in the following derivations and sample calculations. The elements in the diagonal displacement-pressure coefficient matrix $\mathbf{A_{I_n}}$ can be derived from Eq. (3.10) as follows:

$$A_I(m,m)_n = \sum_{j=1,3..}^{N} \frac{4ab[\dfrac{1}{j} - \dfrac{1}{2(j+2n)} - \dfrac{1}{2(j-2n)}]}{j\pi^2[\dfrac{3bm^4\pi^4}{4a^3}D_x - \dfrac{2m^2n^2\pi^4}{ab}D_{xy} + \dfrac{4an^4\pi^4}{b^3}D_y + \dfrac{4m^2n^2\pi^4}{ab}D_s]}$$

$$\tag{3.24}$$

where, $j = 1,3,..,33$. Let the strain-pressure coefficients relation matrix $\mathbf{C_I}$ for OPIT I be defined by,

$$\mathbf{C_I} = \sum_{n=1}^{n=N} \mathbf{S_n A_{I_n}} \tag{3.25}$$

The strain-pressure relationship is then established as,

$$\boldsymbol{\varepsilon_{yy}} = \mathbf{C_I P_I} \tag{3.26}$$

Inversely,

$$\mathbf{P_I} = \mathbf{C_I}^{-1}\boldsymbol{\varepsilon_{yy}} \tag{3.27}$$

The matrix $\mathbf{C_I^{-1}}$ is a well-posed full-matrix with the condition number roughly equals 8.0 to calculate the pressure coefficient terms over the whole plate.

## 3.5.2 OPIT II-Inverse Model II

Still using $I_{inp}$ strain inputs from the HLSG locations, the pressure Fourier coefficients are extracted over the constrained ice covered area. Similarly, $M_2$ is the maximum number of the pressure coefficient terms that can be calculated through the linear matrix operation by OPIT II, and $M_2 = I_{inp}$ in this initial evaluation of OPIT II. The pressure-displacement matrix $\mathbf{A_{II_n}}$ for OPIT II will be expressed in linear matrix form from the Eq. (14). Firstly, let:

$$e_{II}(m,i)_n = \frac{a^2 it_{ice}}{\pi(a^2i^2 - m^2t_{ice}^2)}[(-1)^{i+1}\sin(\frac{m\pi(x_1+t_{ice})}{a}) + \sin(\frac{m\pi x_1}{a})], \text{ if } ai \neq mt_{ice}$$

$$e_{II}(m,i)_n = \frac{1}{2k\pi}[\cos(k\pi x_1)k\pi t - \frac{1}{2}\cos(k\pi x_1)\sin(2k\pi t_{ice}) + \sin(k\pi x_1)\sin^2(k\pi t_{ice})], \text{ if } ai =$$

$$mt_{ice} \qquad (3.28)$$

where $i = 1 \ldots M_2$. Then using Eq. (3.16), the $(m,i)$ element in matrix $\mathbf{A_{II_n}}$ is:

$$A_{II}(m,i)_n = \sum_{j=1,3..}^{33} \frac{b}{2j}[\frac{1}{j} - \frac{1}{2(j+2n)} - \frac{1}{2(j-2n)}]\frac{e_{II}(m,i)_n}{(\frac{3bm^4\pi^4}{4a^3}D_x - \frac{2m^2n^2\pi^4}{ab}D_{xy} + \frac{4an^4\pi^4}{b^3}D_y + \frac{4m^2n^2\pi^4}{ab}D_s)} \qquad (3.29)$$

where $m = 1, .., M_2$.

The strain-displacement coefficient matrix $\mathbf{S_n}$ is independent of the form of pressure applied, and it is the same as in Eq. (3.23) for OPIT I. The inverse of the coefficient matrix $\mathbf{C_{II}}$ relating the strain vector to the pressure terms is calculated as the summation of the products of $\mathbf{S_n}$ and $\mathbf{A_{II_n}}$

$$\mathbf{C_{II}} = \sum_{n=1}^{n=N} \mathbf{S_n A_{II_n}} \qquad (3.30)$$

Similarly the strain-pressure relationship is then established as,

$$\varepsilon_{yy} = \mathbf{C}_{II}\mathbf{P}_{II} \tag{3.31}$$

Inversely,

$$\mathbf{P}_{II} = \mathbf{C}_{II}^{-1}\varepsilon_{yy} \tag{3.32}$$

### 3.5.3 TSVE Optimization –for OPIT II

The coefficient matrix $\mathbf{C}_{II}$ may be ill-posed when the order of the coefficient matrix $M_2$ increases to a certain degree, depending on the confinement of the ice-covered area for the pressure terms. The condition number of the forward coefficient matrix $C_{II}$ is found to be over $10^3$ for both LC#2 and for LC#3, when $M_2 = I_{inp} = 6$. A direct inverse of the OPT II model for LC#2 and LC#3 leads to variations in pressures which are out of the feasible range (Fig. 3.7a and 3.7b).



(a)                                 (b)
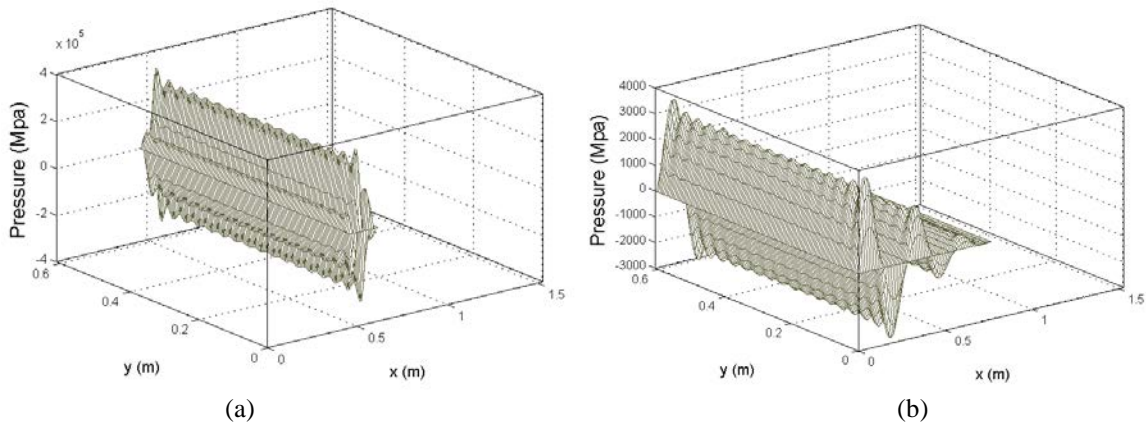
**Figure 3.7:** Infeasible pressure solution by a direct inverse of OPT II without truncation for: **(a)** LC#2; **(b)** LC#3

The reason is that the non-orthogonal Fourier coefficient matrix for OPT II is coupled and ill-posed, and this near singularity will intensify with the increment of the orders of the coefficients. The truncated singular value expansion method (TSVE) is first applied as an

optimization procedure to truncate the order of the coefficient matrix to $M_{trun}$, and re-expand the truncated matrix through the pseudo inverse matrix operation (Hansen and O'Leary 1993; Chock and Kapania 2003). The philosophy of the optimization procedure is to truncate the terms of zero or near-zero singular values to control the condition number of the coefficient matrix (Hansen 1987; Semnani 2008; Semnani 2010). The optimal number of the pressure terms $M_{trun}$ is determined through the TSVE procedure by applying a "low-pass" filter to filter out the values of the singular values $s_i (i = 1,2..M_2)$ that are smaller than $e$, where $e$ is a prescribed lower limit subject to optimization according to different loading case. The TSVE optimization scheme is sketched in Fig. 3.8.
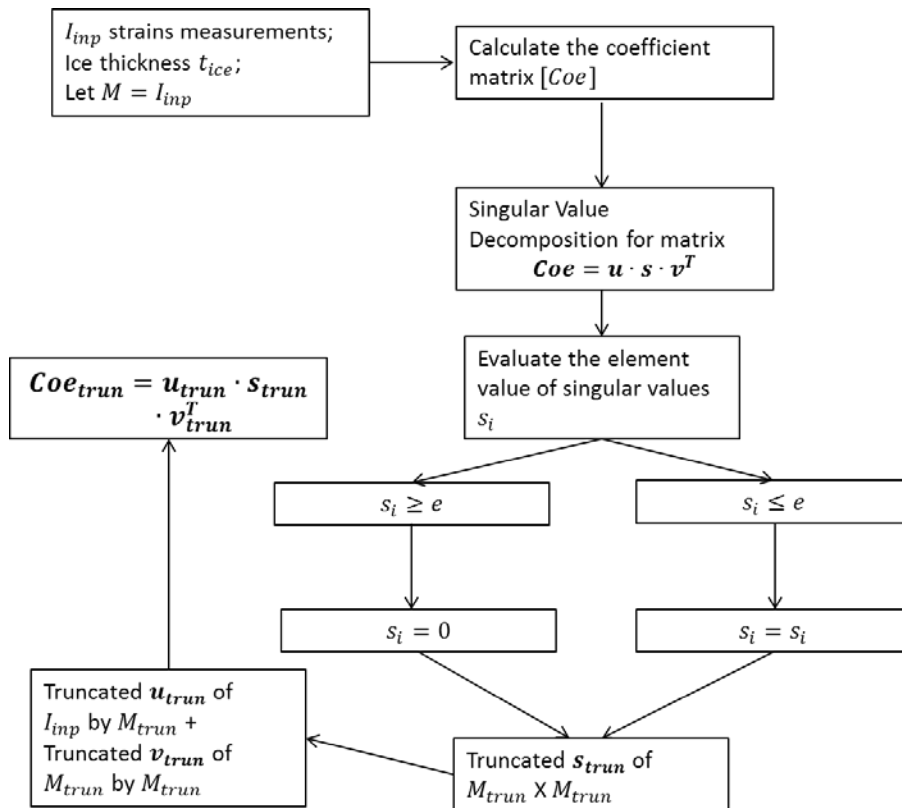


**Figure 3.8:** Schematic diagram of the TSVE procedure for calculating of $M_{trun}$ and $Coe_{trun}$

41

As a rule of thumb, the order $k_c$ of the condition number indicates the level of accuracy caused by a loss of precision from the arithmetic method (Kaiman 1996). The minimum filtering value $e$ for the "low-pass" filter is defined as $1/10^{\kappa_c}$. Chock and Kapania (2003) reported that the error by using only the singular value decomposition methods (SVD) in the steepest descents is however of similar order as that from the input noise level. A difference of 5% to 15% to those exact strains obtained from the FE model is found in the OPT II forward strain prediction at convergence. Thus by constraining $e$ within the range of $10^{-6}$ to$10^{-7}$, the optimization process suffices to retain the robustness of the inversion of the matrix calculation to an error range of less than 15%. Finally, by re-expanding the coefficient matrix at the truncated order $M_{trun}$, the coefficient matrix is of dimension of $M_{trun}$ by $I_{inp}$, as shown in Fig. 3.8. For simplicity, the OPIT II model refers to the inverse calculation of OPT II after the TSVE process in the following discussion.

## 3.6    Sample Inverse Calculations

In an effort to evaluate the pressure solution from strain measurements, six linear strain readings at the HLSG from the FE model serve as inputs to the OPIT I and OPIT II models. Three loading conditions are evaluated, and the results of the calculated pressure by both OPIT methods are compared to the exact pressure prescribed in the FE model, depicted as the plane layers in Fig. 3.9.

As discussed in the forward strain evaluations, the pressure solution by OPIT II under LC #1 is of exactly the same value as obtained by OPIT I (Fig. 3.9a). For LC#2, the peak pressure is calculated as 1.29 MPa with $M_{trun} = 2$ coefficient terms by OPIT II, while the peak value is

evaluated as 0.41 MPa by OPIT I for LC#2. The amplitude is 1.57 MPa for LC#2 in the FE model (Fig. 3.9b).

For all load cases, the peak values and the integrated pressure over the ice-covered area calculated by the OPIT algorithms are compared with the FE model pressure values given in the FE model, and the results are listed in Table 3.2. For LC#3, integrating pressure over the ice thickness, both algorithms achieve 80% of the FE result (Fig. 3.9c). The reduction of the integrated force is due to the Fourier approximation. The OPIT I extracts 6 coefficient terms while the OPIT II is truncated to 3 terms. From the results, it is observed that the OPIT I is stable in estimating ice pressure distribution with great accuracy for most loading cases, especially when the ice-covered area spans over one-half of the plate. The OPIT I is able to achieve an improved accuracy by increasing the coefficient terms with additional strain recordings. On the other hand, the peak value solution found by OPIT II for LC#2 is accurate to within 80%, retaining only two coefficient terms. The capability of capturing peak pressure by OPIT II is notably efficient and accurate when the ice-covered area is reduced.

(a)



(b)



(c)
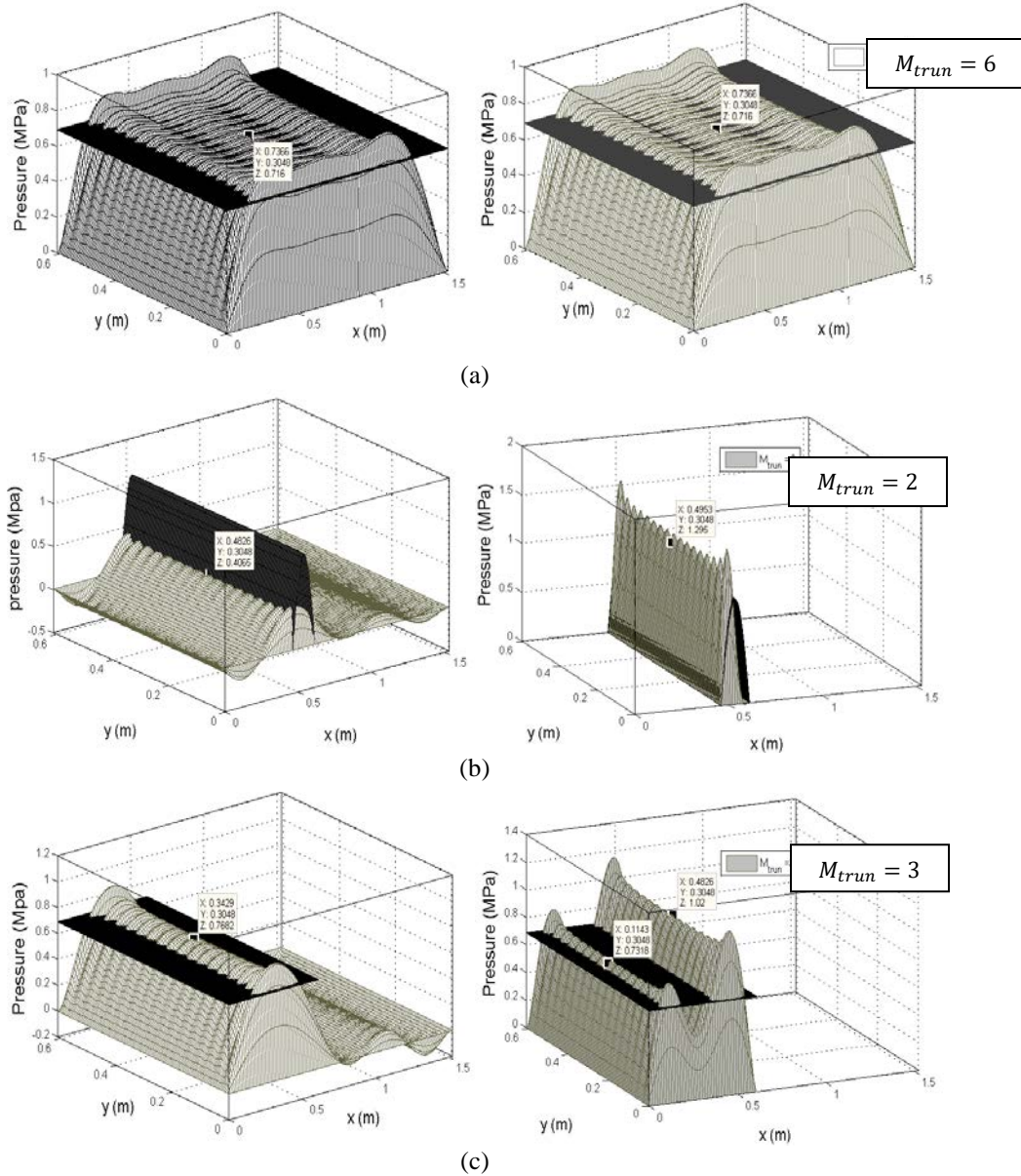
**Figure 3.9:** Pressure extracted by OPIT I and OPIT II for: **(a)** LC#1; **(b)** LC#2; **(c)** LC#3

## 3.7    Field Measurement Results

The presented algorithms are applied using the field measured strains by the IFMS system

on three specific days: Mar 18th, Apr 17th and May 01st, 2014. Photos showing the ice features

44

have been recorded by a camera installed above the measuring stiffened panel. The ice accumulation reaching over the top of the plate is observed on Mar 18th; an event of accumulated



(a)                                        (b)



(c)
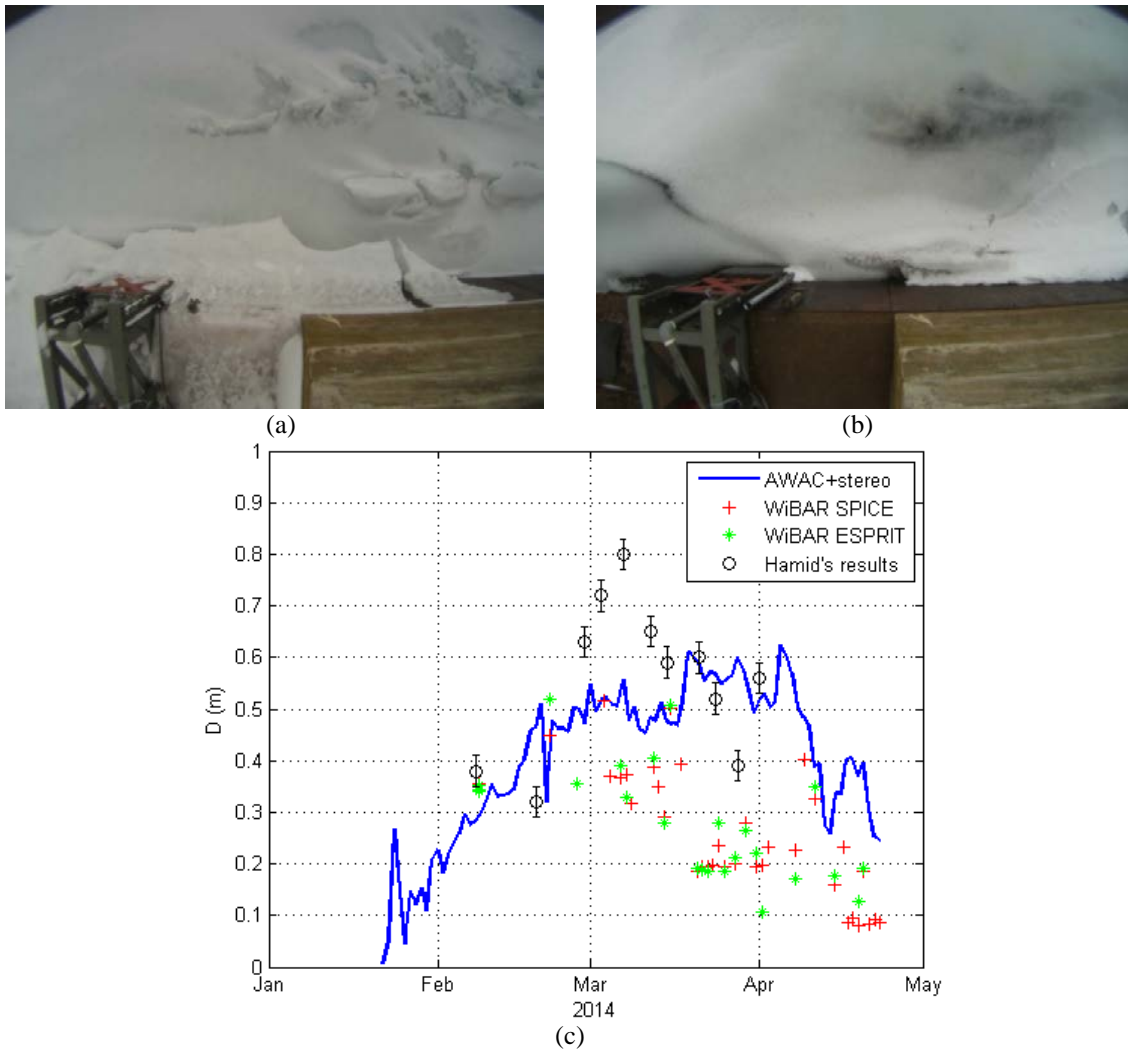
**Figure 3.10: (a)** March 18, 2014; **(b)** April 17, 2014; **(c)** ice thickness measurements from January to May 2014 (adapted from Nejati 2014; by David R. Lyzenga)

ice pushing against the plate on April 17th (Fig. 3.10a, Fig. 3.10b), during which east winds were recorded by NOAA (9099018 Marquette C.G, MI). Additionally, correlated data of ice thickness are measured from the Wideband Autocorrelation Radiometer ice thickness sensor (WiBAR) and Acoustic Wave and Current Profiler (AWAC) below the ice surface from the lake bottom (Nejati, 2014). The recorded ice thickness from February to May is plotted in Fig. 3.10c. These

measurements are used as inputs into the OPIT II algorithm for depth of ice coverage. Three linear horizontal gages were measured at 5 Hz on Mar 18$^{th}$; also, six horizontal strain gages (HLSG) were recorded at 1 Hz on Apr 17$^{th}$. The maximum strain variations recorded through the winter were observed on May 01$^{st}$ at 5 Hz in stormy weather with ice breaking-up. The pressures are calculated by both OPIT I and OPIT II algorithms from strain measurements on March 18$^{th}$ and April 17$^{th}$, with the estimated ice thickness applied as constraint for the OPIT II scheme. Ice thickness data were not available for the May 1$^{st}$ events.



(a)



(b)                                                      (c)
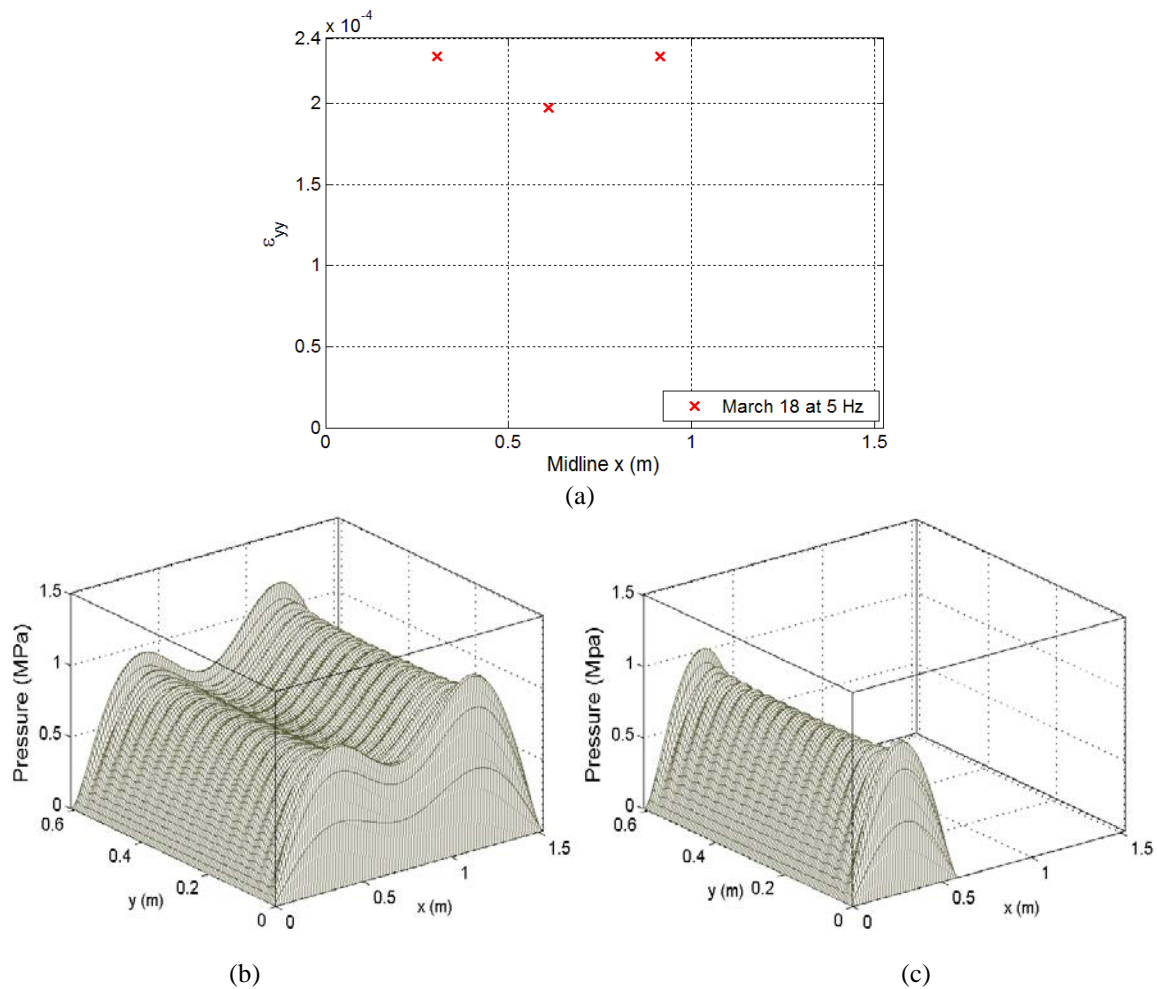
**Figure 3.11:** **(a)** Three strain inputs from March 18, 2014; **(b)** Pressure solution by OPIT I; **(c)** Pressure solution by OPIT II

46

The strain gage readings are examined for March $18^{th}$ at 5 Hz, April $17^{th}$ at 1 Hz and May $01^{st}$ at 5 Hz as the input for the inverse pressure calculation algorithms. The strain variations are measured at the HLSG and are subtracted from the unloaded zero strain gage $R_0$. The recorded strain values and the retrieved forcing are given in Fig. 3.11 to Fig. 3.13. The pressure calculated by SBT are in good agreement with the results obtained by OPIT I, justifying an averaging effect of OPIT I by assuming pressure terms over the entire plate (Table 3.3).

Strain gage readings on rib #1, rib #3, and rib #5 are recorded as input for pressure extraction on March $18^{th}$ at a sampling frequency of 5 Hz (Fig. 3.11a). Peak ice pressure is calculated as 0.84 MPa or 1.04 MPa through OPIT I; the OPIT II estimates the peak pressure to be 0.90 MPa with the constraint of ice thickness to be 0.6 m covering from the top of the plate (Fig. 3.11b). Six strain gages are recorded on April $17^{th}$; it is observed that the OPIT II estimates the peak ice contact pressure to be 1.35 MPa over the ice-covered area, which is slightly larger than the peak values calculated from OPIT I (Fig. 3.12).

Four strain gages on rib#1, rib#3, rib#5, and rib#7 showed the maximum strain variation through the winter season on May 01. Maximum ice contact pressure is calculated to be 3.5 MPa using the OPIT I algorithm with the given strain inputs shown in Fig. 3.13a and 3.13b; the calculated pressure is plotted in Fig. 3.13c. Note that the preliminary assessments of peak ice pressures are consistent with previous findings summarized by Bjerkås (2007) (Fig. 3.14). Additionally the peak lake ice measurements compare closely with this curve developed for prediction of extreme pressures for sea ice impacts as shown in Fig. 3.15 (Tõns et al., 2015), which of particular interest is the lower curve for first year sea ice.
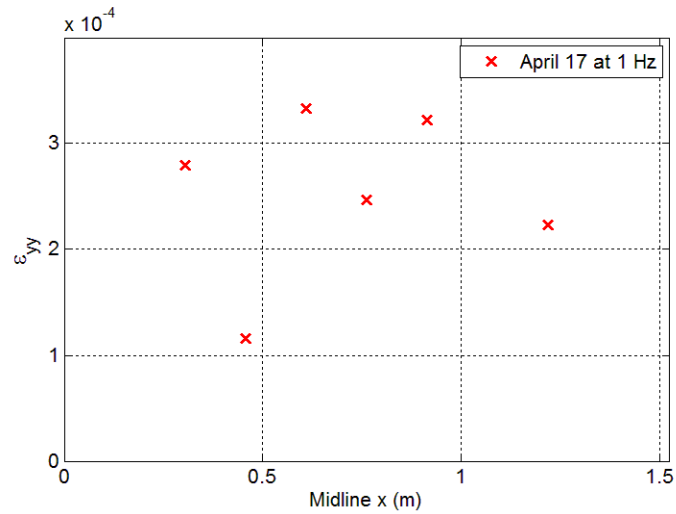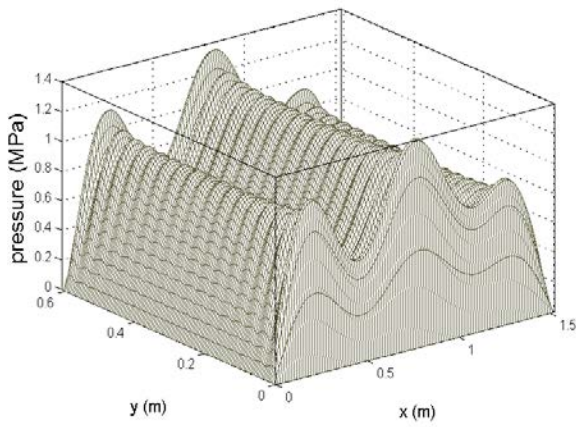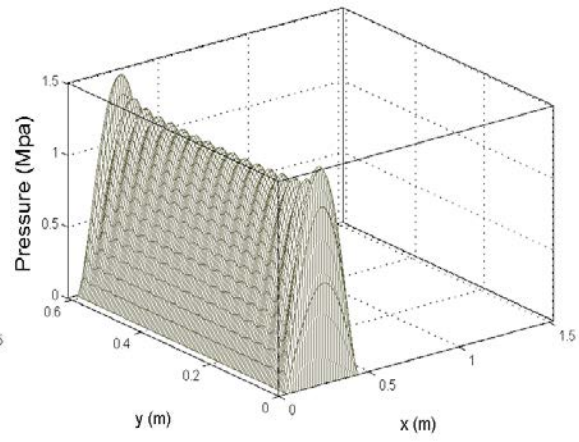
**Figure 3.12: (a)** Six strain inputs from April 17, 2014; **(b)** pressure solution by the OPIT I; **(c)** Pressure solution by OPIT II

(a)



(b)                                                                (c)
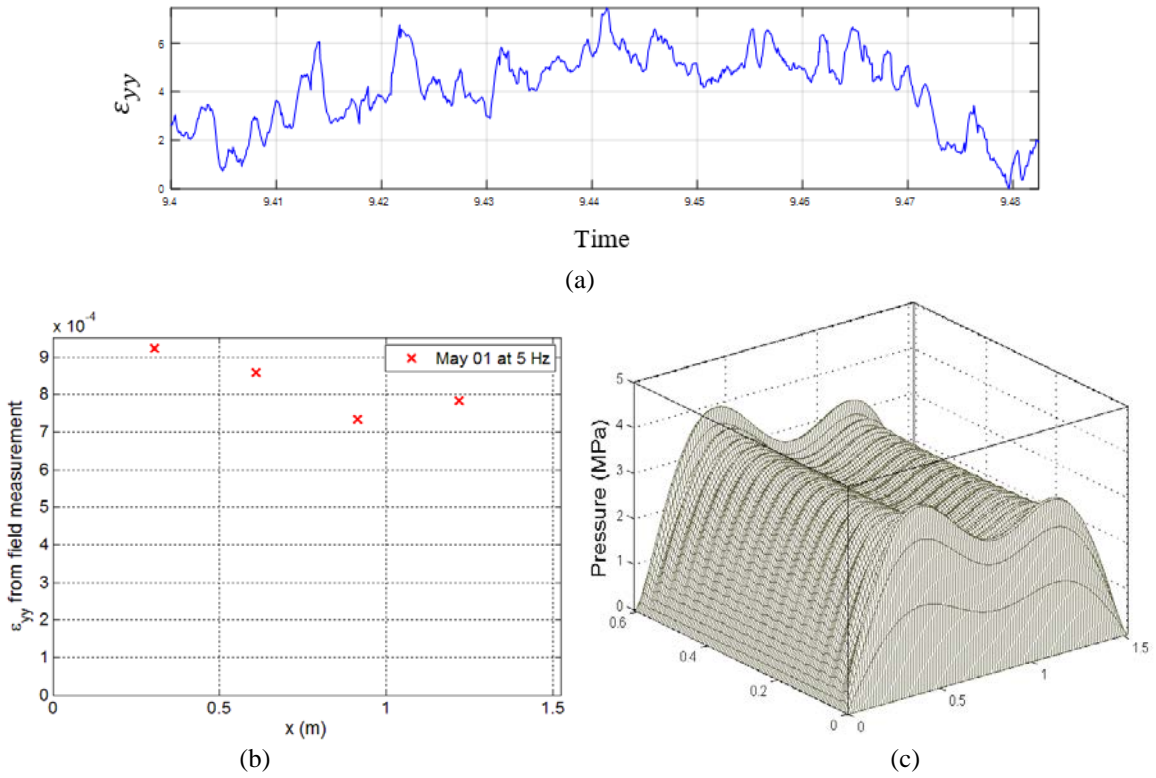
**Figure 3.13: (a)** Strain measurments on rib #5 on May 1st; **(b)** three input strains; **(c)** pressure solution by OPIT I
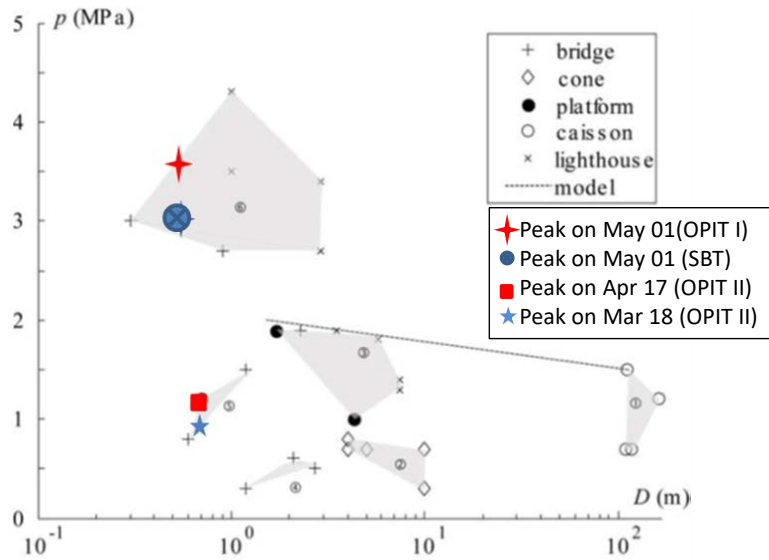


**Figure 3.14:** Effective ice pressure vs. the structural width (adapted from Bjerkås 2007)

49
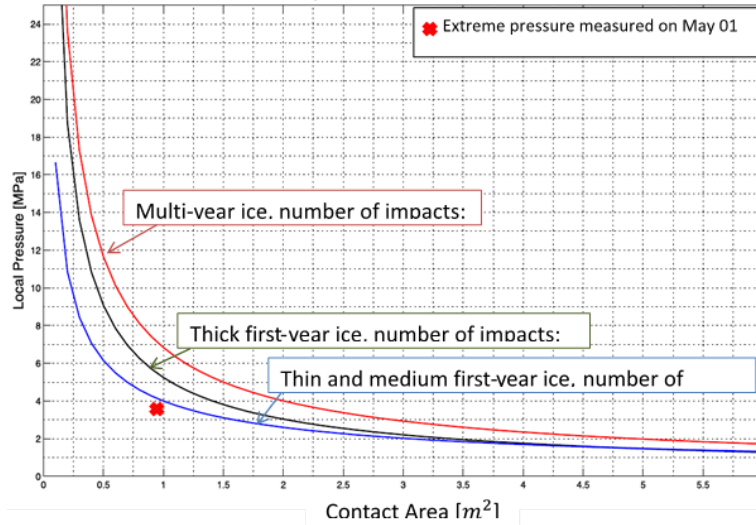
**Figure 3.15:** Predicted extreme load pressure for the specific route and comparison to the extreme load pressure measured by IFMS on May 1 (adapted from Tõns et al. 2015)

## 3.8 Conclusions

Inverse algorithms are formulated through forward analytical models to calculate the quasi-static pressure distribution on a stiffened plate. The stiffened panel is first modeled by strip beam theory (SBT) to estimate the uniform ice-loading over the entire plate and to extract the contact ice-load between two stiffeners. In order to reflect the variability of the ice-forcing, the plate is formulated as a structurally equivalent orthotropic plate to simulate the variable ice loading distribution along the depth of the plate (OPT I and OPT II).

In the forward formulations, the horizontal SBT and the OPT I are used when the stiffened panel is known to be fully covered by ice. While the horizontal SBT is limited to the form of uniform pressure; it is fast and stable under full ice-coverage. The OPT I is applicable for strain evaluation regardless of ice-covered area; moreover, the OPT I approximates closely to the exact strain solution at convergence. The vertical SBT and the OPT II set up the relationships between the ice-pressure distributions over a small portion of the plate to the structural strain-responses.

The vertical SBT calculates accurately the wavy deformation between the ribs, an effect which is not captured if using the orthotropic plate formulation. Nevertheless, the OPT II is notable for its faster convergence, especially when the ice-covered area is comparatively thin.

The inverse counterparts derived from the forward formulations compare well with the sophisticated finite element analysis with respect to different assumptions in the form of ice loads. In the second orthotropic method, the inverse coefficient matrix of the OPT II is truncated through a "low pass filter" by a minimum value $e$ via the TSVE optimization procedure, thus the stability of the matrix operation is retained. Three sample calculations using the FE input strains identify the stability and accuracy of the OPIT I method in predicting pressure distribution over the entire plate. The effectiveness of the OPIT II is observed in extracting the peak ice-pressure by retaining fewer pressure coefficient terms, especially for reduced span of ice-covered area.

In general, the inverse of the horizontal SBT is beneficial as an initial estimation of the averaged ice forcing when the number of structural inputs is extremely limited; the inverse of the vertical SBT provides a close estimation for contact ice-forcing between the ribs given the availability of vertical strain measurements. The OPIT I is always recommended for its accuracy to extract the variable ice-forcing when several strain measurements are available and the ice thickness measurement is not available. Additionally, the number of coefficient terms obtained for convergence from the OPT I of 6 to 9 indicates the optimal number of strain deployments for this system. The OPIT II is notably efficient in approximating the amplitude of contact ice forcing, if the ice thickness measurement for the span of the ice-contact area is available. Finally, the combination of both OPIT I and OPIT II is encouraged: first to get an evaluation of the distribution of the ice forcing over the entire plate, then to obtain more acute contact ice force amplitudes if the ice thickness measurements are available.

The variable loading caused by the coupled effect of ice, wind and thermal forcing has been retrieved using the strain measurements recorded by the IFMS instrumentation through the winter season 2013-2014. Maximum pressure forcing of 3.54 MPa is observed on May 01 by OPIT II calculation, while a peak average pressure about 0.90 MPa to 1.30 MPa were found based on the strain measurements on April 17 and March 18, 2014.

**Table 3.1**：Analytical strain evaluations compared to FE results (under LC#1)

| Strain | SBT | OPT I at M=6 | FE |
|---|---|---|---|
| **Avg. Horizontal Linear Strain at Rib#1 to Rib#5, Rib7** | $1.95 \times 10^{-4}$ | $2.03 \times 10^{-4}$ | $2.18 \times 10^{-4}$ |
| **Avg. Vertical Linear Strain at $x = 0.4m, 0.7m, 1.0n$** | $2.26 \times 10^{-5}$ (Fixed ends) $6.79 \times 10^{-5}$ (Pinned ends) | | $2.21 \times 10^{-5}$ |

Note: SBT=Strip Beam Theory; OPT=Orthotropic Plate Theory; FE=Finite Element.

**Table 3.2**：Peak pressure value and integrated pressure over the ice covered area

| Load Condition | Peak Pressure Value (MPa) | | | Integrated Pressure Along Depth of Ice Coverage (KN/m) | | |
|---|---|---|---|---|---|---|
| | Exact Loading | Solution by OPIT I | Solution by OPIT II | Exact Loading | Solution by OPIT I | Solution by OPIT II |
| **LC#1** | 0.69 | 0.72 | 0.72 | 1050.0 | 912.3 | 912.3 |
| **LC#2** | 1.08 | 0.41 | 1.30 | 105.0 | 55.8 | 95.7 |
| **LC#3** | 0.69 | 0.77 | 1.03 | 414.0 | 332.0 | 333.0 |

**Table 3.3**：Calculated peak pressure for field measurements by the SBT and the OPIT methods

| Measurement date | Peak Pressure Value | | | |
|---|---|---|---|---|
| | Ice thickness (m) | solution by SBT (MPa) | solution by OPIT I (MPa) | Solution by OPIT II (MPa) |
| **Mar 18, 2014** | 0.6 | 0.81 | 0.85 and 1.04 | 0.90 |
| **Apr 17, 2014** | 0.4 | 1.18 | 1.01, 1.21 and 0.82 | 1.31 |
| **May 01, 2014** | -- | 3.27 | 3.55 and 2.95 | -- |

**Nonlinear Contact Dynamic Response Simulation of Matlock's Ice-structure**

**Interaction Model using Fourier Analysis**

## 4.1    Introduction

This model considers the nonlinearity of a simplified ice-structure interaction model (Matlock et al., 1971) and predicts the dynamic response for the vibrations at specific periodicity. Previous studies indicate that periodic behavior of ice-structure interaction is highly non-linear and difficult to predict due to geometrical variability in the intermittent ice breakage and contact to the structure (Karr et al., 1993). The average and maximum magnitude of the structural contact forces are determined for the structural motion responses (Jonkman, 2009 and Yu, 2014). The periodic cycles, the average contact forces and the magnitude of the oscillating force are key factors for estimating structural fatigue life.

It can be observed that the steady-state responses previously obtained were found by selection of initial conditions. However, due to the limited experimental volume, it's not feasible to examine all possible combinations of inputs. The aim here is to predict the behavior of the dynamic response at any specific periodicity by expanding the dynamic equations of motion using Fourier analysis.

Based on Matlock's model, Karr et al. (1993) discussed the actual force time histories which show oscillations and are highly dependent upon the initial velocities and physical

properties of the ice-structure dynamic system. Forces intermittently rise and drop with respect to the deflection and breakage of the ice-teeth; the cyclical forces thus form an intermittent repeating process. This dynamic system is complicated by the ice deformation response, variation in ice-properties, geometry of the contact interface, as well as the dynamics of repeated impacts in each cycle. The imperfect system may have random variation in the ice-pitch, ice-stiffness and ice-strength to reflect the complexity of a real problem. However, the perfect system discussed here is argued to be representative of the more complicated imperfect system by showing similar characteristics.

Many mathematical approaches have been applied to solve non-linear dynamic system response with similar features of intermittent contact forces. Wang (1994) used the Trigonometric Collocation method to eliminate the need to evaluate the integrals of systems of mild non-linearity. Wong et al. (1991) applied the Incremental Harmonic Balance (IHB) method to obtain all possible harmonic responses of unsymmetrical piecewise-linear systems. However, these methods are computationally expensive and cannot predict the specific periodicity and the oscillating amplitude. Karr et al. (1995) and Yu (2014) discussed periodic solutions for the Matlock's ice-structure interaction model from the closed-form piece-wise linear solution. Similarly, the orbits of the steady-state periodic responses are not predictable *a priori* due to the numerical integrations over time steps and the non-linear nature of the dynamic relations. The periodic solutions are found only by simulation from arbitrary initial conditions.

While it has been noted in previous research that an overshoot effect will occur at the jump discontinuity using finite Fourier series, the Gibbs constant can be applied to reduce the over shooting effect (Foster and Richards, 1991). David and Shu (1997) discuss the sufficiency of achieving the same order of accuracy as in the case of smooth functions by applying expansion

coefficients. We apply the traditional Gibbs constant $g = 0.1790$ to adjust the over shooting effect in calculation of the initial position of the structure in the dynamic system.

## 4.2    Mathematical Matlock's Ice Structure Interaction Model

Based on Matlock's (1971) ice-structure interaction model, a first-order approximation for the dynamic ice-structure interaction modeling is a mass-spring-dashpot system with a single degree of freedom (Figure 4.1a,b).



(a)                                    (b)
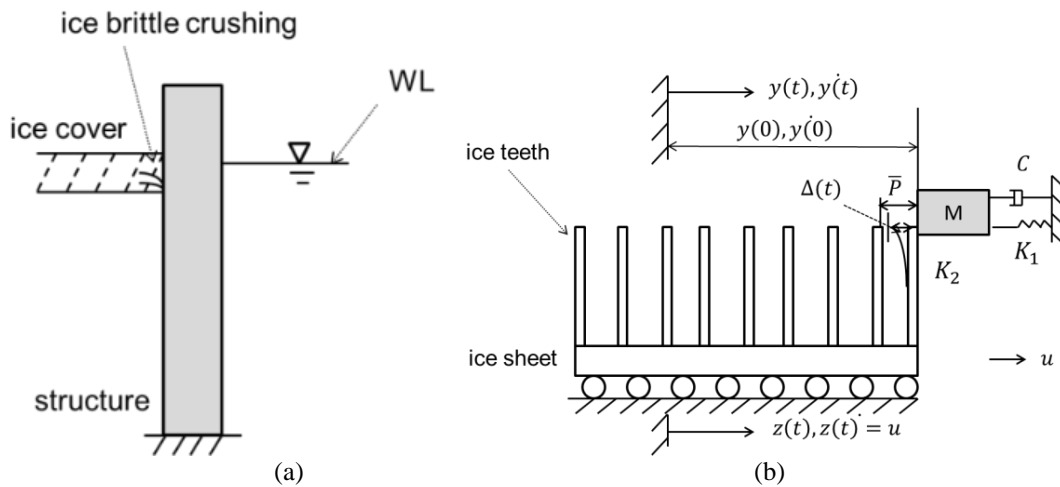
**Figure 4.1: (a)** Ice brittle crushing against an offshore structure; **(b)** Simplified Matlock's dynamic model for ice-structure interaction

The model parameters shown in Figure 1 are: $M$—oscillator mass; $C$—oscillator damping coefficient; $K_1$ – stiffness of oscillator spring; $K_2$ – ice teeth stiffness; $y(t)$ –displacement of the mass oscillator; $z(t)$—displacement of the ice sheet; $\Delta(t)$– deflection of ice-tooth; $\bar{P}$- distance between teeth interval (ice pitch); $u$—constant velocity of the ice-sheet in the $y$ direction.

Following the normalization procedure of Karr et al. (1993), we define the non-dimensional system parameters with respect to the structure's stiffness $K_1$ and the maximum ice forcing $F_{max}$ on the oscillator due to the ice teeth deflection at its maximum:

$$k_{ice} = \frac{K_2}{K_1}, \ \delta = \frac{\Delta}{\Delta_{max}}, \ \bar{y} = \frac{F_{max}}{K_1}$$

$$x = \frac{y}{\bar{y}}, \ U = \frac{u}{\bar{y}}, \ p = \frac{\bar{p}}{\bar{y}}, \ z_0 = \frac{z(\tau = 0)}{\bar{y}} \tag{4.1}$$

Time is normalized with respect to the natural angular velocity of the structure $\omega_n$, $N$ is the number of ice-breakage during each cycle of movement, hence:

$$\tau = \omega_n t \quad \omega_n^2 = \frac{K_1}{M} \quad T = \frac{Np}{U} \tag{4.2}$$

where $T$ is the normalized period for a single cycle. Substituting the parameters in Eq. (4.1) and Eq.(4.2) into the equations of motion, we obtain the governing differential equations with non-dimensionalized parameters as follows:

$$\ddot{x}(\tau) + 2\zeta \dot{x}(\tau) + x(\tau) = \begin{cases} 0, \ \delta \leq 0 \ or \ \delta = 1 \\ k_{ice}[z_0 + U\tau - x(\tau) - p(i-1)], \ 0 < \delta < 1 \end{cases} \tag{4.3}$$

Defining $d = p(i-1)$, the tooth deflection at the initial point $\delta(0)$ is 0. The kinematic expression for tooth deflection $\delta(\tau)$ is:

$$\delta(\tau) = [z_0 - x(\tau) + U\tau - d]k_{ice} \tag{4.4}$$

In an effort to expand the deflection $\delta(\tau)$ in a Fourier series, it's assumed that no teeth separate from the mass during each cycle of movement. This assumption implies immediate contact with the following tooth at the fracture of a previous tooth and it is justified in the perfect

dynamic system where the evenly distributed teeth pitch $\bar{P}$ equals the maximum tooth deflection $\Delta_{max}$. Rearranging Eq. (4.3) by applying the constraint of $0 \le \delta \le 1.0$ yields:

$$\ddot{x}(\tau) + 2\zeta\dot{x}(\tau) + (1 + k_{ice})x(\tau) = k_{ice}[z_0 + U\tau - d] \tag{4.5}$$

For a periodicity of N-teeth breakage per cycle (P-N response), we have:

$$UT = Np \tag{4.6}$$

The breakage occurs at time $\tau = \alpha_i T$, where $i = 1..(N-1), N$; $\alpha_i$ is the time ratio within one cycle of period $T$ when the $i^{th}$ tooth breakage occurs, and $\alpha_N = 1$. The last two terms in Eq. (4.5) can then be expressed by the Heaviside step function as follows:

$$U\tau - d = U\tau - pH\{\tau - \alpha_1 T\} - pH\{t - \alpha_2 T\} \dots - pH\{t - \alpha_N T\} \tag{4.7}$$

Defining $g(\tau) = k_{ice}(z_0 + U\tau - d)$, $g(\tau)$ is expanded in a Fourier series:

$$g(\tau) = k_{ice}(z_0 + U\tau - d) = z_0 k_{ice} + Utk_{ice} - k_{ice}p \sum_{i=1}^{i=N} H\{t - \alpha_i T\}$$

$$= \frac{a_0}{2} + \sum_{n=1}^{\infty}[a_n \cos(n\omega\tau) + b_n \sin(n\omega\tau)] \tag{4.8}$$

The Fourier coefficients are calculated as:

$$a_0 = 2k_{ice}z_0 - Npk_{ice} + 2pk_{ice} \sum_{i=1}^{N} \alpha_i$$

$$a_n = \frac{pk_{ice}}{\pi n} \sum_{i=1}^{N} \sin(2\pi n \alpha_i) \tag{4.9}$$

$$b_n = -\frac{pk_{ice}}{\pi n} \sum_{i=1}^{N} \cos(2\pi n \alpha_i)$$

Substituting Eq. (4.9) into Eq. (4.5), the steady state displacement trajectory $x(\tau)$ is:

$$x(\tau) = \frac{a_0}{2(1+k_{ice})} + \sum_{n=1}^{\infty} \frac{[a_n \cos(nr\tau - \phi_n) + b_n \sin(nr\tau - \phi_n)]}{\sqrt{\beta_n}} \tag{4.10}$$

where

$$r = \frac{2\pi}{T} \tag{4.11}$$

$$\beta_n = [(1 + k_{ice}) - (nr)^2]^2 + (2\zeta nr)^2 \tag{4.12}$$

$$\phi_n = atan[\frac{2\zeta nr}{1+k_{ice}-(nr)^2}] \tag{4.13}$$

The changes in displacement between two points of breakage are expressed by the following relation, where $q = 1, 2, \dots (N - 1)$:

$$x(\tau)|_{t=\alpha_q T} - x(\tau)|_{t=0} = p(q - N\alpha_q) \tag{4.14}$$

Substituting Eq.(4.14) into Eq (4.10), yields (N-1) equations for a specific Period-N response:

$$F(\alpha_q) = \sum_{n=1}^{\infty} \frac{1}{n\sqrt{\beta_n}} \{\sum_{i=1}^{N} \sin(2n\pi\alpha_i) [cos\phi_n - \cos(2\pi n\alpha_q - \phi_n)] +$$

$$\sum_{i=1}^{N} \cos(2n\pi\alpha_i) [sin\phi_n + \sin(2\pi n\alpha_q - \phi_n)]\} - \frac{\pi}{k_{ice}}(q - N\alpha_q) = 0 \tag{4.15}$$

Furthermore, recalling the kinematic relationship for tooth deflection in Eq. (4.4) and the maximum deflection limit $\delta_{max} = 1.0$, we obtain the initial location $z_0$ for the ice sheet at time $\tau = 0$ as follows:

$$z_0 = -\frac{Npk_{ice}}{2} + pk_{ice} \sum_{i=1}^{N} \alpha_i + (1 + k_{ice}) \sum_{n=1}^{\infty} \frac{(a_n cos\phi_n - b_n sin\phi_n)}{\sqrt{\beta_n}} \tag{4.16}$$

The initial velocity of the oscillator at $\tau = 0$ is calculated as:

$$\dot{x}(\tau)|_{\tau=0} = \sum_{n=1}^{\infty} \frac{nr(a_n sin\phi_n + b_n cos\phi_n)}{\sqrt{\beta_n}} \tag{4.17}$$

## 4.3    Periodic Motion Response Predictions

To seek the motion response for a specific periodicity, we first assume that the number of tooth breakages is $N$ for each cycle. The $N^{th}$ element $\alpha_N$ of the vector $\boldsymbol{\alpha}$ equals 1.0, and the remaining elements $\alpha_1 .. \alpha_{N-1}$ are unknowns. The corresponding breaking time ratios $\alpha_i$ can be

59

determined numerically from the $(N-1)$ non-linear equations $F(\alpha)$, as expressed in Eq. (4.15). The corresponding time history of teeth deflection $\delta(\tau)$ is thus determined through the set $\boldsymbol{\alpha}$, but the $\boldsymbol{\alpha}$ must be examined to verify that the responses are within the constraints of $0.0 \leq \delta(\tau) \leq 1.0$. In the following sample calculations for a given system, periodic solutions of N=1 (P-1) to N=5 (P-5) have been examined and the calculated displacements are compared with the results from the closed-form solutions.

The system parameters used in the sample periodic motion predictions for both the Fourier analysis and the closed-form simulation are:

$$U = \frac{10}{54\pi}, \ p = \frac{2}{9}, \ k_{ice} = 4.5, \ \zeta = 0.06 \tag{4.18}$$

Effort is given to verify the accuracy of the predicted amplitude of motion and the occurrence of tooth-breakage for specific periodicity. The fixed point of breakage for the closed-form P-1 solution is $(0) = 0.56, \dot{x}(0) = -0.015$ . It is observed that the predicted displacement of P-1 response by Fourier analysis is in close agreement with the displacement simulated from the closed form solution (Figure 4.2a). However, at the time of tooth fracturing, it is observed that the displacement-time derivative from the Fourier simulation is less than the velocity obtained by the closed-form solution. The normalized velocity at breakage is -0.015 from the closed-form solution, and it is -0.37 from the Fourier simulation. The difference in velocity is caused by the Gibbs effect of overshooting at the point of discontinuity due to tooth-breakage. The ice-tooth deformation forcing obtained by Fourier analysis is gradual at the breakage of $\delta(\tau = \alpha_i T)$ rather than shifting directly to zero. The overshooting effect in time history of the tooth-deflection is estimated to be 0.09, which agrees with the product of Gibbs constant $g$ times one-half of the jump size at the point of breakage (Figure 4.2 b). There is thus a source of error in estimating the velocity of the mass at breakage due to the Gibbs effect. In fact, inputting the kinematic initial condition at

breakage from the calculated P-1 response into the closed-form simulator, a periodic solution of P-5 is obtained.

The $\boldsymbol{\alpha}$ components for P-3 response are calculated as $\alpha_1 = 0.095, \alpha_2 = 0.41$, which compares well to the vibrations in Karr et al.'s (1993) steady-state P-3 response (Figure 4.3). Less than 6.6% of difference in the amplitude of motion is found, and the tooth breakage occurrences are in close agreement. Also, similar observations are found for P-2 response.

In addition to this periodic response, another possible P-3 response is calculated from the Fourier analysis (Figure 4.4). Moreover, we find possible P-4 solutions which are missing from the previous closed-form solutions (Karr et al., 1993). One typical simulation is shown in Figure 4.4b. It is observed that both the P-3 and P-4 responses resemble a portion of the oscillating motion from the closed-form P-25 steady-state response (Figure 4.5a). This P-25 response is obtained by using the Fourier calculated breakage initial conditions from a P-3 response: $x(0) = 0.49, \dot{x}(0) = -0.48$. Another closed-form solution with static initial condition $x(0) = 0, \dot{x}(0) = 0$ is shown in Figure 4.4a. It is noticed that this response consists of transient indentations during which the mass sweeps through 5, 4, 2 and 3 tooth-breakages respectively. The amplitudes of the transient response from Figure 4.5b resemble the motion amplitudes from the P-3 to P-4 responses calculated by Fourier analysis (Figure 4.4, Figure 4.7) with the same number of tooth-breakage in one single sweeping cycle.

Finally, the time history of displacements for a P-5 response predicted by the Fourier analysis compares well to the steady-state closed-form solutions in terms of the motion of response and the tooth breakage occurrence (Figure 4.6). Furthermore, the predicted motion of amplitude for P-5 by Fourier analysis is in agreement with the transient response shown in Figure 4.5b for P-1 response with 5 teeth breaking in the first sweep. Closed-form solutions for steady-state P-1, P-

2, P-3, P-5 and P-25 responses have been recorded by random initial inputs. The P-5 response features the maximum oscillating magnitude from the Fourier periodic solutions from P-1 through P-5 responses. The transient motion resembling the P-5 response shown in Figure 4.5b is thus not negligible. Therefore the Fourier analysis can be used to estimate the extreme motions of the dynamic system for both transient and steady-state response.



(a)

(b)
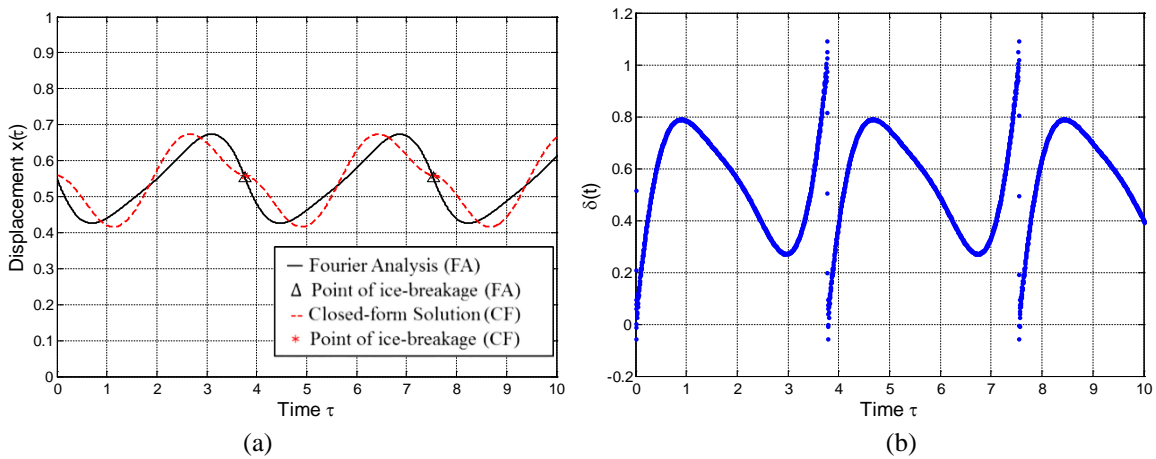
**Figure 4.2: (a)**: The P-1 response $x(\tau)$ obtained by Fourier series and closed-form solution**; (b)**: Tooth deflection $\delta(\tau)$ for a P-1 response by Fourier analysis



(a)

(b)
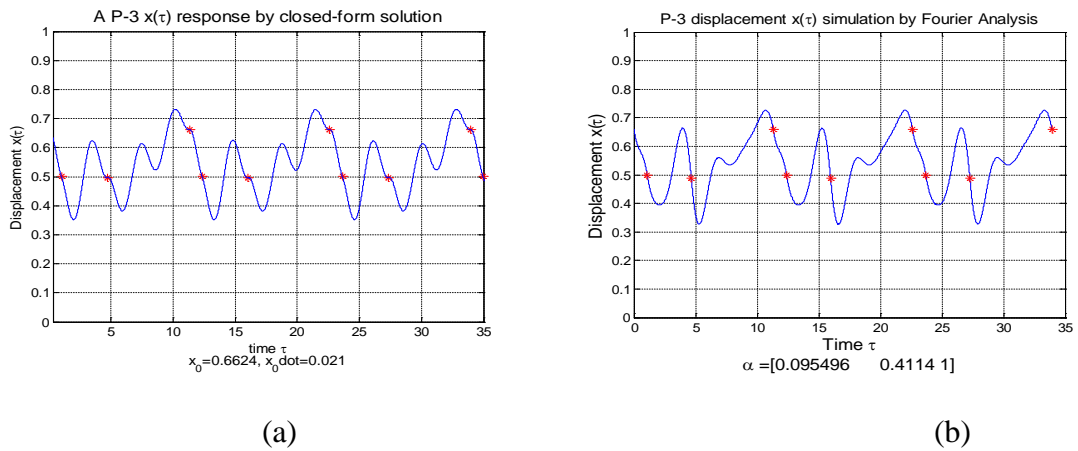
**Figure 4.3a:** A P-3 response by closed-form simulator ($x(0) = 0.66, \dot{x}(0) = 0.021$)
**Figure 4.3b:** A P-3 response predicted by Fourier series analysis ($\boldsymbol{\alpha} = [0.095, 0.41, 1.00]$)
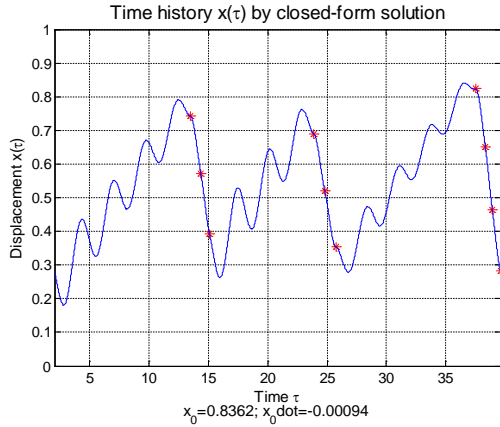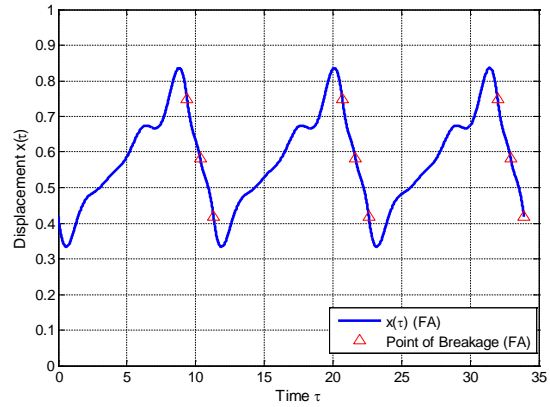
**Figure 4.4 (a)** The transient time history of displacement by closed-form simulation with $x_0 = 0.84, \dot{x}_0 = 0.0009$; **(b)** A P-3 response calculated by Fourier analysis ($\alpha = [0.83, 0.91, 1.00]$);
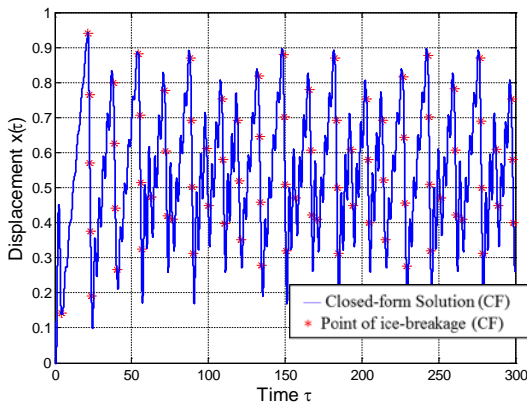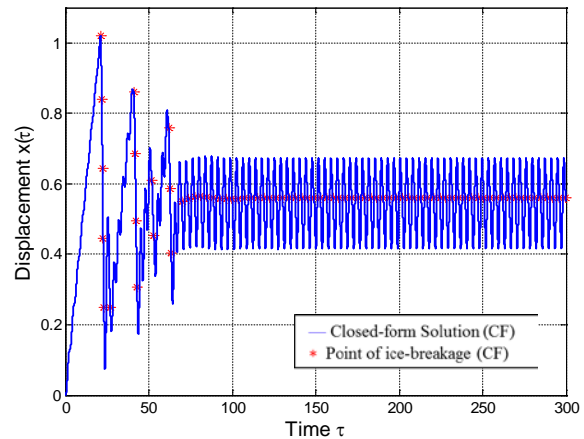


**Figure 4.5 (a)** Time history $x(\tau)$ by Closed-form solution with input $x(0) = 0.49, \dot{x}(0) = -0.48$; **(b)** Time history $x(\tau)$ by Closed-form solution with input $x(0) = 0, \dot{x}(0) = 0$
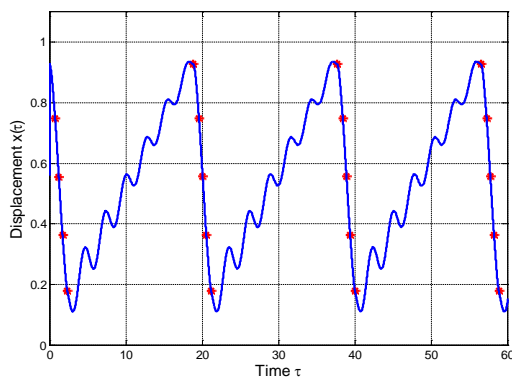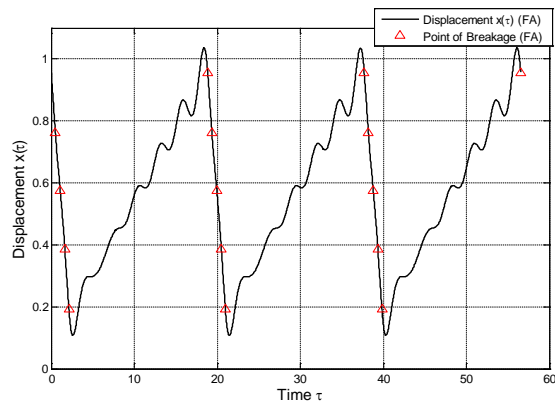


**Figure 4.6 (a)** A P-5 response by Closed-form simulator (initial condition $x_0 = 0.93, \dot{x} = -0.012$); **(b)** A P-5 response predicted by Fourier analysis (α=[0.027,0.058,0.087,0.11,1.00])

63
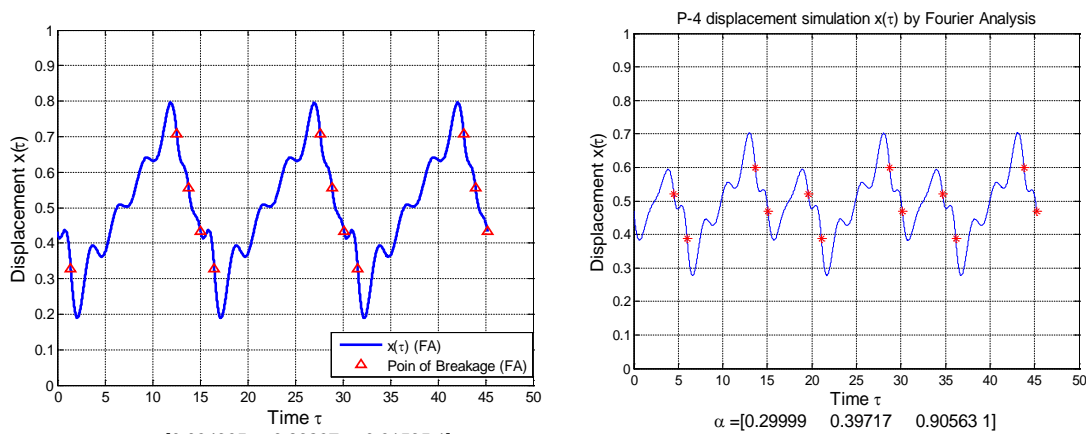
**Figure 4.7 (a)** A P-4 response calculated by Fourier analysis (α=[0.094,0.83,0.92,1.00]); **(b)** A P-4 response calculated by Fourier analysis (α=[0.30,0.39,0.91,1.00])

## 4.4 Proposed Validation using Offshore Wind Tower

As an extended application of the Matlock's ice structure interaction model using Fourier analysis, we convert the physical parameters input from other existed literature to compare the calculated dynamic response with the numerical simulated results and the experimental measurements. The analytical calculations will be carried out using the closed form solution and the Fourier analysis demonstrated in the previous section. The experimental measurements and the numerical results are referred from the previous research (Kärnä et al., 2010)

The model of an offshore wind turbine structure is depicted in Fig. 4.8 (Kärnä et al., 2010). The multi-modal analysis of the compliant offshore structure is studied and its eigenvalue and the corresponding mass for eigen-mode 1 and 4 are summarized in table 4.1. Note that the turbine blade is idling with no additional dynamic inputs for the dynamic response under the ice-crushing event.
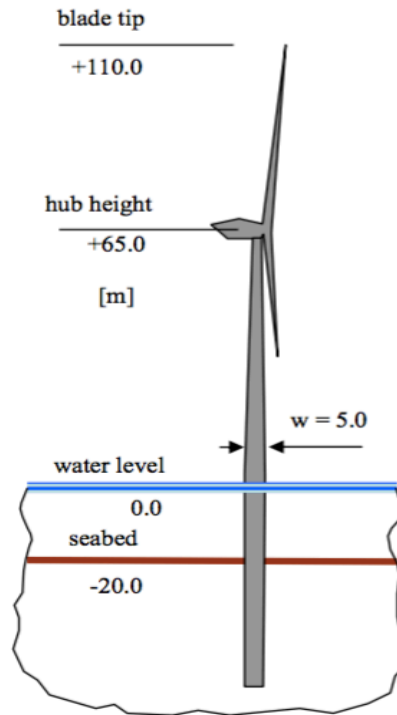
**Figure 4.8** A wind turbine exposed to ice actions (Kärnä et al., 2010)

It's observed that mode 1 at 0.37 Hz and mode 4 of 1.77 Hz dominate the dynamic response

of the vertical offshore structure during ice structure interaction simulation (Kärnä et al., 2010).

The response at the hub height of 65 m is dominated by mode 1 and the response at the water level

is dominated by mode 4. The velocity of the sheet ice is 0.1 m/s, while the ice thickness is 0.3 m.

In our Matlock's ice-structure interaction model, the ice pitch is assumed as equal to the ice

thickness. The conversion of the non-dimensional parameters from the physical wind tower model

to the Matlock's ice structure interaction model is shown in Table 4.2. Note that $\bar{y}$ is calculated

as $\frac{F_{max}}{K_1}$, where the maximum ice force is assumed as the maximum bending stress of ice multiply

by the width of the cylindrical structure in this scenario. $F_{max} = Dh\sigma_{max}$. Here we will use the

codes recommendation API RP-2N (1995) (Bjerkås et al., 2010) and obtained the $\sigma_{max} =$

$8.1(Dh)^{-0.5}$ Mpa= $6.6MPa$. Thus we apply the maximum ice force as $F_{max} = 9.9e6\ N$. The

comparison of the results using closed form solution and the Fourier series will be analyzed with the numerical simulation results by Kärnä et al. (2010).

**Table 4.1** Eigenfrequencies and related parameters (Kärnä et al., 2010)

|  |  | modes | |
|---|---|---|---|
|  | Description | 1 | 4 |
| $f_n$ (Hz) | Modal Frequency | 0.37 | 1.77 |
| $M_n$ (Kg) | Modal mass | 20500 | 7000 |
| $\xi_n^{tol}$ (%) | Total damping ratio | 1.6 | 2 |
| $\xi_n^{crt}$ (%) | Critical damping ratio | 8.1 | 99 |
| $K_1$ (N/m) | Modal stiffness $K_1 = 4\pi^2 f_n^2 M_n$ | 1.11e7 | 8.67e5 |
| $K_2$ (N/m) | Ice Stiffness |  |  |
| $w_n \left(\frac{rad}{s}\right) = 2\pi f_n$ | Modal angular velocity | 2.32 | 11.12 |
| $T_n = \frac{1}{f_n}$ (s) | Modal periodicity | 2.70 | 0.56 |

**Table 4.2** Matlock's ice-structure interaction parameter conversions

| $\overline{y}$ | structural deflection under quasi-static maximum ice force | $\overline{y} = \frac{F_{max}}{K_1}$ | | | | | |
|---|---|---|---|---|---|---|---|
| **Parameters** | Description | value | Non-dimensional parameter conversion | Expression | Mode 1 | Mode 4 |
| **u (m/s)** | Ice in-action velocity | 0.1 | $U$ | $U = \dfrac{u}{\overline{y}}$ |  |  |
| **h (m)** | Ice thickness | 0.3 | $p$ | $p = \dfrac{P}{\overline{y}}$ |  |  |
| **P (m)** | ice pitch | 0.3 | $T$ | $T = \dfrac{Np}{u}$ | 3N | 3N |
| **w (m)** | Cylindrical structural width | 5 | $\tau$ | $\tau = \omega_n t$ | 2.32t | 11.12t |
| **Fm (MN)** | Mean value of the ice action on an individual structure | 50 |  |  |  |  |

Another calculation example from the experiment measurement we propose to use is by Yue et al. (2009). Yue et al. (2009) discussed the dynamic ice force measured from the field test monopod structure of oil tankers of JZ9-3 in the north part of Bohai Bay, with maximum design thickness of 0.5m and an average ice in-action velocity reaching 1m/s. The field set up and the sketch of the level ice-crushing event is shown in Figure 9a and 9b. Further decomposition of the physical parameters will be carried out for a comparison of the result using the Matlock's ice structure interaction prediction model. It would be beneficial if the lock-in phenomenon observed in the vibration process can be properly predicted using the Matlock's Fourier analysis model.



(a)                                               (b)
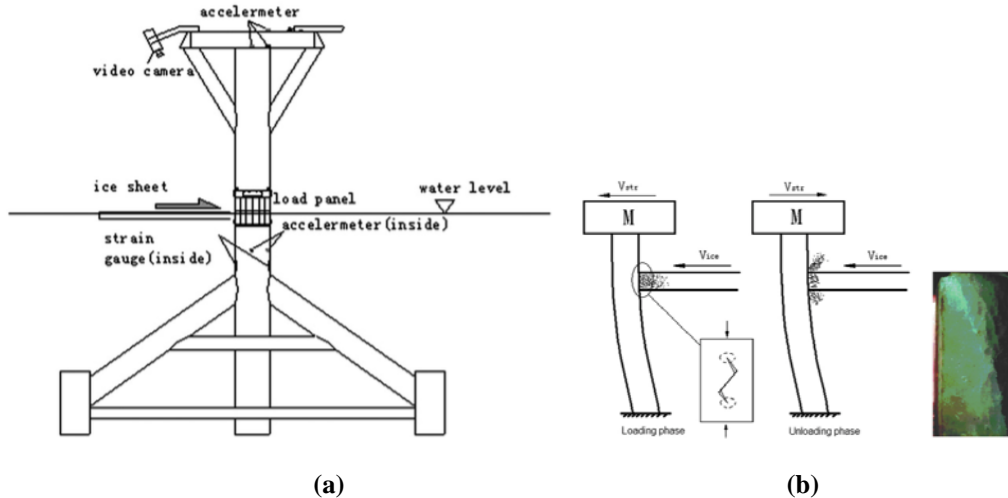
**Figure 4.9 (a)** Test system on the JZ9-3 mooring platform **(b)** sketch of physical mechanism of ice induced steady state vibration and ice specimen (Yue et al., 2009)

## 4.5    Conclusions

In this non-linear ice-structure dynamic simulation using Matlock's model, we expand the equations of motion in Fourier series, and set up the relationships among the system parameters to evaluate the responses for specific steady-state periodicity. Our approach establishes the non-linear dynamic equations through Fourier analysis with respect to the number of tooth-breakages $N$ per cycle. This method allows rapid estimation for the range of motion and the evaluation of structural

contact forces. The amplitudes predicted by our Fourier analysis solution correspond well to the simulation results obtained from closed-form solutions with random initial condition selections. Furthermore, the time ratios of breakage are accurately predicted thus the cyclic behavior can be analyzed accordingly. Also, with the calculated structural periodic responses, the mean value and the magnitude of the oscillating contact forces can be obtained. These output parameters are key factors for strength and fatigue life assessment. The previously un-detected periodic response of a P-4 is found through our Fourier solution. Further effort should be given to validate the basin of attractions given a representative system and more specific evaluation of the error range in the velocity predictions due to the Gibbs effect.

**Stiffened Plate Analysis by Treating Stiffeners as Discrete Energy Components Using Double Fourier Series Formulation**

## 5.1    Introduction

Researchers have multiple mathematical formulation following various simplified assumptions to analyze the stiffened plates. Green (1944) analyzed the double Fourier series results compared to classical orthotropic theory. He found that the double Fourier series is of satisfying accuracy in calculation of the bending moment with little algebraic manipulation. Eagle and Sewall (1968) utilized the Rayleigh-Ritz method with the allowance of coupling between both axial and circumferential modes for the displacement functions. A sine series solution has been extended to apply to the free vibration of orthotropic plates by Dickinson (1969). It was observed that the determinants for plates with all edges supported converge rapidly and the sine series solution can also be applied to systems built up from rectangular plates.

Xiang et al (1994) found an analytical model using Ritz method in the form of complete algebraic polynomials, which greatly reduced the computational effort compared to the previous FEA analyses. However, the polynomial formulation requires higher order of modes to include torsional effects. Srinivas and Rao (1970) argued that a three-dimensional displacement field for the composite plate is necessary and the solution is set up in the form of a double trigonometric

series. Meleshko (1997) reviewed the purely mathematical formulations for clamped plates and presented three different bi-harmonic solutions with infinite systems linear algebraic equations. It is argued that the superposition method is recommended for fast convergence for rectangular plates, and discussed the dominance effect of simply supported plate edges when the ratio of clamped edges is smaller than 0.5.

In a similar approach, Bhaskar and Kaushik (2004) etc. presented an exact solution methodology for orthotropic laminated plate based on superposition of double sine series solution derived from the principle of virtual work. This analysis was presented for arbitrarily loaded cross-ply plates with any combination of simply-supported and clamped edges. Qing et al. (2006) developed a novel mathematical model for the finite element on the basis of state-vector equation theory with excellent predictive capability for static and free-vibration of stiffened plates by separate consideration of plate and stiffeners. In the methods presented in this paper, Navier's double Fourier series formulation is utilized to approximate the transverse and in-plane displacement field at the mid-plane of the stiffened plate as an extended application of the plate solution summarized by previous researchers.

In this chapter, two models of the stiffened plates are developed. The first model referred to as a discrete energy method (DEM I) treats the effective centroids of the stiffened plate to be at the geometric centroids of the cross-sections. This model assumes zero in-plane displacement and strains from plate bending at the effective centroids. The effective centroids are calculated in both directions which are parallel to the edges of the rectangular plate. The second model (DEM II) formulates the displacement fields in double Fourier series for transverse and both in-plane directions that satisfy the boundary conditions of pinned edges along the mid-plane of the plate. This model achieves high accuracy in estimation of the structural responses comparable to

sophisticated FEA results, while eliminating the necessity of calculating either the effective centroids or the effective breadth of the representative sections.

## 5.2    Discrete Energy Method

### 5.2.1 Discrete Energy Method I (DEM I)

The plate stiffeners are aligned parallel to the x-axis or y-axis direction. Each of the stiffeners along one direction has the same constant structural properties. In the example analysis, the plate is stiffened with 3 horizontal stiffeners (x-stiffeners) as is shown in Fig. 5.1a. A double Fourier series formulation is applied for the displacement field $w(x, y)$ to satisfy simply supported boundary conditions. The displacement field is assumed to be identical over the depth of the plate, i.e., the transverse displacement field is independent of the z-coordinate. Let $m = 1..M$, $n = 1..N$, where $M$ is the order of coefficient terms to be retained along the $x$-direction, and $N$ is the order of terms be retained over the $y$-direction:

$$w(x, y) = \sum_{m=1}^{M}\sum_{n=1}^{N} W_{mn} \sin(\frac{m\pi x}{a})\sin(\frac{n\pi y}{b}) \qquad (5.1)$$

The variable pressure acting on the plate is prescribed using Fourier series as:

$$p(x, y) = \sum_{m=1}^{M}\sum_{n=1}^{N} P_{mn} \sin(\frac{m\pi x}{a})\sin(\frac{n\pi y}{b}) \qquad (5.2)$$

$W_{mn}$ and $P_{mn}$ are the Fourier coefficients for the displacement and pressure formulation accordingly. The position of the centroidal plane in either the x or y direction is found by assuming fully effective plating for the averaged cross-sections. Here, $t_x$ denotes the spacing of the x-stiffener as is shown in Fig. 5.2. As is common for orthotropic plates, the kinematic assumption is

that in-plane displacement fields $u(x,y,z)$ and $v(x,y,z)$ are zero at the centroidal plane in their respective coordinate direction. Thus, the in-plane displacements $u$ and $v$ are calculated using the rotational angle determined from the transverse displacement $w(x,y)$. The in-plane coordinate z is measured from the mid-plane of the plate using the relations $z_x = z - c_x$ and $z_y = z - c_y$, where $c_x$ and $c_y$ are the z-coordinates of the effective centroid position in either x-stiffener or y-stiffener aligned direction. The in-plane displacements are expressed as:

$$u(x,y) = -(z-c_x)\frac{\partial w}{\partial x}; \quad v(x,y) = -(z-c_y)\frac{\partial w}{\partial y} \tag{5.3}$$

The total strain energy of the plate is calculated through the integration of stress and strain products over the entire plate (excluding the stiffener), which yields the following:

$$U_P = \frac{E}{2(1-\upsilon^2)}\iint_R \int_{-h_p/2}^{h_p/2} [\varepsilon_{xx}^2 + 2\upsilon\varepsilon_{xx}\varepsilon_{yy} + \varepsilon_{yy}^2 + 2(1-\upsilon)\varepsilon_{xy}^2]dzdxdy \tag{5.4}$$

Introducing the coefficient $D = Eh_p^3/12(1-\upsilon^2)$, and decomposing the strain energy of the plate $U_p$ into bending strain energy $U_{pb}$ and membrane strain energy $U_{pm}$, the total strain energy of the plate is calculated as:

$$
\begin{aligned}
U_p &= U_{pb} + U_{pm} = \\
&\frac{D}{2}\iint_A [(\frac{\partial^2 \omega}{\partial x^2})^2 + (\frac{\partial^2 \omega}{\partial y^2})^2 + 2\upsilon\frac{\partial^2 \omega}{\partial x^2}\frac{\partial^2 \omega}{\partial y^2} + 2(1-\upsilon)(\frac{\partial^2 \omega}{\partial y\partial x})^2]dA \\
&+\frac{C}{2}\iint_A [(\frac{\partial u_s}{\partial x})^2 + (\frac{\partial v_s}{\partial y})^2 + 2\upsilon\frac{\partial u_s}{\partial x}\frac{\partial v_s}{\partial y} + \frac{1-\upsilon}{2}(\frac{\partial u_s}{\partial y} + \frac{\partial v_s}{\partial x})^2]dA
\end{aligned}
\tag{5.5}
$$

Here, $u_s$ and $v_s$ are the in-plane displacement at the mid-plane of the plate, and $C = Eh_p/(1-\upsilon^2)$. Rewriting Eqn. (5.5) by introducing the traditional plate rigidity coefficients $D_x$, $D_y$, $D_{xy}$ and $D_s$ as $D_x = D + Cc_x^2$, $D_y = D + Cc_y^2$, $D_{xy} = 2v(D + Cc_xc_y)$, $D_s = (1-v)[2D + (C_x + C_y)^2/2$, and substituting the in-plane displacement fields $u_s$, $v_s$ in terms of $w(x,y)$:

$$U_p = \frac{1}{2} \iint_A [D_x w_{,xx}^2 + D_y w_{,yy}^2 + D_{xy} w_{,xx} w_{,yy} + D_s w_{,xy}^2] dA \qquad (5.6)$$

The stiffeners' strain energy $U_S$ is composed of the beam axial strain energy, beam bending strain energy and the beam torsional strain energy. It is assumed that the warping torsional strain energy is negligible. The strain energy for x-stiffeners $U_{s-x}$ is expressed as:

$$U_{s-x} = \sum_{y_s} \left[ \frac{1}{2} \int_0^a EI_{ey} (\frac{\partial^2 \omega}{\partial x^2})^2 |_{y=y_s} dx + \frac{1}{2} \int_0^a GJ_x (\frac{\partial^2 \omega}{\partial x \partial y})^2 |_{y=y_s} dx \right] \qquad (5.7)$$

For y-stiffeners the strain energy $U_{s-y}$ is calculated by the following expression:

$$U_{s-y} = \sum_{x_s} \left[ \frac{1}{2} \int_0^b EI_{ex} (\frac{\partial^2 \omega}{\partial y^2})^2 |_{x=x_s} dy + \frac{1}{2} \int_0^b GJ_y (\frac{\partial^2 \omega}{\partial x \partial y})^2 |_{x=x_s} dx \right] \qquad (5.8)$$

In the above two expressions, the $I_{ex}$ and $I_{ey}$ are the moment of inertia of the stiffener with respect to the effective centroid of the cross-section along x and y axis respectively (Fig. 5.2). Additionally, $J_x$ and $J_y$ are the torsional constants of the x-stiffener and y-stiffener respectively.

Expanding the stiffeners' strain energy found from Eqn. (5.7) and (5.8) in terms of the displacement field yield:

$$U_s = \sum_{y_s} \sum_{m=1}^M \sum_{n=1}^N \sum_{j=1}^N \left[ \frac{m^4 \pi^4 I_{ex} E}{4a^3} W_{mn} W_{mj} \sin(\frac{\pi n y_s}{b}) \sin(\frac{\pi j y_s}{b}) + \frac{m^2 nj GJ_x \pi^4}{4ab^2} W_{mn} W_{mj} \cos(\frac{\pi n y_s}{b}) \cos\left(\frac{\pi j y_s}{b}\right) \right]$$

$$+ \sum_{x_s} \sum_{m=1}^M \sum_{i=1}^M \sum_{n=1}^N \left[ \frac{n^4 \pi^4 I_{ey} E}{4b^3} W_{mn} W_{in} \sin(\frac{m \pi x_s}{a}) \sin(\frac{i \pi x_s}{a}) + \frac{n^2 mi GJ_y \pi^4}{4a^2 b} W_{mn} W_{in} \cos(\frac{m \pi x_s}{a}) \cos(\frac{i \pi x_s}{a}) \right]$$

$$(5.9)$$

The external potential energy $V$ is written as a function of the displacement and pressure terms integrated over the entire plate as:

$$V = \iiint_v w(x, y) p(x, y) dv = \sum_{m=1}^M \sum_{n=1}^N \frac{ab W_{mn} P_{mn}}{4} \qquad (5.10)$$

Applying the principle of stationary total potential energy $(\partial U_s + \partial U_p)/\partial W_{mn} - \partial V/\partial W_{mn} = 0$, the deformation coefficients are thus calculated from the Fourier pressure terms. The resulting system of equations (M x N) is used to solve for $W_{mn}$ in terms of $P_{mn}$. Taking the derivative of external strain energy $V$ in Eqn. (10) with respect to the displacement coefficients $W_{mn}$ yields:

$$\frac{\partial V}{\partial W_{mn}} = \frac{ab}{4} P_{mn} \tag{5.11}$$

Additionally, taking the derivative of the total strain energy of the stiffened panel $U$ with respect to the displacement coefficients $W_{mn}$ yields the following $M$ by $N$ equations:

$$\frac{\partial U}{\partial W_{mn}} = [\frac{bm^4\pi^4}{4a^3} + \frac{an^4\pi^4}{4b^3} + \frac{\upsilon m^2 n^2 \pi^4}{2ab} + \frac{(1-\upsilon)m^2 n^2 \pi^4}{2ab}] \cdot DW_{mn}$$

$$+ \sum_{y_s} \sum_{j=1}^{j=N} \left[ \frac{m^4\pi^4}{2a^3} EI_{ex} \sin(\frac{\pi n y_s}{b}) \sin(\frac{\pi j y_s}{b}) + \frac{m^2 nj\pi^4}{2ab^2} GJ_x \cos(\frac{n\pi y_s}{b}) \cos(\frac{j\pi y_s}{b}) \right] \cdot W_{mj}$$

$$+ \sum_{x_s} \sum_{i=1}^{i=M} \left[ \frac{n^4\pi^4}{2b^3} EI_{ey} \sin(\frac{m\pi x_s}{a}) \sin(\frac{i\pi x_s}{a}) + \frac{mn^2 i\pi^4}{2a^2 b} GJ_y \cos(\frac{m\pi x_s}{a}) \cos(\frac{i\pi x_s}{a}) \right] \cdot W_{in}$$

$$= A_{o_{mn}} W_{mn} + \sum_{y_s} \sum_{j=1}^{j=N} B_{o_{mn\_s\_j}} W_{mj} + \sum_{x_s} \sum_{i=1}^{i=M} C_{o_{mn\_s\_i}} W_{in} \tag{5.12}$$

Analyzing Eqn. (11) and (12) and re-writing the expression in the form of linear matrices operations yield:

$$[A_{o_{mn}}]\{W_{mn}\} + \sum_{y_s}[B_{o_{mn}}]_s\{W_{mn}\} + \sum_{x_s}[C_{o_{mn}}]_s\{W_{mn}\} = [E_{o_{mn}}]\{P_{mn}\} \tag{5.13}$$

Here $[A_{o\,mn}]$, $[B_{o\,mn}]$, $[C_{o\,mn}]$ and $[E_{o\,mn}]$ are $(M \times N)$ by $(M \times N)$ coefficient matrices obtained from Eqn. (12), and $\{W_{mn}\}$ is the the $(M \times N)$ by 1 column matrix for Fourier coefficients of the displacement field for $m = 1..M, n = 1..N$:

$$\{W_{mn}\} = [W_{11}\ W_{12}\ ..W_{1N}\ W_{21}..W_{2N}\ ...W_{M1}..W_{MN}]^T \tag{5.14}$$

Thus, the expression for calculation of the displacement Fourier coefficient terms $\{W_{mn}\}$ is:

$$[COE_{mn}]\{W_{mn}\} = [E_{o_{mn}}]\{P_{mn}\} \qquad (5.15)$$

Here $[COE_{mn}] = [A_{o_{mn}}] + \Sigma[B_{o_{mn}}]_s + \Sigma[C_{o_{mn}}]_s$ and $[E_{o_{mn}}]$ can be written via Eqn. (5.12) as

coefficient matrices. Finally, the Fourier coefficient terms of the displacement are found through

the linear algebra operation:

$$\{W_{mn}\} = inv[COE_{mn}][E_{o_{mn}}]\{P_{mn}\} \qquad (5.16)$$



(a)                                        (b)
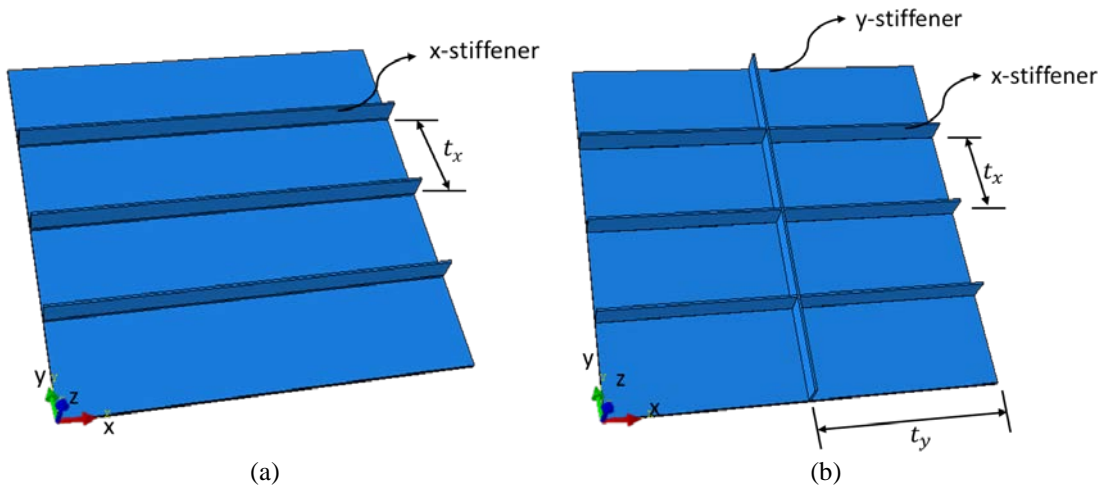
**Figure 5.1:** Simply supported plate with single-directional **(a)** or orthogonal stiffeners **(b)**
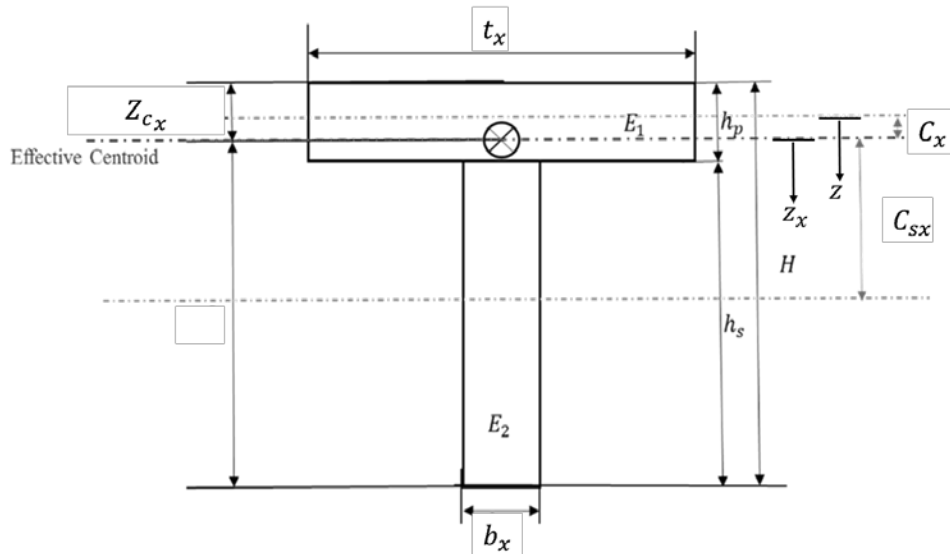


**Figure 5.2:** X-stiffened cross-section and the effective centroid location of the neutral plane (y-direction edge)

### 5.2.2 Discrete Energy Method II (DEM II)

For the DEM II formulation, the same boundary condition of simple support along the four edges of the plate are used. The transverse displacement field and the pressure field are expressed in Eqn. (5.1) and Eqn. (5.2). Introducing the in-plane displacement function $u_0(x, y, z = 0)$ and $v_0(x, y, z = 0)$ at the mid-plane of the plate in addition to the transverse displacement is found here:

$$u_0(x, y) = \sum_m \sum_n A_{mn} \sin(\frac{m\pi x}{a}) \sin(\frac{n\pi y}{b}) \tag{5.17}$$

$$v_0(x, y) = \sum_m \sum_n B_{mn} \sin(\frac{m\pi x}{a}) \sin(\frac{n\pi y}{b}) \tag{5.18}$$

Thus, the linear strain of the plate is expressed as a function of the in-plane displacement fields $u_0$, $v_0$ and the transverse displacement field $w$ as follows:

$$\varepsilon_{xx} = \frac{\partial u_0}{\partial x} - z\frac{\partial^2 w}{\partial x^2} \tag{5.19}$$

$$\varepsilon_{yy} = \frac{\partial v_0}{\partial y} - z\frac{\partial^2 w}{\partial y^2} \tag{5.20}$$

Here $z$ is again measured from the mid-plane of the plate. Substituting the total strain energy with the displacement field expressed in Eqn. (5.17), (5.18) and Eqn. (5.1), the strain energy of the plate $U_p$ without stiffeners is:

$$U_p = \frac{D}{2}\sum_m\sum_n (\frac{\pi^4 b}{4a^3}m^4 + \frac{\pi^4 a}{4b^3}n^4 + \frac{\upsilon\pi^4}{2ab}m^2 n^2 + \frac{(1-\upsilon)\pi^4}{2ab}m^2 n^2)W_{mn}^2 + \sum_m\sum_n[\frac{Cm^2\pi^2 b}{8a} + \frac{C(1-\upsilon)n^2\pi^2 a}{16b}]A_{mn}^2$$

$$+ \sum_m\sum_n[\frac{Cn^2\pi^2 a}{8b} + \frac{C(1-\upsilon)m^2\pi^2 b}{16a}]B_{mn}^2 + \sum_m\sum_n\sum_i\sum_j \frac{2mnijC(1+\upsilon)}{(m^2 - i^2)(j^2 - n^2)}A_{mn}B_{ij}$$

$$\tag{5.21}$$

The stiffeners' strain energy $U_s$ is expressed as the sum of the bending strain energy, axial strain energy and torsional strain energy. For the general stiffening scenario, x-stiffeners are evenly distributed over locations of $y = y_s$, while y-stiffeners are distributed over the locations of $x = x_s$. Here $s = 1,2,3 \dots$ is the number of the ribs in either the x or y direction. Summing the strain energy at $y = y_s$ as $U_{sx}$, and at $x = x_s$ as $U_{sy}$ using the displacement fields expressed in Fourier series, the relationship of stiffeners' strain energy is obtained as:

$$
\begin{aligned}
U_s = \sum_{y_s} &\{\sum_m \sum_n \sum_j \frac{m^2\pi^2}{4a}EA_{sx}\sin(\frac{n\pi y_s}{b})\sin(\frac{j\pi y_s}{b})A_{mn}A_{mj} + \sum_m \sum_n \sum_i \sum_j \frac{(h_{sx}+h_p)EA_{sx}mi^3\pi^2}{a^2(i^2-m^2)}\sin(\frac{n\pi y_s}{b})\sin(\frac{j\pi y_s}{b})A_{mn}W_{ij} \\
&+ \sum_m \sum_n \sum_j [\frac{m^4\pi^4 I_{ex}E}{4a^3}\sin(\frac{n\pi y_s}{b})\sin(\frac{j\pi y_s}{b}) + \frac{m^2 njGJ_x\pi^4}{4ab^2}\cos(\frac{n\pi y_s}{b})\cos(\frac{j\pi y_s}{b})]W_{mn}W_{mj}\} \\
+ \sum_{x_s} &\{\sum_m \sum_n \sum_i \frac{n^2\pi^2}{4b}EA_{sy}\sin(\frac{m\pi x_s}{a})\sin(\frac{i\pi x_s}{a})B_{mn}B_{in} + \sum_m \sum_n \sum_i \sum_j \frac{(h_{sy}+h_p)EA_{sy}nj^3\pi^2}{b^2(j^2-n^2)}\sin(\frac{m\pi x_s}{a})\sin(\frac{i\pi x_s}{a})B_{mn}W_{ij} \\
&+ \sum_m \sum_n \sum_i [\frac{n^4\pi^4 I_{ey}E}{4b^3}\sin(\frac{m\pi x_s}{a})\sin(\frac{i\pi x_s}{a}) + \frac{n^2 miGJ_y\pi^4}{4a^2b}\cos(\frac{m\pi x_s}{a})\cos(\frac{i\pi x_s}{a})]W_{mn}W_{in}\}
\end{aligned}
$$

$$(5.22)$$

In Eqn. (5.22) $A_{sx}$ and $A_{sy}$ are the area of the cross section of the x-stiffener and y-stiffener respectively. $h_{sx}$ and $h_{sy}$ are the height of the x-stiffener or y-stiffener respectively, $h_p$ is the thickness of the plate. $I_{ex}$ and $I_{ey}$ are the moment of inertia of the x-stiffener or y-stiffener with respect to the mid-plane of the plate.

The external potential energy $V$ is written as a function of the displacements and pressure terms integrated over the entire plate in Eqn. (5.10). Applying the principle of stationary total potential energy, 3 sets of M by N equations with unknown coefficients $W_{mn}$, $A_{mn}$ and $B_{mn}$ are obtained as functions of the calculated pressure coefficients $P_{mn}$. Taking the stationary total potential energy with respect to $W_{mn}$, the first set of $M \times N$ equations for unknown coefficient variables are calculated as:

$$\frac{\partial U_p + \partial U_s}{\partial W_{mn}} = [\frac{bm^4\pi^4}{4a^3} + \frac{an^4\pi^4}{4b^3} + \frac{\upsilon m^2 n^2 \pi^4}{2ab} + \frac{(1-\upsilon)m^2 n^2 \pi^4}{2ab}] \cdot DW_{mn}$$

$$+ \sum_{y_s} \sum_{j=1}^{j=N} \left[ \frac{m^4\pi^4}{2a^3} EI_{ex} \sin(\frac{\pi n y_s}{b}) \sin(\frac{\pi j y_s}{b}) + \frac{m^2 n j \pi^4}{2ab^2} GJ_x \cos(\frac{n\pi y_s}{b}) \cos(\frac{j\pi y_s}{b}) \right] \cdot W_{mj}$$

$$+ \sum_{x_s} \sum_{i=1}^{i=M} \left[ \frac{n^4\pi^4}{2b^3} EI_{ey} \sin(\frac{m\pi x_s}{a}) \sin(\frac{i\pi x_s}{a}) + \frac{mn^2 i \pi^4}{2a^2 b} GJ_y \cos(\frac{m\pi x_s}{a}) \cos(\frac{i\pi x_s}{a}) \right] \cdot W_{in} \qquad (5.23)$$

$$+ \sum_{y_s} \sum_{i}^{M} \sum_{j}^{N} (h_{sx} + h_p) EA_{sx} \frac{im^3\pi^2}{a^2(m^2 - i^2)} \sin(\frac{j\pi y_s}{b}) \sin(\frac{n\pi y_s}{b}) A_{ij}$$

$$\sum_{x_s} \sum_{i}^{M} \sum_{j}^{N} (h_{sy} + h_p) EA_{sy} \frac{jn^3\pi^2}{b^2(n^2 - j^2)} \sin(\frac{i\pi x_s}{a}) \sin(\frac{m\pi x_s}{a}) B_{ij}$$

$$= \frac{\partial V}{\partial W_{mn}} = \frac{ab}{4} P_{mn}$$

Then taking the derivative of the total potential energy with respect to $A_{mn}$, the second set of $M \times N$ equations are calculated as:

$$\frac{\partial U_p + \partial U_s}{\partial A_{mn}} = [\frac{Cm^2\pi^2 b}{4a} + \frac{C(1-v)n^2\pi^2 a}{8b}] \cdot A_{mn} + \sum_i \sum_j \frac{2mnijC(1+v)}{(m^2 - i^2)(j^2 - n^2)} B_{ij}$$

$$+ \sum_{y_s} \sum_{j=1}^{j=N} \frac{m^2\pi^2}{2a} EA_{sx} \sin(\frac{n\pi y_s}{b}) \sin(\frac{j\pi y_s}{b}) A_{mj} \qquad (5.24)$$

$$+ \sum_{y_s} \sum_{i=1}^{M} \sum_{j=1}^{N} (h_{sx} + h_p) EA_{sx} \frac{mi^3\pi^2}{a^2(i^2 - m^2)} \sin(\frac{n\pi y_s}{b}) \sin(\frac{j\pi y_s}{b}) W_{ij}$$

$$= 0$$

Finally taking the derivative of the potential energy with respect to $B_{mn}$, the third set of $M \times N$ equations are calculated as:

$$\frac{\partial U_p + \partial U_s}{\partial B_{mn}} = [\frac{Cn^2\pi^2 a}{4b} + \frac{C(1-v)m^2\pi^2 b}{8a}] \cdot B_{mn} + \sum_i \sum_j \frac{2mnijC(1+v)}{(m^2 - i^2)(j^2 - n^2)} A_{ij}$$

$$+ \sum_{x_s} \sum_{i=1}^{i=M} \frac{n^2\pi^2}{2b} EA_{sy} \sin(\frac{m\pi x_s}{a}) \sin(\frac{i\pi x_s}{a}) B_{in} \qquad (5.25)$$

$$+ \sum_{x_s} \sum_{i=1}^{M} \sum_{j=1}^{N} (h_{sy} + h_p) EA_{sy} \frac{nj^3\pi^2}{b^2(j^2 - n^2)} \sin(\frac{m\pi x_s}{a}) \sin(\frac{i\pi x_s}{a}) W_{ij}$$

$$= 0$$

Re-writing the expressions of Eqn. (5.23) to Eqn. (5.25) in the form of linear operations:

$$[E_{1_{mn}}]\{W_{mn}\} + \sum_{y_s}[E_{2_{mn}}]\{W_{mn}\} + \sum_{x_s}[E_{3_{mn}}]\{W_{mn}\} + \sum_{y_s}[E_{4_{mn}}]\{A_{mn}\} + \sum_{x_s}[E_{5_{mn}}]\{B_{mn}\} = [E_{mn}]\{P_{mn}\} \ (5.26)$$

$$[CX_{1_{mn}}]\{A_{mn}\}+[CX_{2_{mn}}]\{B_{mn}\}+\sum_{y_s}([CX_{3_{mn}}]_s\{A_{mn}\}+[CX_{4_{mn}}]_s\{W_{mn}\})=\{\mathbf{0}\} \tag{5.27}$$

$$[CY_{1_{mn}}]\{B_{mn}\}+[CY_{2_{mn}}]\{A_{mn}\}+\sum_{x_s}([CY_{3_{mn}}]_s\{B_{mn}\}+[CY_{4_{mn}}]_s\{W_{mn}\})=\{\mathbf{0}\} \tag{5.28}$$

Here $\{W_{mn}\}$, $\{A_{mn}\}$ and $\{B_{mn}\}$ are the $(M \times N)$ $by$ $1$ vector for Fourier coefficients of the displacement field for $m = 1..M, n = 1..N$, as the following:

$$\{W_{mn}\} = [W_{11}\ W_{12}\ ..\ W_{1N}\ W_{21}..\ W_{2N}\ ...\ W_{M1}..\ W_{MN}]^T \tag{5.29}$$

$$\{A_{mn}\} = [A_{11}\ A_{12}\ ..\ A_{1N}\ A_{21}..\ A_{2N}\ ...\ A_{M1}..\ A_{MN}]^T \tag{5.30}$$

$$\{B_{mn}\} = [B_{11}\ B_{12}\ ..\ B_{1N}\ B_{21}..\ B_{2N}\ ...\ B_{M1}..\ B_{MN}]^T \tag{5.31}$$

$[E_{1mn}]$, $[E_{2mn}]_s$, $[E_{3mn}]_s$, $[E_{4mn}]_s$ and $[E_{5mn}]_s$ are the $(M \times N)$ by $(M \times N)$ coefficient matrices that are derived from the minimum total potential energy of the whole plate with respect to the coefficient vector $\{W_{mn}\}$. Also, $[CX_{1mn}]$ through $[CX_{4mn}]$ are the $(M \times N)$ by $(M \times N)$ coefficient matrices that are derived from the minimum total potential energy of the entire plate with respect to the coefficient vector $\{A_{mn}\}$, while $[CY_{1mn}]$ through $[CY_{4mn}]$ are the coefficient matrices that are derived with respect to the coefficient vector $\{B_{mn}\}$. The detailed expression for the coefficient matrices are provided in the appendices. The results are discussed in the following section with comparison to the FEA model.

## 5.3    Sample Calculation Results

### 5.3.1 DEM I vs Numerical Results

To evaluate the accuracy and efficiency of the DEM methods, the structural response is analyzed for two simply supported stiffened panels (Fig. 5.1a). Three horizontal stiffeners are

distributed evenly over the plate, spanning across the x-direction with thickness of 12 mm and height of 140 mm. For the second model, one additional orthogonal stiffener is added along the middle of the plate (Fig. 5.1b). The dimension of the plate is 2000 mm by 2000 mm with thickness of 20 mm. Four edges are simply supported at the calculated effective centroids, i.e., simply supported along the mid-plane of the plate for the x-direction edges, and simply supported at $z_x = 21.5\ mm$ for the y-direction edges (Fig. 5.2). The geometry is selected with respect to a commonly observed thickness-to-length ratio of 1/100 for stiffened thin plates in offshore or naval structures (Mouritz et al., 2001). The assigned pressure is 0.1MPa to be within the range of elastic deformation for the sample stiffened steel plate analysis. The 'incompatible' modes for 3D solid elements C3D8I are applied for FEA analysis, with four element layers over the thickness of the plate to accurately capture the bending effect while eliminating the shear locking phenomena. The 'incompatible' modes for the quadrilateral and hexahedral elements are elements fully integrated with internal degrees of freedom added. Additionally, the FEA model avoids artificial stiffening due to Poisson's effect in bending deformation. The plate with three horizontal stiffeners is first evaluated using DEM I.

The transverse displacement field w(x,y) calculated by DEM I is shown contoured in Fig. 5.3 with satisfying agreement with the FEA model of pinned ends at the effective centroids. The transverse and in-plane displacements calculated by DEM I at the mid-plane of the plate along x=1000 mm or along y=1250 mm are compared with the FEA results (Fig. 5.4a-5.4d). It is observed that DEM I gives good approximation of the transverse displacement fields both along the mid-line of the plate or in between stiffeners at an approximate accuracy of 90% (Fig. 5.4a and Fig. 5.4b). However, DEM I assumes the plane cross-sections remain plane and calculates the in-plane displacement fields from the rotation from the bending effect with respect to the neutral

planes. Fig. 5.4c represents an averaged x-direction displacement $u(x, y)$ calculated from the rotation of the plate about the y-axis. The displacement field $v(x, y)$ is calculated as zero at the mid-plane of the plate as is shown in Fig. 5.4d. DEM I cannot capture the v-component in-plane displacement at the mid-plane which is actually non-zero because of the Poisson's effect from the bending of the plate about the y-axis.

Calculated stresses and strains are shown in Fig. 5.5 and Fig. 5.6. The calculated horizontal strains $\varepsilon_{xx}$ have smeared values of the plate and stiffeners as shown in Fig. 5.5a. The calculated stresses $\tau_{xx}$ match well the results from FEA, particularly capturing the curvatures at the stiffeners (Fig. 5.5b). The in-plane strains $\varepsilon_{yy}$ calculated by DEM I agree well with the FEA results for the wavy deformation over stiffeners on top and bottom of the plate. However, the strains in the middle of the plate with no y-direction stiffeners yield zero strain value as is shown in Fig. 5.6a. Similarly, the stresses $\tau_{yy}$ calculated by DEM I give satisfying approximation for top and bottom of the plate with a minimum accuracy of about 85% (Fig. 5.6b).

To evaluate the maximum stress over the stiffeners as one of the key issues for design and strength analysis, the horizontal stresses $\tau_{xx}$ calculated are plotted with what is obtained from the FEA model (Fig. 5.7). The DEM I model gives close approximation for the stresses for both the top of the plate and the bottom of the stiffener, while the stress at the effective centroids by DEM I goes to zero. Note that the stress for the plate is calculated from displacement derivatives using the effective Young's modulus based on plane strain assumption, while the stress at the bottom of the stiffener is calculated using beam theory and steel's Young's modulus.
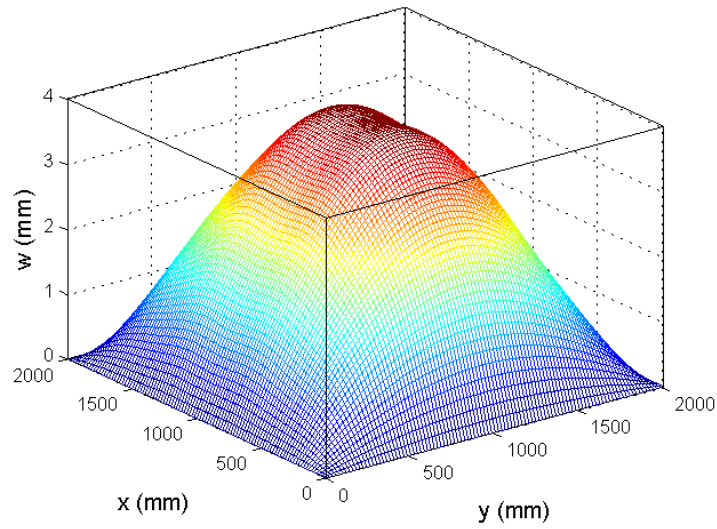
**Figure 5.3:** Transverse displacement field w(x,y) calculated from DEM I at order of M=N=11



(a)



(b)



(c)



(d)
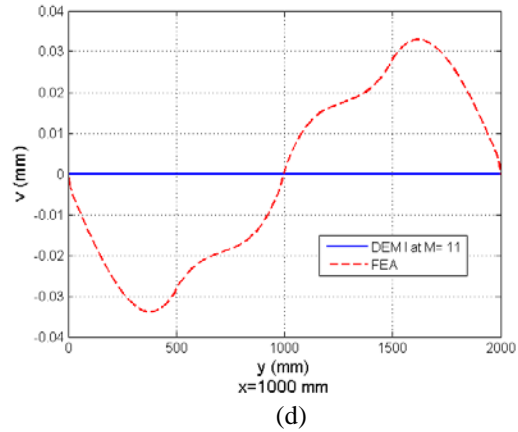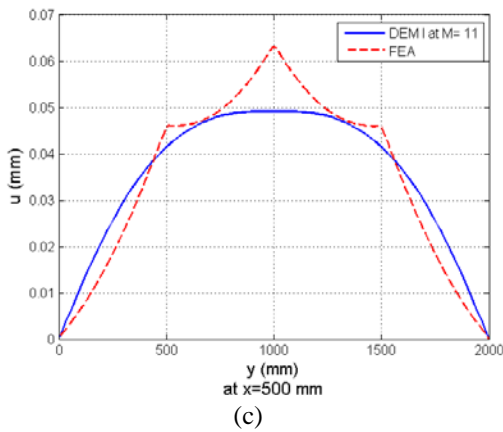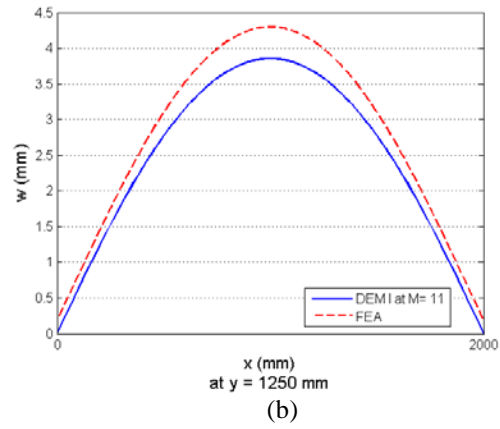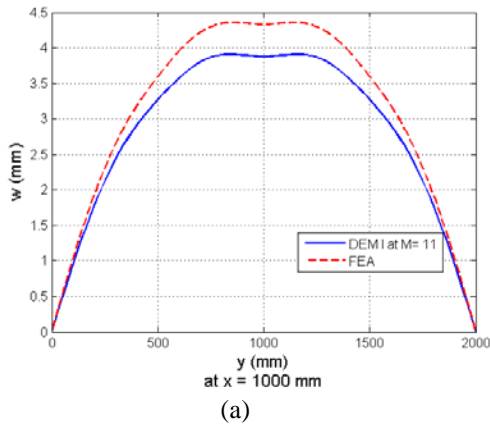
**Figure 5.4: (a)** Displacement w(x,y,z=0) at x=1000 mm, **(b)** w(x,y,z=0) at y=1250 mm, **(c)** u(x,y,z=0) at x=500 mm, **(d)** v(x,y,z=0) at x=1000 mm by DEM I
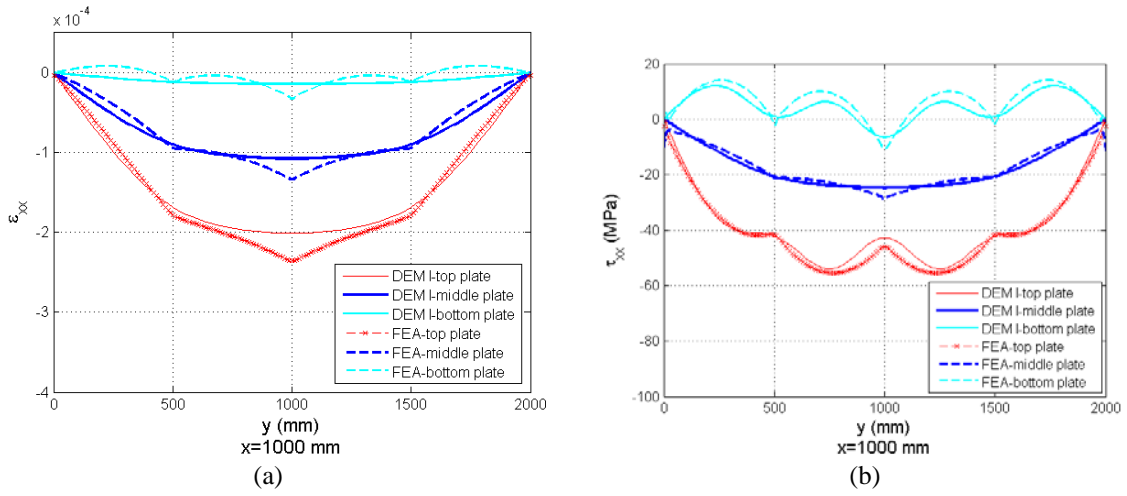
**Figure 5.5:** (**a**) Strain $\varepsilon_{xx}$ and (**b**) stress $\tau_{xx}$ at x=1000 mm at top, middle and bottom of plate by DEM I compared to FEA results
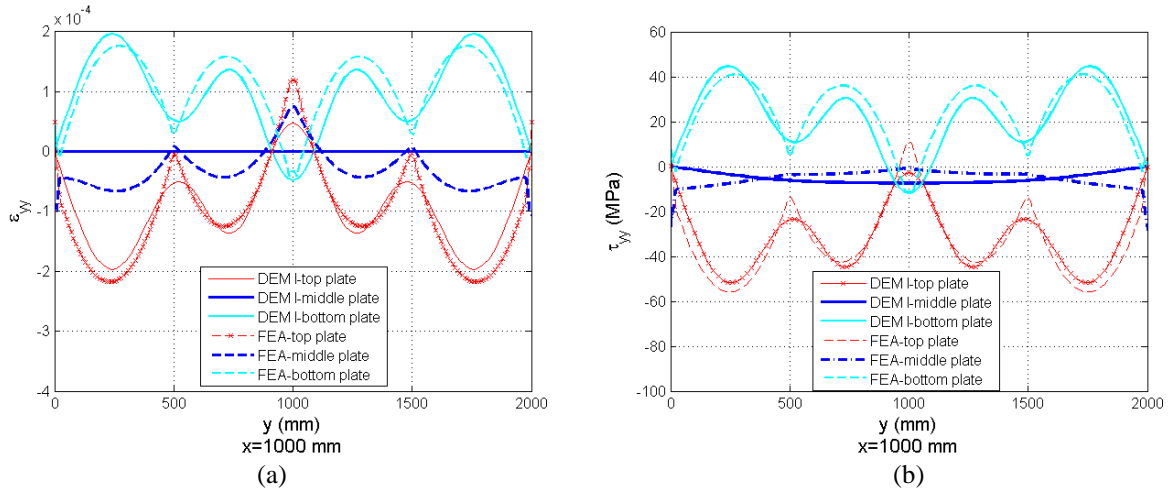


**Figure 5.6:** (**a**) Strain $\epsilon_{yy}$ and (**b**) stress $\tau_{yy}$ at x=1000 mm at top, middle and bottom of the plate by DEM I compared to FEA results
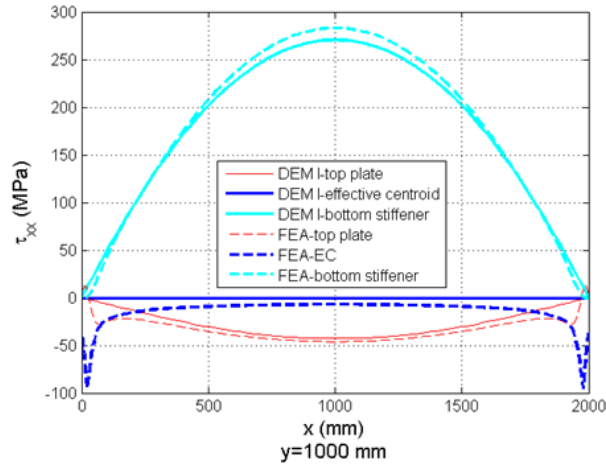
**Figure 5.7:** Stress $\tau_{xx}$ in the middle stiffener of the plate (at y=1000 mm) by DEM I compared to FEA results

### 5.3.2 DEM II vs Numerical Results

The FEA model for comparison with DEM II results has the same geometry as the model for DEM I, and the loading pressure is again 0.1 MPa over the entire plate. The boundary conditions for the FEA model are updated as pinned edges along the mid-plane at its four edges. This boundary condition allows a direct comparison of FEA model to the DEM II.

The transverse displacement contour from DEM II is plotted in Fig. 5.8. The maximum transverse displacement predicted by DEM II is improved compared to DEM I, with the displacement closely capturing the FEA results from the boundary edges to the middle part of the plate (Fig. 5.9a and Fig. 5.9b). The highlight using DEM II lies in its capability to accurately formulate the in-plane displacement to capture the in-plane shear and Poisson's effects. The displacements $u(x, y, z = 0)$ and $v(x, y, z = 0)$ are plotted in Fig. 5.9c and Fig. 5.9d in solid lines agreeing well with the dashed lines obtained from the FEA results at an accuracy of over 90%.

The horizontal strains $\varepsilon_{xx}$ and stresses $\tau_{xx}$ predicted by DEM II overcome the deficiency of zero v-component strain value predicted at the neutral plane by DEM I. Both strains and stresses

calculated by DEM II match very well the FEA results as are shown in Fig. 5.10a and Fig. 5.10b. The maximum horizontal strains $\varepsilon_{xx}$ and stresses $\tau_{xx}$ achieve an accuracy of over 95% approximated by DEM II, while there is approximate 85% accuracy using DEM I. Additionally, the strains $\varepsilon_{yy}$ and stresses $\tau_{yy}$ achieve substantial improvement of accuracy calculated using DEM II (Fig. 5.11a and Fig. 5.11b). The DEM II well reflects the in-plane displacements at the middle of the plate thus resolving the smearing effect issue observed in the DEM I method.

Finally, the stresses $\tau_{xx}$ calculated by DEM II are evaluated against the results obtained by FEA shown in Fig. 5.12. The stress at the top of the plate predicted by DEM II matches nicely with that analyzed in FEA. Excellent agreement of the maximum stress predicted by DEM II at the bottom of the stiffener is achieved compared to the stress obtained from the corresponding FEA model. The DEM II method shows accurate approximations for both the stress over the plate and the maximum stress at the tip of the stiffener. It is found that that the DEM II captures the structural response and the stress components with improved accuracy for the stiffened structures.
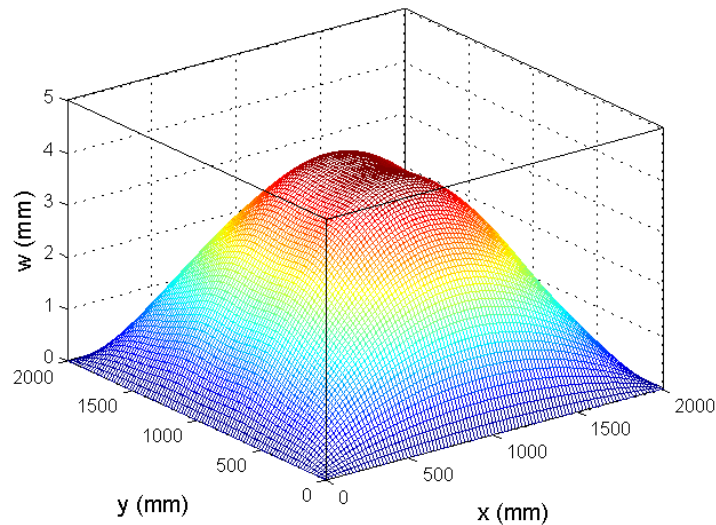


**Figure 5.8:** Transverse displacement field w(x,y,z=0) calculated by DEM II at order of M=N=11
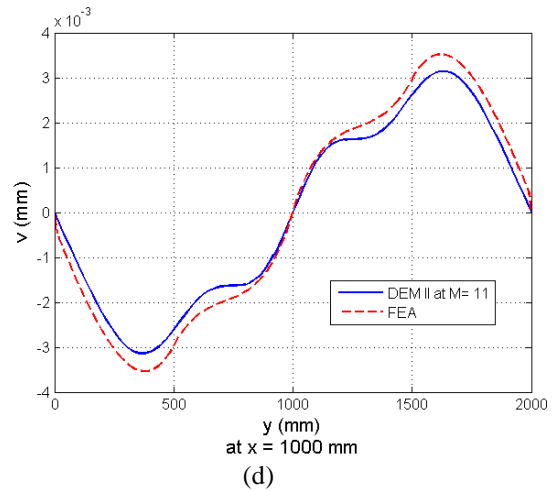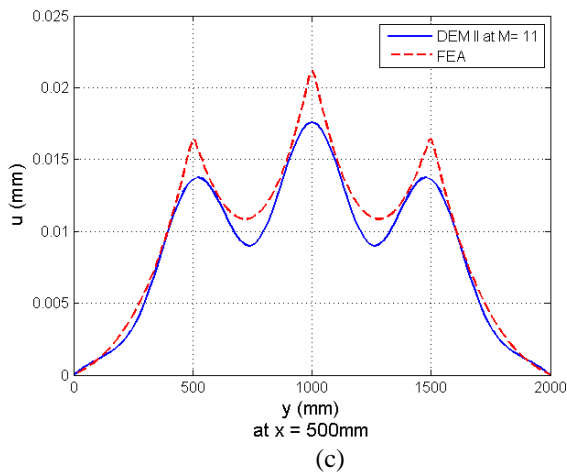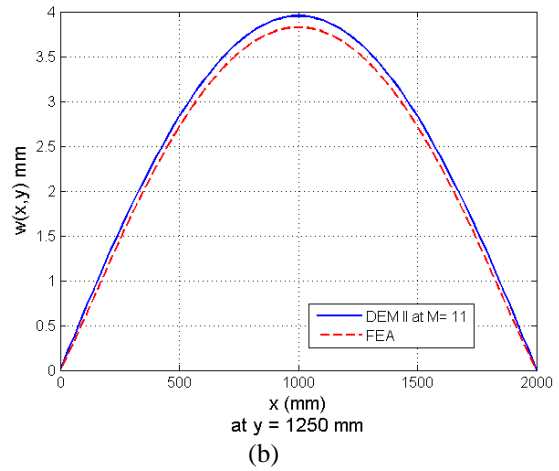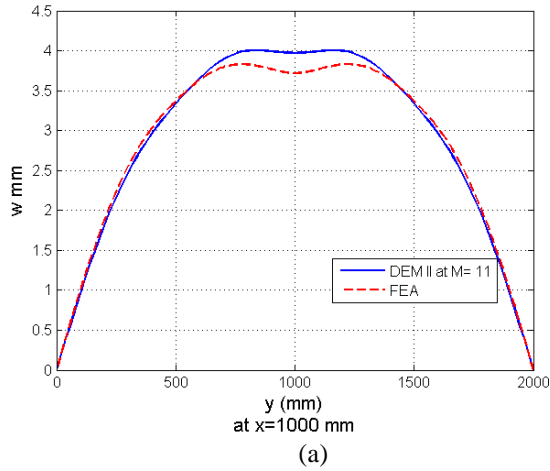
**Figure 5.9: (a)** Displacement w(x,y,z=0) at x=1000 mm; **(b)** w(x,y,z=0) at y=1250 mm; **(c)** u(x,y,z=0) at x=500 mm; **(d)** v(x,y,z=0) at x=1000 mm by DEM II
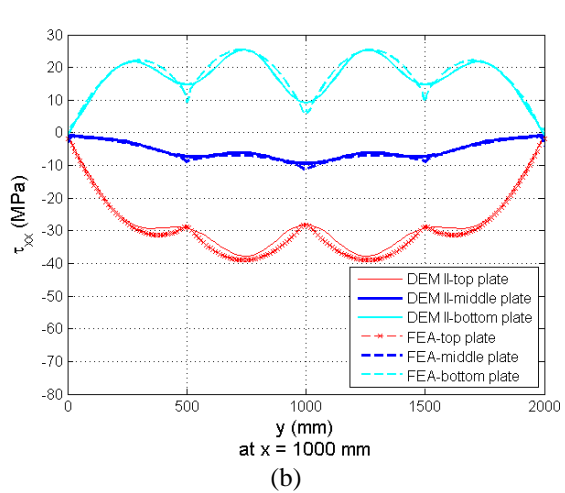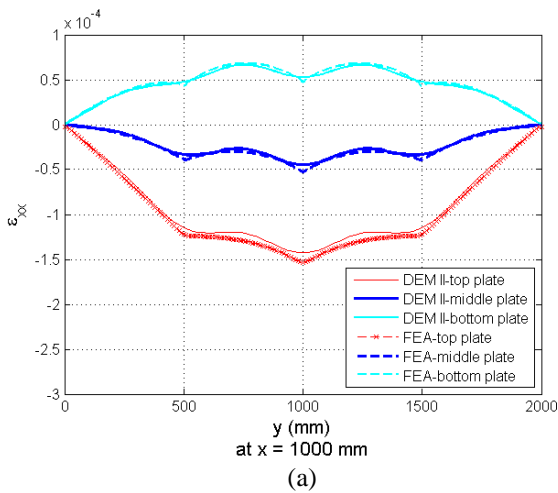


**Figure 5.10: (a)** Strain $\varepsilon_{xx}$ and; **(b)** stress $\tau_{xx}$ at x=1000 mm the at top, middle and bottom of plate by DEM II compared to FEA results
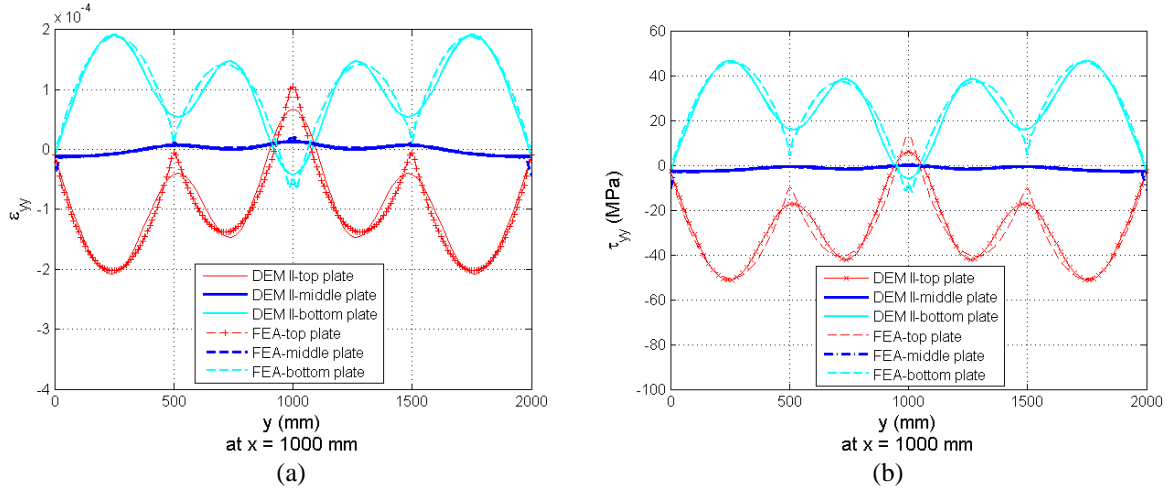
**Figure 5.11:** (**a**) Strain $\varepsilon_{yy}$ and (**b**) stress $\tau_{yy}$ at x=1000 mm at top, middle and bottom of plate by DEM II compared to FEA results
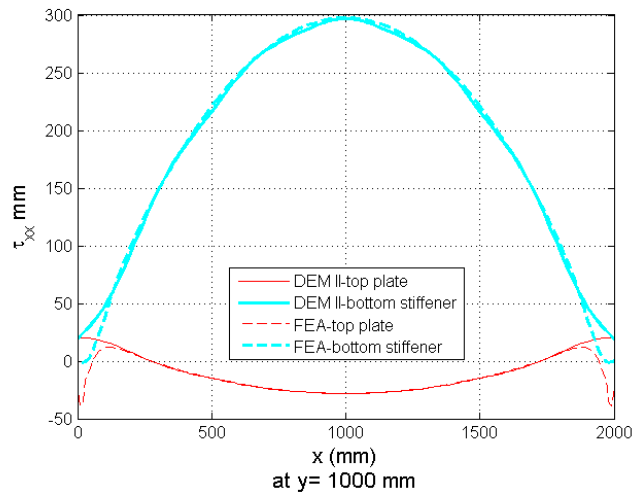


**Figure 5.12:** Stress $\tau\_xx$ in the middle stiffener of the plate (at y=1000 mm) by DEM II compared to FEA results

### 5.3.3 Orthogonally Stiffened Plate using DEM I and DEM II vs FEA results

The geometry of the orthogonally stiffened plate is sketched in Fig. 5.1b. This orthogonally stiffened panel is evaluated again using both DEM I and DEM II to compare with the FEA results in terms of the structural response. The transverse and in-plane displacements calculated by DEM I match with FEA's results to approximately 75% to 86% as are shown in Fig. 5.13b-5.13f. The

87

transverse displacement caused by the dominant bending effect agree well with the FEA model compared to the in-plane displacement calculated by DEM I (Fig. 5.13b-f). It is observed that the plate with only three horizontal stiffeners predict better the displacement fields compared to the orthogonally stiffened plate as the Poisson's effect is less dominant in uniformly-stiffened direction (Fig. 5.4 and Fig. 5.13). Further evaluation of the stresses $\tau_{xx}$ and $\tau_{yy}$ over the plate calculated by DEM I for the orthogonal plate are compared with the FEA results (Fig 5.14). The stress approximation by DEM I gives a smearing effect over the aligned stiffeners as shown in Fig. 5.14. Note that DEM I gives good approximation of maximum stress $\tau_{xx}$ along the tip of the stiffener (Fig. 5.15) at similar accuracy as the uniformly stiffened panel approximately 90%.

Compared to DEM I, DEM II presents a marked improvement in the calculation of displacement fields and the stress analysis as depicted in Fig.5.16-5.18. The in-plane displacements calculated by DEM II satisfyingly describe the variation of the displacements between stiffeners (Fig. 5.16). The accurate prediction of displacement contributes to a more accurate calculation of in-plane stress over the plate as is shown in Fig. 5.17. It is also worth noting that the maximum stresses calculated by DEM II over the tip of the stiffener very accurately agree with that analyzed by more elaborate FEA model compared to DEM I method (Fig. 5.18 and Fig. 5.15). This highlights the advantage of DEM II method in formulating the $u_0(x, y)$ and $v_0(x, y)$ at the mid-plane of the plate to capture the in-plane effects of various stiffened structure which is neglected by DEM I.

(a)

(b)

(c)

(d)

(e)

(f)
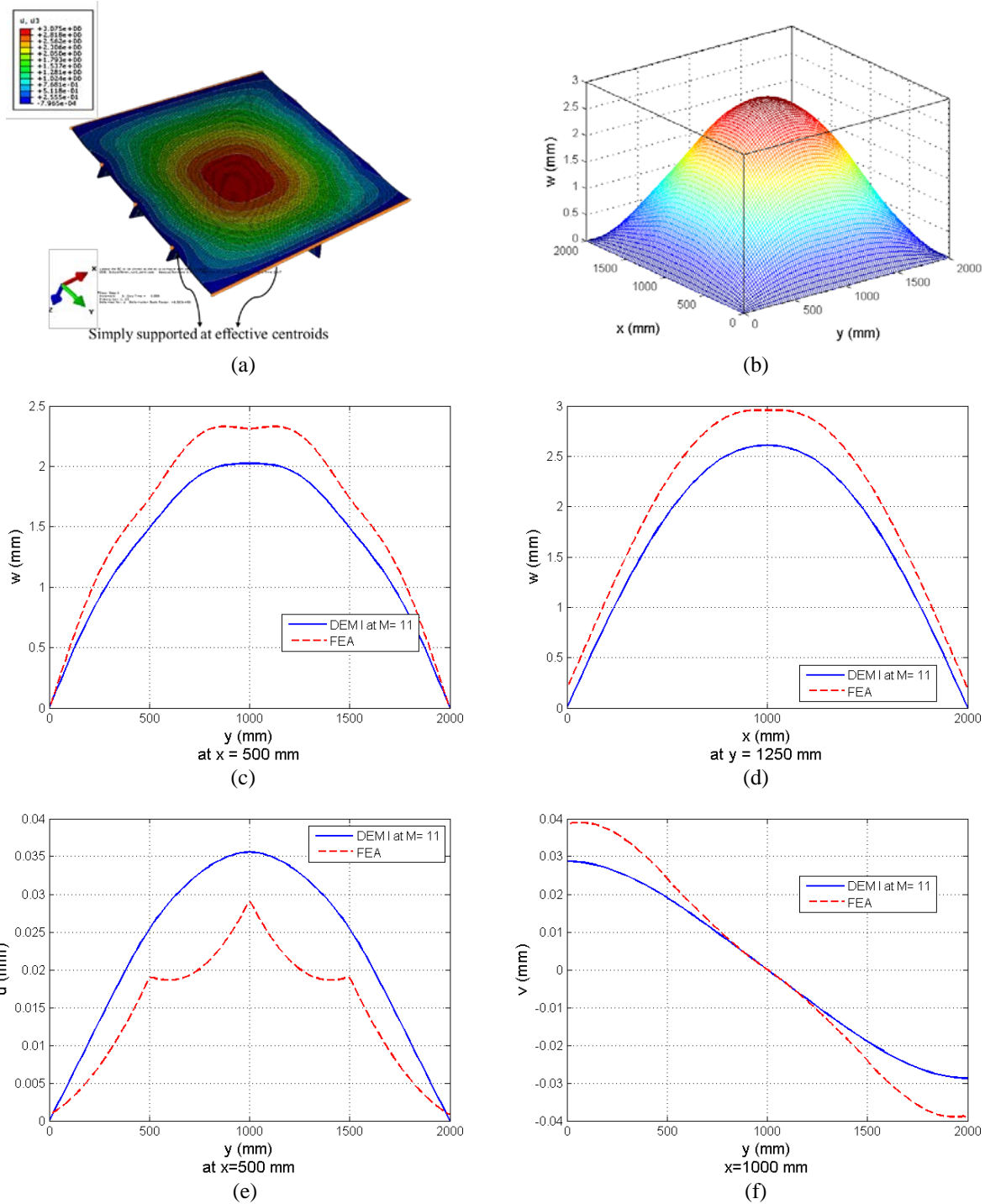
**Figure 5.13:** **(a)** Transverse displacement w(x,y,z) contour by FEA; **(b)** w(x,y,z=0) contour calculated by DEM I at order of M=N=11; **(c)** Displacement w(x,y,z=0) at x=1000 mm; **(d)** w(x,y,z=0) at y=1250 mm; **(e)** u(x,y,z=0) at x=500 mm; **(f)** v(x,y,z=0) at x=1000 mm by DEM I
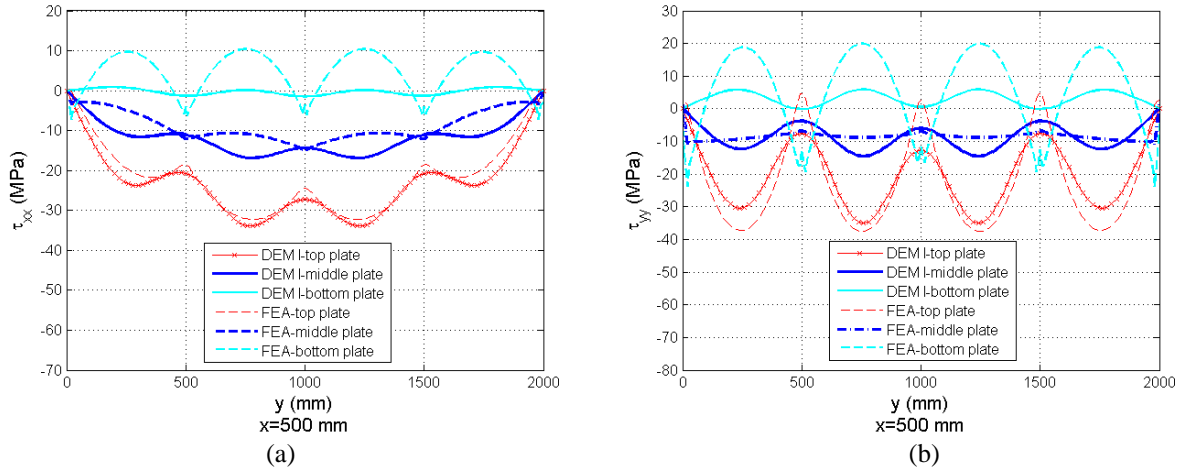
**Figure 5.14:** Stress $\tau_{xx}$ (**a**) and $\tau_{yy}$ (**b**) comparison using DEM I vs FEA results for orthogonally stiffened plate
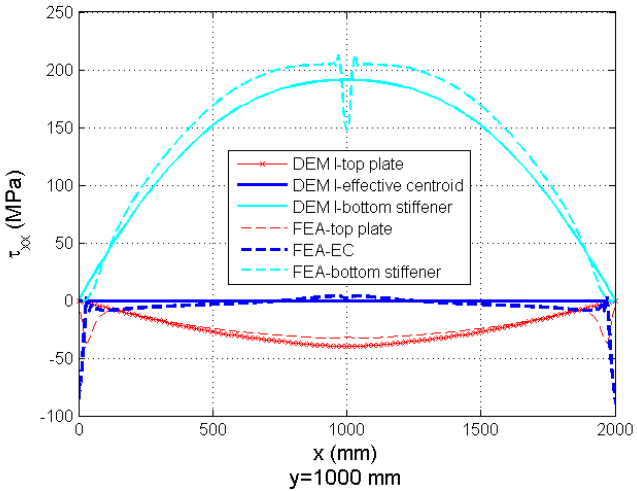


**Figure 5.15:** Horizontal stress $\tau_{xx}$ by DEM I vs FEA results for orthogonally stiffened plate at y=1000 mm
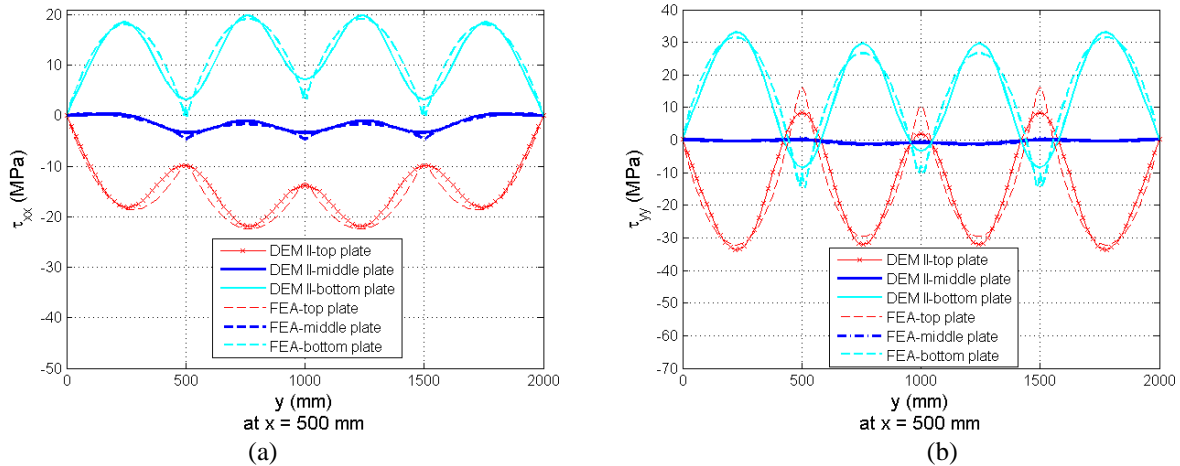


**Figure 5.16:** Stress $\tau_{xx}$ (**a**) and $\tau_{yy}$ (**b**) comparison using DEM II vs FEA results for orthogonally stiffened plate

90
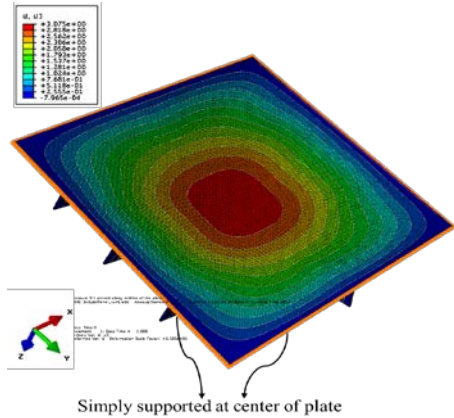
(a)
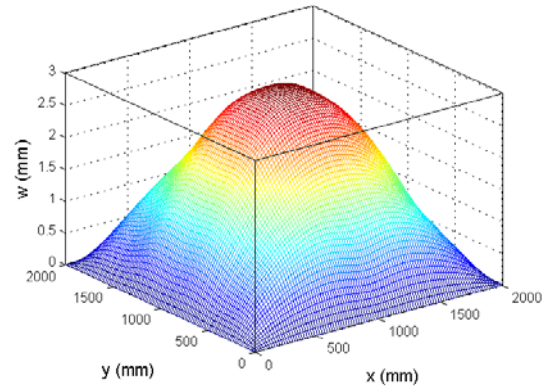
(b)
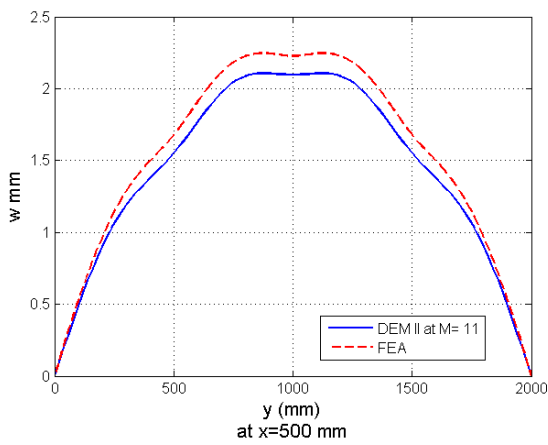
(c)
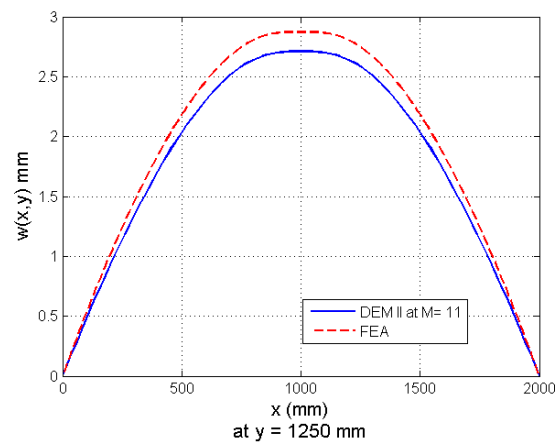
(d)
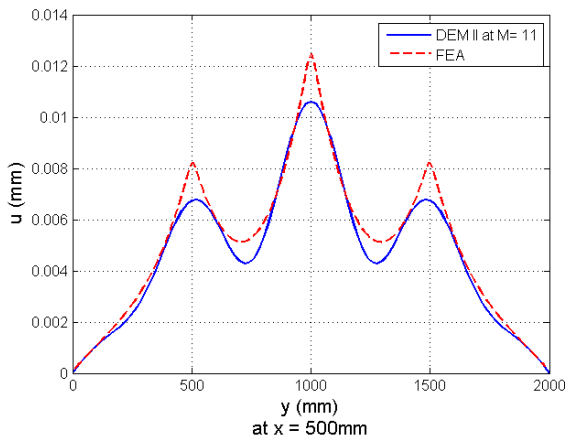
(e)
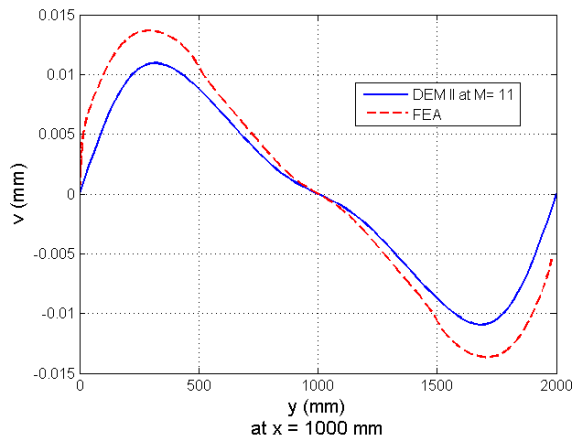
(f)

**Figure 5.17: (a)** Transverse displacement w(x,y,z) contour by FEA; **(b)** w(x,y,z=0) contour calculated by DEM II at order of M=N=11; **(c)** Displacement w(x,y,z=0) at x=1000 mm; **(d)** w(x,y,z=0) at y=1250 mm; **(e)** u(x,y,z=0) at x=500 mm; **(f)** v(x,y,z=0) at x=1000 mm by DEM II
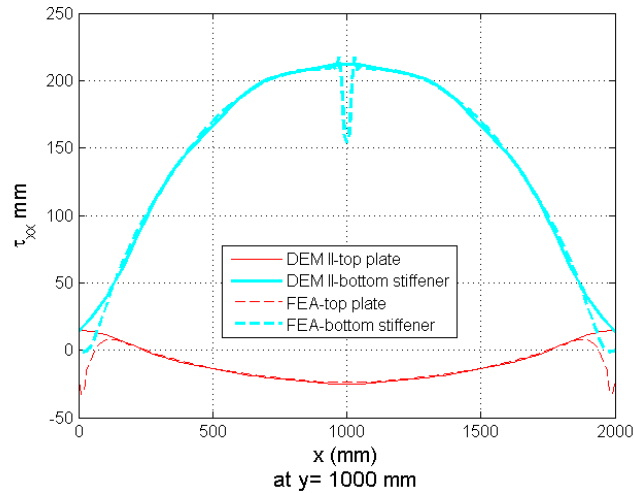
**Figure 5.18:** Horizontal stress $\tau_{xx}$ by DEM II vs FEA results for orthogonally stiffened plate at y=1000 mm

## 5.4    Conclusions

Two sub-models DEMI and DEM II are developed to predict the response of various stiffened plates applying the discrete energy component method using Fourier series formulation with two different assumptions of the neutral planes. DEM I presumes that the reference planes having zero in-plane displacements at the effective centroids calculated from the cross-section intervals for either x-direction or y-direction aligned stiffeners. DEM II formulates non-zero in-plane displacement fields at the mid-plane of the plate, thus saving the calculation effort for effective centroids and the effective breadths. The plate described above is simply supported on all four edges at the effective centroids for DEM I model, and at the mid-plane of the plate for DEM II model. This simply supported boundary condition is assumed as practical for efficient ship structural and stiffened plate design in general.

DEM I is valid and efficient assuming the dominance of bending effect for plate with pinned ends. It is found that DEM I approximate approximately 90% of the maximum stress over

the stiffener compared for different stiffening patterns, indicating the dominance of the bending effect for the stiffened plate in the middle section of the structure.

DEM II formulates the in-plane displacement field $u_0(x, y)$ and $v_0(x, y)$ at the mid-plane of the plate, thus more accurately considering the in-plane shearing Poisson's effects compared to the DEM I method. Additionally, DEM II eliminates the need to calculate the effective centroids for the stiffened cross section to achieve great calculation efficiency with the improvement of accuracy for stress and strain evaluation over the entire panel. It is observed that DEM II also improves the accuracy in prediction of the transverse displacement field $w(x, y)$ compared to DEM I. Additionally, DEM II catches the displacement variation between stiffeners while the stiffness is smeared using DEM I. The capture of these deformation variations between stiffeners is critical to understand the maximum stress and strength for the plate analysis for design purposes.

Finally, DEM II presents notable accuracy in prediction in either uni-directionally or orthogonally stiffened plate for its stress evaluation. The advantage of formulating the in-plane displacement highlights the accuracy and cost-saving efficiency of DEM II in terms of design evaluation compared to traditional computationally expensive FEA model analysis and less accurate conventional orthotropic plate theory.

Chapter 6

## Conclusion

## 6.1    Conclusions

In this thesis, motivated to further study the ice-structure interaction process and to more efficiently predict peak ice loading during multiple ice failure modes coupled with other environmental and undetermined factors, I developed multiple inverse ice loading prediction algorithms for stiffened plates. The inverse ice load prediction models incorporated the field measured data to record the peak ice loading in the Great Lakes area in Lake Superior through year 2014 to 2015. Extended effort is given to predict the peak motion of amplitude for the dynamic ice-structure interaction modeled by Matlocks's model of ice-teeth indentation against a spring-mass-dashpot system using Fourier series analysis to simulate the continuous ice crushing. As an improvement on the structural analysis part incorporated in the inverse ice-load prediction algorithm, a novel analytical model using discrete energy method is established for structural analysis of stiffened plate with substantial efficiency and accuracy.

The inverse of the horizontal SBT is beneficial as an initial estimation of the averaged ice forcing when the number of structural inputs is extremely limited; the inverse of the vertical SBT

provides a close estimation for contact ice-forcing between the ribs given the availability of vertical strain measurements. The OPIT I is always recommended for its accuracy to extract the variable ice-forcing when several strain measurements are available and the ice thickness measurement is not available. The OPIT II is notably efficient in approximating the amplitude of contact ice forcing, if the ice thickness measurement for the span of the ice-contact area is available. Finally, the combination of both OPIT I and OPIT II is encouraged: first to get an evaluation of the distribution of the ice forcing over the entire plate, then to obtain more acute contact ice force amplitudes if the ice thickness measurements are available.

The variable loading caused by the coupled effect of ice, wind and thermal forcing has been analyzed using the strain measurements recorded by the IFMS instrumentation through the winter season 2013-2014. Maximum pressure forcing of 3.54 MPa is observed on May 01 by OPIT II calculation, while a peak average pressure about 0.90 MPa to 1.30 MPa were found based on the strain measurements on April 17 and March 18, 2014.

In the non-linear ice-structure dynamic simulation using Matlock's model, the presented approach establishes the non-linear dynamic equations through Fourier analysis with respect to the number of tooth-breakages $N$ per cycle. This method allows rapid estimation for the range of motion and the evaluation of structural contact forces. Furthermore, the time ratios of breakage are accurately predicted given a representative ice-structure interaction system applying first modal analysis, thus the cyclic behavior is analyzed accordingly.

As for the stiffened plate analysis, DEM II presents a marked improvement in the calculation of displacement fields and the stress analysis compared to DEM I. The accurate prediction of displacement contributes to a more accurate calculation of in-plane stress over the

plate by DEM II incorporating the shear effect at the mid-plane of the plate. Another highlight of the advantages of DEM II method lie in its formulation of the $u_0(x, y)$ and $v_0(x, y)$ at the mid-plane of the plate to capture the in-plane effects of various stiffened structure which is neglected by DEM I.

## 6.2    Future Research Directions

### 6.2.1 Inverse Ice Load Prediction

Further experimental research can be proposed to use the existing hardware from the DoE project of the ice force measurement panel and extend its usage in the Lake St. Clair, Detroit River system. The core aspect of the presented dissertation is the mechanical modeling of the ice-structure interaction.

- The field experimentation can focus on collecting strain gage data both at low and high strain rates to validate the inverse ice-load prediction algorithm and record the peak floe ice loads at various ice failure conditions incorporating the recorded weather conditions as the input parameters for ice condition description.

- The calculated peak ice loads compare to the loads calculated using the existing design codes and follow a similar fashion as Sabodash's (2015) calculation on the ice loads on the Sakhalin offshore structure using a statistical modeling for level ice fields.

- The key factor of impact ice load can thus be recorded and the results can be compared with existing ice-impact load. The relationship of the ice thickness, ice-

indentation speed and the temperature with respect to the peak ice loads calculated using the inverse ice prediction method can be recorded and compared to the design loads (Kim and Amdahl, 2016; Jiang et al, 2016).

- The inverse algorithm can be improved using DEM I or DEM II method for the forward formulation of structural response of stiffened plate, while the optimized order can be studied, thus new installation of strain gages can be recommended before field installation to maximize the accuracy under limited input.

- The TSVE can also be improved using other widely applied optimization methods to realize the automation of reduced order inverse load prediction at in-situ dynamic condition (Ward et al., 2018)

## 6.2.2 Proposed Validation of Matlock's Model for Ice-crushing Analysis

Unlike the forward mathematical solution, the kinematic initial conditions and the response amplitude of the wind turbine structure can be predicted at targeted periodicity using the Matlock's model via the Fourier analysis. Given a representative offshore wind tower system:

- The first mode shape of the physical system is calculated as input for the ice-structure interaction model (Huang and Song, 2007; Ziemer and Evers, 2016)

- The results can be compared with other validly established ice-structure interaction model with existing experimental records (Kärnä and Turunen, 1989; Sodhi, 2001; Huang and Liu, 2009; Ji and Oterkus, 2016)

- Further effort should be given to validate the basin of attractions given a representative system and more specific evaluation of the error range in the velocity predictions due to the Gibbs effects (Hewitt and Hewitt, 1979; Jerri, 2013)

## 6.2.3 Stiffened Plate Analysis

The stiffened plate analysis can be developed into a design package and extended applications to better understand the structural behavior of stiffened plate:

- The stiffened plate analysis using DEM I and DEM II can be well developed into students' ship design tool for stiffened plate scantling without the knowledge of FEA for model set-up.
- The FEA modeling for swaged panel analysis as equivalent composite plate is to be further studied as an extended understanding for stiffened plate analysis in marine structures (Karr and Ashcroft, 2015). Similar approaches of the DEM methods might as well to be applied to model the swaged panel as stiffened plates to increase the accuracy and efficiency of structural design.

## Appendix A Coefficient Matrix for DEM I and DEM II

DEM I – Coefficient Matrice Operation

$[A_{o\,mn}]$ are $(M \times N)$ by $(M \times N)$ diagonal coefficient matrice at the $m_{th}$ and $n_{th}$ order as the following:

$$[A_{o_{mn}}]_s = \begin{bmatrix} A_{11} & & & & & & & & \\ & A_{1n} & & & & & & & \\ & & A_{1N} & & & & & & \\ & & & A_{m1} & & & & & \\ & & & & .. & & & & \\ & & & & & A_{mN} & & & \\ & & & & & & A_{M1} & & \\ & & & & & & & A_{Mn} & \\ & & & & & & & & A_{MN} \end{bmatrix} \tag{A.1}$$

$[B_{o\,mn}]_s$ are $(M \times N)$ by $(M \times N)$ matrices with coupled terms at the $m_{th}$ and $n_{th}$ order as an effect of x-stiffeners evenly distributed at $y = y_s$s over depth of the plate:

$$[B_{o_{mn}}]_s = \begin{bmatrix} B_{11\_1} & . & B_{11\_N} \\ B_{1n\_1} & . & B_{1n\_N} \\ B_{1N\_1} & . & B_{1N\_N} \\ & & & . & . & . \\ & & & . & . & . \\ & & & . & . & . \\ & & & & & & B_{M1\_1} & . & B_{M1\_N} \\ & & & & & & B_{Mn\_1} & . & B_{Mn\_N} \\ & & & & & & B_{MN\_1} & . & B_{MN\_N} \end{bmatrix} \tag{A.2}$$

Note that $[Co_{mn}]_s$ are $M \times N$ by $M \times N$ matrices as an effect of evenly distributed y-stiffeners at

$x = x_s$s over the plate:

$$[C_{o_{mn}}]_s = \begin{bmatrix} C_{11\_1} & & & C_{11\_m} & & & C_{11\_M} \\ & C_{1n\_1} & & & C_{1n\_m} & & & C_{1n\_M} \\ & & C_{1N\_1} & & & C_{1N\_m} & & & C_{1N\_M} \\ C_{m1\_1} & & & C_{m1\_m} & & & . \\ & C_{mn\_1} & & & . & & & . \\ & & C_{mN\_1} & & & . & & & . \\ . & & & . & & & C_{M1\_M} \\ . & & & . & & & & C_{Mn\_M} \\ . & & & . & & & & & C_{MN\_M} \end{bmatrix} \tag{A.3}$$

Where $K_j = \sum_{j=1}^N [\cos(\frac{2\pi y_s j}{b}) - 1]$, and $L_j = \sum_{j=1}^N j \cdot \sin(\frac{2 j \pi y_s}{b})$ are constants calculated

from the summation of the $j_{th}$ terms over the y-direction, i.e., the width of the plate.

$[E_{1mn}]$ is an $MN$ by $MN$ diagonal coefficient matrix:

$$[E_{1_{mn}}] = \begin{bmatrix} E_{1_{11}} & & & & & & & \\ & .. & & & & & & \\ & & E_{1_{1n}} & & & & & \\ & & & .. & & & & \\ & & & & E_{1_{mn}} & & & \\ & & & & & E_{1_{mN}} & & \\ & & & & & & .. & \\ & & & & & & & E_{1_{Mn}} \\ & & & & & & & & E_{1_{MN}} \end{bmatrix}$$

(A.4)

Here $E_{1_{mn}}$ is the coefficient term for $W_{mn}$ at the $m_{th}$ and $n_{th}$ order:

$$E_{1_{mn}} = [\frac{bm^4\pi^4}{4a^3} + \frac{an^4\pi^4}{4b^3} + \frac{\upsilon m^2 n^2 \pi^4}{2ab} + \frac{(1-\upsilon)m^2 n^2 \pi^4}{2ab}]D$$

(A.5)

$[E_{2_{mn}}]_s$ is an $MN$ by $MN$ coefficient matrix along $y = y_s$:

$$[E_{2_{mn}}]_s = \begin{bmatrix} E_{2_{11\_1}} & E_{2_{11\_j}} & E_{2_{11\_N}} & & & & & & \\ E_{2_{1n\_1}} & E_{2_{1n\_j}} & E_{2_{1n\_N}} & & & & & & \\ E_{2_{1N\_1}} & E_{2_{1N\_j}} & E_{2_{1N\_N}} & & & & & & \\ & & & E_{2_{m1\_1}} & E_{2_{m1\_j}} & E_{2_{m1\_N}} & & & \\ & & & E_{2_{mn\_1}} & E_{2_{mn\_j}} & E_{2_{mn\_N}} & & & \\ & & & E_{2_{mN\_1}} & E_{2_{mN\_n}} & E_{2_{mN\_N}} & & & \\ & & & & & & E_{2_{M1\_1}} & E_{2_{M1\_j}} & E_{2_{M1\_N}} \\ & & & & & & E_{2_{Mn\_1}} & E_{2_{Mn\_j}} & E_{2_{Mn\_N}} \\ & & & & & & E_{2_{MN\_1}} & E_{2_{MN\_j}} & E_{2_{MN\_N}} \end{bmatrix}_s$$

(A.6)

$$E_{2_{mn\_j}s} = \frac{m^4\pi^4}{2a^3}EI_{ex}\sin(\frac{\pi n y_s}{b})\sin(\frac{\pi j y_s}{b}) + \frac{m^2 nj\pi^4}{2ab^2}GJ_x\cos(\frac{n\pi y_s}{b})\cos(\frac{j\pi y_s}{b})$$

(A.7)

$[E_{3mn}]_s$ is an *MN* by *MN* coefficient matrix along $x = x_s$:

$$[E_{3_{mn}}]_s = \begin{bmatrix} E_{3_{11\_1}} & & E_{3_{11\_m}} & & E_{3_{11\_M}} & \\ & E_{3_{1n\_1}} & & E_{3_{1n\_m}} & & E_{3_{1n\_M}} \\ & & E_{3_{1N\_1}} & & E_{3_{1N\_m}} & & E_{3_{1N\_N}} \\ E_{3_{m1\_1}} & & E_{3_{m1\_m}} & & E_{3_{m1\_M}} & \\ & E_{3_{mn\_1}} & & E_{3_{mn\_m}} & & E_{3_{mn\_M}} \\ & & E_{3_{mN\_1}} & & E_{3_{mn\_m}} & & E_{3_{mn\_M}} \\ E_{3_{M1\_1}} & & E_{3_{M1\_m}} & & E_{3_{M1\_M}} & \\ & E_{3_{Mn\_1}} & & E_{3_{Mn\_m}} & & E_{3_{Mn\_M}} \\ & & E_{3_{MN\_1}} & & E_{3_{MN\_m}} & & E_{3_{MN\_M}} \end{bmatrix} \tag{A.8}$$

$$E_{3_{mn\_i}\,s} = \left[ \frac{n^4\pi^4}{2b^3} EI_{ey} \sin(\frac{m\pi x_s}{a}) \sin(\frac{i\pi x_s}{a}) + \frac{mn^2 i\,\pi^4}{2a^2 b} GJ_y \cos(\frac{m\pi x_s}{a}) \cos(\frac{i\pi x_s}{a}) \right] \tag{A.9}$$

$[E_{4mn}]_s$ is an *MN* by *MN* coefficient matrix along $y = y_s$:

$$[E_{4_{mn}}]_s = \begin{bmatrix} E_{4_{11\_11}} & .. & E_{4_{11\_1N}} & E_{4_{11\_m1}} & .. & E_{4_{11\_mN}} & E_{4_{11\_M1}} & .. & E_{4_{11\_MN}} \\ .. & .. & .. & .. & .. & .. & .. & .. & .. \\ E_{4_{1N\_11}} & .. & E_{4_{1N\_1N}} & E_{4_{1N\_m1}} & .. & E_{4_{1N\_mN}} & E_{4_{1N\_M1}} & .. & E_{4_{1N\_MN}} \\ E_{4_{m1\_11}} & .. & E_{4_{m1\_1N}} & E_{4_{m1\_m1}} & .. & E_{4_{m1\_mN}} & E_{4_{m1\_M1}} & .. & E_{4_{m1\_MN}} \\ .. & .. & .. & .. & .. & .. & .. & .. & .. \\ E_{4_{mN\_11}} & .. & .. & .. & .. & .. & .. & .. & E_{4_{mN\_MN}} \\ .. & .. & .. & .. & .. & .. & .. & .. & .. \\ .. & .. & .. & .. & .. & .. & .. & .. & .. \\ E_{4_{MN\_11}} & .. & E_{4_{MN\_1N}} & E_{4_{MN\_m1}} & .. & E_{4_{MN\_mN}} & E_{4_{MN\_M1}} & .. & E_{4_{MN\_MN}} \end{bmatrix} \tag{A.10}$$

$$E_{4_{mn\_ij}\,s} = (h_{sx} + h_p) EA_{sx} \frac{im^3\pi^2}{a^2(m^2 - i^2)} \sin(\frac{j\pi y_s}{b}) \sin(\frac{n\pi y_s}{b}) \tag{A.11}$$

$[E_{5mn}]_s$ is an *MN* by *MN* coefficient matrix along $x = x_s$:

$$[E_{5_{mn}}]_s = \begin{bmatrix} E_{5_{11\_11}} & .. & E_{5_{11\_1N}} & E_{5_{11\_m1}} & .. & E_{5_{11\_mN}} & E_{5_{11\_M1}} & .. & E_{5_{11\_MN}} \\ .. & .. & .. & .. & .. & .. & .. & .. & .. \\ E_{5_{1N\_11}} & .. & E_{5_{1N\_1N}} & E_{5_{1N\_m1}} & .. & E_{5_{1N\_mN}} & E_{5_{1N\_M1}} & .. & E_{5_{1N\_MN}} \\ E_{5_{m1\_11}} & .. & E_{5_{m1\_1N}} & E_{5_{m1\_m1}} & .. & E_{5_{m1\_mN}} & E_{5_{m1\_M1}} & .. & E_{5_{m1\_MN}} \\ .. & .. & .. & .. & .. & .. & .. & .. & .. \\ E_{5_{mN\_11}} & .. & & .. & .. & .. & .. & .. & E_{5_{mN\_MN}} \\ .. & .. & .. & .. & .. & .. & .. & .. & .. \\ .. & .. & .. & .. & .. & .. & .. & .. & .. \\ E_{5_{MN\_11}} & .. & E_{5_{MN\_1N}} & E_{5_{MN\_m1}} & .. & E_{5_{MN\_mN}} & E_{5_{MN\_M1}} & .. & E_{5_{MN\_MN}} \end{bmatrix} \qquad (A.12)$$

$$E_{5_{mn\_ij}s} = (h_{sy} + h_p)EA_{sy}\frac{jn^3\pi^2}{b^2(n^2 - j^2)}\sin(\frac{i\pi x_s}{a})\sin(\frac{m\pi x_s}{a}) \qquad (A.13)$$

Coefficient matrix $[CX_{1mn}]$, $[CX_{2mn}]$, $[CX_{3mn}]_s$, $[CX_{4mn}]_s$ are in the followings expressions. $[CX_{1mn}]$ is an $MN$ by $MN$ diagonal coefficient matrix:

$$[CX_{1_{mn}}] = \begin{bmatrix} CX_{1_{11}} & & & & & & & \\ & .. & & & & & & \\ & & CX_{1_{1n}} & & & & & \\ & & & .. & & & & \\ & & & & CX_{1_{mn}} & & & \\ & & & & & CX_{1_{mN}} & & \\ & & & & & & .. & \\ & & & & & & & CX_{1_{Mn}} & \\ & & & & & & & & CX_{1_{MN}} \end{bmatrix} \qquad (A.14)$$

where $CX_{1mn}$ is the coefficient term for $A_{mn}$ at the $m_{th}$ and $n_{th}$ order:

$$CX_{1_{mn}} = [\frac{Cm^2\pi^2 b}{4a} + \frac{C(1-v)n^2\pi^2 a}{8b}] \qquad (A.15)$$

$\left[CX_{2mn}\right]$ is an $MN$ by $MN$ coefficient matrix:

$$[CX_{2_{mn}}] = \begin{bmatrix} CX_{2_{11\_11}} & .. & CX_{2_{11\_1N}} & CX_{2_{11\_m1}} & .. & CX_{2_{11\_mN}} & CX_{2_{11\_M1}} & .. & CX_{2_{11\_MN}} \\ .. & .. & .. & .. & .. & .. & .. & .. & .. \\ CX_{2_{1N\_11}} & .. & CX_{2_{1N\_1N}} & CX_{2_{1N\_m1}} & .. & CX_{2_{1N\_mN}} & CX_{2_{1N\_M1}} & .. & CX_{2_{1N\_MN}} \\ CX_{2_{m1\_11}} & .. & CX_{2_{m1\_1N}} & CX_{2_{m1\_m1}} & .. & CX_{2_{m1\_mN}} & CX_{2_{m1\_M1}} & .. & CX_{2_{m1\_MN}} \\ .. & .. & .. & .. & .. & .. & .. & .. & .. \\ CX_{2_{mN\_11}} & .. & .. & .. & .. & .. & .. & .. & CX_{2_{mN\_MN}} \\ .. & .. & .. & .. & .. & .. & .. & .. & .. \\ .. & .. & .. & .. & .. & .. & .. & .. & .. \\ CX_{2_{MN\_11}} & .. & CX_{2_{MN\_1N}} & CX_{2_{MN\_m1}} & .. & CX_{2_{MN\_mN}} & CX_{2_{MN\_M1}} & .. & CX_{2_{MN\_MN}} \end{bmatrix} \tag{A.16}$$

$$CX_{2_{mn\_ij}\,s} = \frac{2mnijC(1+v)}{(m^2-i^2)(j^2-n^2)} \tag{A.17}$$

$\left[CX_{3mn}\right]_s$ is an $MN$ by $MN$ coefficient matrix along $y = y_s$:

$$[CX_{3_{mn}}]_s = \begin{bmatrix} CX_{3_{11\_1}} & CX_{3_{11\_j}} & CX_{3_{11\_N}} & & & & & & \\ CX_{3_{1n\_1}} & CX_{3_{1n\_j}} & CX_{3_{1n\_N}} & & & & & & \\ CX_{3_{1N\_1}} & CX_{3_{1N\_j}} & CX_{3_{1N\_N}} & & & & & & \\ & & & CX_{3_{m1\_1}} & CX_{3_{m1\_j}} & CX_{3_{m1\_N}} & & & \\ & & & CX_{3_{mn\_1}} & CX_{3_{mn\_j}} & CX_{3_{mn\_N}} & & & \\ & & & CX_{3_{mN\_1}} & CX_{3_{mN\_n}} & CX_{3_{mN\_N}} & & & \\ & & & & & & CX_{3_{M1\_1}} & CX_{3_{M1\_j}} & CX_{3_{M1\_N}} \\ & & & & & & CX_{3_{Mn\_1}} & CX_{3_{Mn\_j}} & CX_{3_{Mn\_N}} \\ & & & & & & CX_{3_{MN\_1}} & CX_{3_{MN\_j}} & CX_{3_{MN\_N}} \end{bmatrix}_s \tag{A.18}$$

$$CX_{3_{mn\_j}\,s} = \frac{m^2\pi^2}{2a} EA_{sx} \sin(\frac{n\pi y_s}{b})\sin(\frac{j\pi y_s}{b}) \tag{A.19}$$

$\left[CX_{4mn}\right]_s$ is an $MN$ by $MN$ coefficient matrix along $y = y_s$:

$$[CX_{4_{mn}}]_s = \begin{bmatrix} CX_{4_{11\_11}} & .. & CX_{4_{11\_1N}} & CX_{4_{11\_m1}} & .. & CX_{4_{11\_mN}} & CX_{4_{11\_M1}} & .. & CX_{4_{11\_MN}} \\ .. & .. & .. & .. & .. & .. & .. & .. & .. \\ CX_{4_{1N\_11}} & .. & CX_{4_{1N\_1N}} & CX_{4_{1N\_m1}} & .. & CX_{4_{1N\_mN}} & CX_{4_{1N\_M1}} & .. & CX_{4_{1N\_MN}} \\ CX_{4_{m1\_11}} & .. & CX_{4_{m1\_1N}} & CX_{4_{m1\_m1}} & .. & CX_{4_{m1\_mN}} & CX_{4_{m1\_M1}} & .. & CX_{4_{m1\_MN}} \\ .. & .. & .. & .. & .. & .. & .. & .. & .. \\ CX_{4_{mN\_11}} & .. & .. & .. & .. & .. & .. & .. & CX_{4_{mN\_MN}} \\ .. & .. & .. & .. & .. & .. & .. & .. & .. \\ .. & .. & .. & .. & .. & .. & .. & .. & .. \\ CX_{4_{MN\_11}} & .. & CX_{4_{MN\_1N}} & CX_{4_{MN\_m1}} & .. & CX_{4_{MN\_mN}} & CX_{4_{MN\_M1}} & .. & CX_{4_{MN\_MN}} \end{bmatrix} \qquad (A.20)$$

$$CX_{4_{mn\_ij}s} = (h_{sy} + h_p)EA_{sy}\frac{nj^3\pi^2}{b^2(j^2-n^2)}\sin(\frac{m\pi x_s}{a})\sin(\frac{i\pi x_s}{a}) \qquad (A.21)$$

Coefficient matrix $[CY_{1_{mn}}]$, $[CY_{2_{mn}}]$, $[CY_{3_{mn}}]_s$, $[CY_{4_{mn}}]_s$ are in the followings

expressions. $[CY_{1_{mn}}]$ is an $MN$ by $MN$ diagonal coefficient matrix:

$$[CY_{1_{mn}}] = \begin{bmatrix} CY_{1_{11}} & & & & & & & \\ & .. & & & & & & \\ & & CY_{1_{1n}} & & & & & \\ & & & .. & & & & \\ & & & & CY_{1_{mn}} & & & \\ & & & & & CY_{1_{mN}} & & \\ & & & & & & .. & \\ & & & & & & & CY_{1_{Mn}} & \\ & & & & & & & & CY_{1_{MN}} \end{bmatrix} \qquad (A.22)$$

where $CY_{1_{mn}}$ is the coefficient term for $B_{mn}$ at the $m_{th}$ and $n_{th}$ order:

$$CY_{1_{mn}} = [\frac{Cn^2\pi^2 a}{4b} + \frac{C(1-v)m^2\pi^2 b}{8a}] \qquad (A.23)$$

$[CY_{2_{mn}}]$ is an $MN$ by $MN$ coefficient matrix:

$$[CY_{2_{mn}}] = \begin{bmatrix} CY_{2_{11\_11}} & .. & CY_{2_{11\_1N}} & CY_{2_{11\_m1}} & .. & CY_{2_{11\_mN}} & CY_{2_{11\_M1}} & .. & CY_{2_{11\_MN}} \\ .. & .. & .. & .. & .. & .. & .. & .. & .. \\ CY_{2_{1N\_11}} & .. & CY_{2_{1N\_1N}} & CY_{2_{1N\_m1}} & .. & CY_{2_{1N\_mN}} & CY_{2_{1N\_M1}} & .. & CY_{2_{1N\_MN}} \\ CY_{2_{m1\_11}} & .. & CY_{2_{m1\_1N}} & CY_{2_{m1\_m1}} & .. & CY_{2_{m1\_mN}} & CY_{2_{m1\_M1}} & .. & CY_{2_{m1\_MN}} \\ .. & .. & .. & .. & .. & .. & .. & .. & .. \\ CY_{2_{mN\_11}} & .. & .. & .. & .. & .. & .. & .. & CY_{2_{mN\_MN}} \\ .. & .. & .. & .. & .. & .. & .. & .. & .. \\ .. & .. & .. & .. & .. & .. & .. & .. & .. \\ CY_{2_{MN\_11}} & .. & CY_{2_{MN\_1N}} & CY_{2_{MN\_m1}} & .. & CY_{2_{MN\_mN}} & CY_{2_{MN\_M1}} & .. & CY_{2_{MN\_MN}} \end{bmatrix}$$

(A.24)

$$CY_{2_{mn\_ij}\,s} = \frac{2mnijC(1+v)}{(m^2 - i^2)(j^2 - n^2)}$$

(A.25)

$[CY_{3_{mn}}]_s$ is an $MN$ by $MN$ coefficient matrix along $x = x_s$:

$$[CX_{3_{mn}}]_s = \begin{bmatrix} CX_{3_{11\_1}} & & & CX_{3_{11\_m}} & & & CX_{3_{11\_M}} & & \\ & CX_{3_{1n\_1}} & & & CX_{3_{1n\_m}} & & & CX_{3_{1n\_M}} & \\ & & CX_{3_{1N\_1}} & & & CX_{3_{1N\_m}} & & & CX_{3_{1N\_N}} \\ CX_{3_{m1\_1}} & & & CX_{3_{m1\_m}} & & & CX_{3_{m1\_M}} & & \\ & CX_{3_{mn\_1}} & & & CX_{3_{mn\_m}} & & & CX_{3_{mn\_M}} & \\ & & CX_{3_{mN\_1}} & & & CX_{3_{mn\_m}} & & & CX_{3_{mn\_M}} \\ CX_{3_{M1\_1}} & & & CX_{3_{M1\_m}} & & & CX_{3_{M1\_M}} & & \\ & CX_{3_{Mn\_1}} & & & CX_{3_{Mn\_m}} & & & CX_{3_{Mn\_M}} & \\ & & CX_{3_{MN\_1}} & & & CX_{3_{MN\_m}} & & & CX_{3_{MN\_M}} \end{bmatrix}$$

(A.26)

$$CY_{3_{mn\_i}\,s} = \frac{n^2 \pi^2}{2b} EA_{sy} \sin(\frac{m\pi x_s}{a}) \sin(\frac{i\pi x_s}{a})$$

(A.27)

$[CY_{4_{mn}}]_s$ is an $MN$ by $MN$ coefficient matrix along $x = x_s$:

106

$$[CY_{4_{mn}}]_s = \begin{bmatrix} CY_{4_{11\_11}} & .. & CY_{4_{11\_1N}} & CY_{4_{11\_m1}} & .. & CY_{4_{11\_mN}} & CY_{4_{11\_M1}} & .. & CY_{4_{11\_MN}} \\ .. & .. & .. & .. & .. & .. & .. & .. & .. \\ CY_{4_{1N\_11}} & .. & CY_{4_{1N\_1N}} & CY_{4_{1N\_m1}} & .. & CY_{4_{1N\_mN}} & CY_{4_{1N\_M1}} & .. & CY_{4_{1N\_MN}} \\ CY_{4_{m1\_11}} & .. & CY_{4_{m1\_1N}} & CY_{4_{m1\_m1}} & .. & CY_{4_{m1\_mN}} & CY_{4_{m1\_M1}} & .. & CY_{4_{m1\_MN}} \\ .. & .. & .. & .. & .. & .. & .. & .. & .. \\ CY_{4_{mN\_11}} & .. & .. & .. & .. & .. & .. & .. & CY_{4_{mN\_MN}} \\ .. & .. & .. & .. & .. & .. & .. & .. & .. \\ .. & .. & .. & .. & .. & .. & .. & .. & .. \\ CY_{4_{MN\_11}} & .. & CY_{4_{MN\_1N}} & CY_{4_{MN\_m1}} & .. & CY_{4_{MN\_mN}} & CY_{4_{MN\_M1}} & .. & CY_{4_{MN\_MN}} \end{bmatrix} \qquad (A.28)$$

$$CX_{4_{mn\_ij}\,s} = (h_{sy} + h_p)EA_{sy}\frac{nj^3\pi^2}{b^2(j^2 - n^2)}\sin(\frac{m\pi x_s}{a})\sin(\frac{i\pi x_s}{a}) \qquad (A.29)$$

# Appendix B IFMS Post-alibration Test Records

Calibration List

B1. Test:  DAQ sanity check

Purpose:  demonstrate ability to acquire data and archive it in a readily accessible place (eg. CTools or Google Drive).

Materials:  DOE-Ice laptop and power cord; DataTaker DAQ system, including wall wart; USB disk and/or external hard drive.

Personnel:  Yuxi Zhang and Roger De Roo

Location:  1124 SRB (current location of DataTaker DAQ).

Task:  connect laptop to DAQ system, command DAQ system from laptop, download data. Set the DAQ RTC to within TBD seconds of real-time.

Success criteria:  data appropriate for open circuit connections downloaded and interpreted.


B2. Task:  DAQ connected to IFMS

Purpose:  connect the DAQ system to the IFMS.

Materials:  DOE-Ice laptop and power cord;  DataTaker DAQ system, including wall wart; IFMS; .

Personnel:  Yuxi Zhang, Roger De Roo, and MHL personnel.

Location:  Marine Hydrodynamic Lab (current location of IFMS).

Task: Bring DAQ to MHL, connect DAQ to IFMS, connect laptop to DAQ system, command DAQ system from laptop, download data.

Success criteria:  data appropriate for no-load IFMS conditions downloaded and interpreted.  DAQ RTC keeping time to within TBD seconds of real-time.

B3. Test:  IFMS data acquisition; DAQ sheltered.

Purpose:  obtain baseline data of IFMS under no-load conditions, with DAQ system in thermally controlled environment and IFMS experiencing diurnal variations.

Materials:  DOE-Ice laptop and power cord;  DataTaker DAQ system, including wall wart; IFMS; .

Personnel:  Yuxi Zhang, Roger De Roo, and MHL personnel.

Location:  Marine Hydrodynamic Lab (current location of IFMS).

Task:  connect DAQ to IFMS, with DAQ located indoors.  Run DAQ for at least 72 hours to capture at least 3 diurnal cycles.

Success criteria:  archival of data, including weather conditions.

B4. Test:  IFMS data acquisition; DAQ unsheltered.

Purpose:  obtain baseline data of IFMS under no-load conditions, with both DAQ system and IFMS experiencing diurnal variations.

Materials:  DOE-Ice laptop and power cord;  DataTaker DAQ system, including wall wart and USCG enclosures; IFMS; .

Personnel:  Yuxi Zhang, Roger De Roo, and MHL personnel.

Location:  Marine Hydrodynamic Lab (current location of IFMS).

Task:  connect DAQ to IFMS, with DAQ located outdoors but protected from the elements with USCG enclosure.  Run DAQ for at least 72 hours to capture at least 3 diurnal cycles.

Success criteria:  archival of data, including weather conditions.


B5. Test:  IFMS data acquisition; shielded cable flexed.

Purpose:   obtain baseline data of IFMS under no-load conditions, with the shielded (outdoor component at lighthouse) cables flexed in the middle of the cable.

Materials:  DOE-Ice laptop and power cord;  DataTaker DAQ system, including wall wart and USCG enclosures; IFMS; accurate clock.

Personnel:  Yuxi Zhang, Roger De Roo, and MHL personnel?.

Location:  Marine Hydrodynamic Lab (current location of IFMS).

Task:  capture data at a relatively rapid rate, flexing the shielded cables one by one (first left , then middle, last right) at a location distant from other system features (such as connectors). Carefully record activities including real-time of events.

Success criteria:  archival of data, including notes.

B6. Test:  IFMS data acquisition; DAQ cable flexed.

Purpose:  obtain baseline data of IFMS under no-load conditions, with the cables b/t connectors and DAQ system flexed in the middle of the cable.

Materials:  DOE-Ice laptop and power cord;  DataTaker DAQ system, including wall wart and USCG enclosures; IFMS; accurate clock.

Personnel:  Yuxi Zhang, Roger De Roo, and MHL personnel?.

Location:  Marine Hydrodynamic Lab (current location of IFMS).

Task:  capture data at a relatively rapid rate, flexing the cables one by one (first left , then middle, last right) at a location distant from other system features (such as connectors).  Carefully record activities including real-time of events.

Success criteria:  archival of data, including notes.


B7. Test:  IFMS data acquisition; circular connectors strained mechanically.

Purpose:  obtain baseline data of IFMS under no-load conditions, with the military connectors between the DAQ and IFMS mechanically stressed.

Materials:  DOE-Ice laptop and power cord;  DataTaker DAQ system, including wall wart and USCG enclosures; IFMS; accurate clock.

Personnel:  Yuxi Zhang, Roger De Roo, and MHL personnel?.

Location:  Marine Hydrodynamic Lab (current location of IFMS).

Task:  capture data at a relatively rapid rate, flexing the cables one by one (first left , then middle, last right) at the circular connectors.  Carefully record activities including real-time of events.

Success criteria:  archival of data, including notes.

B8. Test:  IFMS data acquisition; circular connectors strained thermally.

Purpose:   obtain baseline data of IFMS under no-load conditions, with the military connectors between the DAQ and IFMS thermally stressed.

Materials:  DOE-Ice laptop and power cord;  DataTaker DAQ system, including wall wart and USCG enclosures; IFMS; accurate clock; compressed air canister.

Personnel:  Yuxi Zhang, Roger De Roo, and MHL personnel?.

Location:  Marine Hydrodynamic Lab (current location of IFMS).

Task:  capture data at a relatively rapid rate, spraying compressed air on the cable circular connectors one by one (first left , then middle, last right).  Carefully record activities including real-time of events.

Success criteria:  archival of data, including notes.

B9. Test:  IFMS data acquisition; DAQ strained thermally.

Purpose:  obtain baseline data of IFMS under no-load conditions, with the connectors at the DAQ and the DAQ itself thermally stressed.

Materials:  DOE-Ice laptop and power cord;  DataTaker DAQ system, including wall wart and USCG enclosures; IFMS; accurate clock; compressed air canister.

Personnel:  Yuxi Zhang, Roger De Roo, and MHL personnel?.

Location:  Marine Hydrodynamic Lab (current location of IFMS).

Task:  capture data at a relatively rapid rate, spraying compressed air on the connections at the DAQ system.  Carefully record activities including real-time of events.

Success criteria:  archival of data, including notes.


B10. Test:  IFMS data acquisition; circular connectors moistened.

Purpose:  obtain baseline data of IFMS under no-load conditions, with the military circular connectors moistened.

Materials:  DOE-Ice laptop and power cord;  DataTaker DAQ system, including wall wart and USCG enclosures; IFMS; accurate clock; water spray bottle.

Personnel:  Yuxi Zhang, Roger De Roo, and MHL personnel?.

Location:  Marine Hydrodynamic Lab (current location of IFMS).

Task:  capture data at a relatively rapid rate, spraying water on the connections at the DAQ system.  Carefully record activities including real-time of events.

Success criteria:  archival of data, including notes.


B11. Test:  IFMS data acquisition; DAQ moistened.

Purpose: obtain baseline data of IFMS under no-load conditions, with the connectors at the DAQ and the DAQ itself moistened.

Materials: DOE-Ice laptop and power cord; DataTaker DAQ system, including wall wart and USCG enclosures; IFMS; accurate clock; water spray bottle.

Personnel: Yuxi Zhang, Roger De Roo, and MHL personnel?.

Location: Marine Hydrodynamic Lab (current location of IFMS).

Task: capture data at a relatively rapid rate, spraying water on the connections at the DAQ system. Carefully record activities including real-time of events.

Success criteria: archival of data, including notes.


B12. Task: cable moving in and out; check the cable inlet with mirror and flash lights.

Purpose: evaluate the effect zero strain gauge located on the upper bracket of the L-metal; give a first estimation of the condition of the cables from the inlet of the upper plate.

Materials: IFMS plate, cables, gloves and mirror and flash lights.

Personnel: Yuxi Zhang, RdR.

Location: MHL

Task: move cables in and out wtr to the inlet of the cables on the IFMS plate, check the appearance of incoming cables by the mirror with a flash light.

Success criteria: zero strain gauge reading is not affected much compared to its regular variations in calm state; good condition of observation of the cable inside.

# BIBLIOGRAPHY

[1]     Andrews, H., & Patterson, C. (1976). Singular value decompositions and digital image processing. IEEE Transactions on Acoustics, Speech, and Signal Processing, 24(1), 26-53.

[2]     Andrieux, S., & Abda, A. B. (1996). Identification of planar cracks by complete overdetermined data: inversion formulae. Inverse problems, 12(5), 553.

[3]     Barik, M., & Mukhopadhyay, M. (2002). A new stiffened plate element for the analysis of arbitrary plates. Thin-Walled Structures, 40(7), 625-639.

[4]     Bhaskar, K., & Kaushik, B. (2004). Simple and exact series solutions for flexure of orthotropic rectangular plates with any combination of clamped and simply supported edges. Composite Structures, 63(1), 63-68.

[5]     Bjerkås, M., & Skiple, A. (2005). "Occurrence of continuous and intermittent crushing during ice-structure interaction." Proceedings of the 18th International Conference of Port and Ocean Engineering under Arctic Conditions (POAC), Potsdam, USA (Vol. 3).

[6]     Bjerkås, M. (2006). Ice Actions on Offshore Structures–With Applications of Continuous Wavelet Transforms on Ice Load Signals.

[7]     Bjerkås, M. (2007). "Review of Measured Full Scale Ice Forces to Fixed Structures." Proceedings of the 26th International Conference on Offshore Mechanics and Arctic Engineering, San Diego, California, USA. OMAE2007-29048.

[8]     Bjerkås, M., Albrektsen, A., & Gürtner, A. (2010, January). Static and dynamic ice actions in the light of new design codes. In ASME 2010 29th International Conference on Ocean, Offshore and Arctic Engineering (pp. 733-739). American Society of Mechanical Engineers.

[9]     Bonnet, M., & Constantinescu, A. (2005). "Inverse problems in elasticity." Inverse problems, 21(2), R1.

[10]    Boot, J. C., & Moore, D. B. (1988). "Stiffened plates subject to transverse loading." International journal of solids and structures, 24(1), 89-104.

[11]    Croasdale, K. R., Morgenstern, N. R., & Nuttall, J. B. (1977). Indentation tests to investigate ice pressures on vertical piers. Journal of Glaciology, 19(81), 301-312.

115

[12]    Chock, J. and R. Kapania (2003). "Load Updating for Finite Element Models". AIAA Journal 41 (9), 1667–1673.

[13]    Choi, Y. S., & Noah, S. T. (1988). Forced periodic vibration of unsymmetric piecewise-linear systems. Journal of Sound and Vibration, 121(1), 117-126.

[14]    Deb, A., and Booton, M. (1988). "Finite element models for stiffened plates under transverse loading." Computers & Structures, 28(3), 361-372.

[15]    Deb, A., Deb, M., & Booton, M. (1991). "Analysis of orthotropically modeled stiffened plates." International Journal of Solids and Structures, 27(5), 647-664.

[16]    Dempsey, J. P. (2000). Research trends in ice mechanics. International journal of solids and structures, 37(1-2), 131-153

[17]    Dempsey, J. P., Palmer, A. C., & Sodhi, D. S. (2001). High pressure zone formation during compressive ice failure. Engineering fracture mechanics, 68(17), 1961-1974.

[18]    Dickinson, S. M. (1969, March). The flexural vibration of rectangular orthotropic plates. Journal of Applied Mechanics, 36(1), 101-106.

[19]    Egle, D. M., & Sewall, J. L. (1968). An analysis of free vibration of orthogonally stiffened cylindrical shells with stiffeners treated as discrete elements. AIAA Journal, 6(3), 518-526.

[20]    Engl, H. W., & Kügler, P. (2005). "Nonlinear inverse problems: theoretical aspects and some industrial applications." In Multidisciplinary methods for analysis optimization and control of complex systems (pp. 3-47). Springer Berlin Heidelberg.

[21]    Ewing, R. E., Lin, T., & Lin, Y. (1999). A mixed least-squares method for an inverse problem of a nonlinear beam Eq.. Inverse Problems, 15(1), 19.

[22]    Efimtsov, B. M., & Lazarev, L. A. (2009). Forced vibrations of plates and cylindrical shells with regular orthogonal system of stiffeners. Journal of Sound and Vibration, 327(1), 41-54.

[23]    Foster, J., & Richards, F. B. (1991). The Gibbs phenomenon for piecewise-linear approximation. The American Mathematical   Monthly, 98(1), 47-49.

[24]    Frederking, R., & Schwarz, J. (1982). Model tests of ice forces on fixed and oscillating cones. Cold Regions Science and Technology, 6(1), 61-72.

[25]    FSICR 2010. Finnish- Swedish Ice lass Rules 2010. Transport Safety Agency, Helsinki, Finland. TRAFI/31298/03.04.01.00/2010.

[26]     Green, A. E. (1944). Double Fourier series and boundary value problems. In Mathematical Proceedings of the Cambridge Philosophical Society (Vol. 40, No. 03, pp. 222-228), Cambridge University Press, Cambridge, UK.

[27]     Gagnon, R. E. (2012). An explanation for the Molikpaq May 12, 1986 event. Cold Regions Science and Technology, 82, 75-93.

[28]     Hansen, P. C. (1987). "The truncated svd as a method for regularization." BIT Numerical Mathematics, 27(4), 534-553.

[29]     Hansen, P. C., & O'Leary, D. P. (1993). "The use of the L-curve in the regularization of discrete ill-posed problems." SIAM Journal on Scientific Computing, 14(6), 1487-1503.

[30]     Hewitt, E., & Hewitt, R. E. (1979). The Gibbs-Wilbraham phenomenon: an episode in Fourier analysis. Archive for history of Exact Sciences, 21(2), 129-160.

[31]     Hoppman, H. W., Huffington, N. J., & Magness, L. S. (1956). A study of orthogonally stiffened plates. ASME Trans. J. Appl. Mech, 23, 243-250.

[32]     Huang, G., & Liu, P. (2009). A dynamic model for ice-induced vibration of structures. Journal of Offshore Mechanics and Arctic Engineering, 131(1), 011501.

[33]     Huang, Y., Shi, Q., & Song, A. (2007). Model test study of the interaction between ice and a compliant vertical narrow structure. Cold Regions Science and Technology, 49(2), 151-160.

[34]     International Electrotechnical Commission. (2009). IEC 61400-3-1. Wind Turbines-Part, 3-1: Design Requirement for Offshore Wind Turbines.

[35]     International Association of Classification Societies. Structural Requirements for Polar Class Ships IACS Req. 2006/Rev.2, 2010

[36]     Jerri, A. J. (2013). The Gibbs phenomenon in Fourier analysis, splines and wavelet approximations (Vol. 446). Springer Science & Business Media.

[37]     Ji, X., & Oterkus, E. (2016, October). A novel dynamic ice-structure interaction model for ice-induced vibrations. In Techno-Ocean (Techno-Ocean) (pp. 70-73). IEEE.

[38]     Jordaan, I. J. (2001). Mechanics of ice–structure interaction. Engineering Fracture Mechanics, 68(17), 1923-1960.

[39]     Joensuu, A., & Riska, K. (1989). Contact between ice and structure. Laboratory of Naval Architecture and Marine Engineering, Helsinki University of Technology, Espoo, Finland, Report M-88.

[40]    Jonkman, J. M. (2009). Dynamics of offshore floating wind turbines—model development and verification. Wind energy, 12(5), 459-492.

[41]    Kaiman, D. (1996). "A singularly valuable decomposition." College Mathematics Journal, 27(1), 2-23.

[42]    Kaldasaun, J., & Kujala, P. (2011). Risk-Based Approach for Structural Design of Ice-Strengthened Vessels Navigating in the Baltic Sea. In Proceedings of the International Conference on Port and Ocean Engineering Under Arctic Conditions (No. POAC11-093).

[43]    Kärnä, T., & Turunen, R. (1989). Dynamic response of narrow structures to ice crushing. Cold Regions Science and Technology, 17(2), 173-187.

[44]    Kärnä, T., Gravesen, H., Fransson, L., & Løset, S. (2010). Simulation of multi-modal vibrations due to ice actions. In Proceedings of the 20th International Symposium on Ice (IAHR). Lahti, Finland (Vol. 1).

[45]    Kärnä, T., Qu, Y., Bi, X., Yue, Q., & Kuehnlein, W. (2007). A spectral model for forces due to ice crushing. Journal of offshore mechanics and Arctic engineering, 129(2), 138-145.

[46]    Karr, D. G., Troesch, A. W., & Wingate, W. C. (1993). Nonlinear dynamic response of a simple ice-structure interaction model. Journal of Offshore Mechanics and Arctic Engineering, 115(4), 246-252.

[47]    Kim, E., & Amdahl, J. (2016). Discussion of assumptions behind rule-based ice loads due to crushing. Ocean Engineering, 119, 249-261.

[48]    Kim, L. V., Kulesh, V. A., & Tsuprik, V. G. (2015). Methodology for Experimental Determination of Local Ice Pressures on Flexible Hull of Platforms and Ships. In The Twenty-fifth International Offshore and Polar Engineering Conference. International Society of Offshore and Polar Engineers.

[49]    Leira, B., Børsheim, L., Espeland, Ø., & Amdahl, J. (2009). Ice-load estimation for a ship hull based on continuous response monitoring. Proceedings of the Institution of Mechanical Engineers, Part M: Journal of Engineering for the Maritime Environment, 223(4), 529-540.

[50]    Leone, G., & Soldovieri, F. (2003). Analysis of the distorted Born approximation for subsurface reconstruction: truncation and uncertainties effects. IEEE Transactions on Geoscience and Remote Sensing, 41(1), 66-74.

[51]    Li, J., & Kapania, R. K. (2007). "Load updating for nonlinear finite element models." AIAA journal, 45(7), 1444-1458.

[52]     Ma, C. K., Chang, J. M., & Lin, D. C. (2003). "Input forces estimation of beam structures by an inverse method." Journal of soun  d and vibration, 259(2), 387-407.

[53]     Matlock, H., Dawkins, W. P., & Panak, J. J. (1971). Analytical model for ice-structure interaction. Journal of the Engineering Mechanics Division, 97(4), 1083-1092.

[54]     Meleshko, V. V. (1997). Bending of an elastic rectangular clamped plate: Exact versus 'engineering' solutions. Journal of Elasticity, 48(1), 1-50.

[55]     Mouritz, A. P., Gellert, E., Burchill, P., & Challis, K. (2001). Review of advanced composite structures for naval ships and submarines. Composite structures, 53(1), 21-42.

[56]     Mukherjee, A., & Mukhopadhyay, M. (1988). Finite element free vibration of eccentrically stiffened plates. Computers & structures, 30(6), 1303-1317.
[57]     Nejati, H. (2014). Passive Remote Sensing of Lake Ice and Snow using Wideband Autocorrelation Radiometer (WiBAR) (Doctoral dissertation, The University of Michigan).

[58]     Palmer, A. C., Dempsey, J. P., and Masterson, D. M. (2009). "A revised ice pressure-area curve and a fracture mechanics explanation." Cold regions science and technology, 56(2), 73-76.

[59]     Palmer, A., & Croasdale, K. (2013). Arctic offshore engineering. Singapore: World Scientific.

[60]     Qing, G., Qiu, J., & Liu, Y. (2006). Free vibration analysis of stiffened laminated plates. International Journal of Solids and Structures, 43(6), 1357-1371.

[61]     Remmers, Thomas C. "Prediction of Nonlinear Contact Dynamics of an Ice-Structure Interaction Model using Fourier Analysis." Master's thesis, The University of Michigan, 1998.

[62]     Rigo, P. (1992). Stiffened sheathings of orthotropic cylindrical shells. Journal of Structural Engineering, 118(4), 926-943.

[63]     Riska, K. (1991). Observations of the line-like nature of ship-ice contact. In 11th International Conference on Port and Ocean Engineering under Arctic Conditions, Proceedings (Vol. 2, pp. 24-28).

[64]     Riska, K., Uto, S., & Tuhkuri, J. (2002). Pressure distribution and response of multiplate panels under ice loading. Cold Regions Science and Technology, 34(3), 209-225.

[65]     Riska, K., & Kämäräinen, J. (2011, November). A review of ice loading and the evolution of the finnish-swedish ice class rules. In Proceedings of the SNAME Annual Meeting and Expo. November (pp. 16-18).

[66]     Sabodash, O. A. (2015, July). Global Ice Loads on the Sakhalin Offshore Structures: Statistical Overview by Existing Design Codes. In The Twenty-fifth International Ocean and Polar Engineering Conference. International Society of Offshore and Polar Engineers.

[67]     Samanta, A., & Mukhopadhyay, M. (2003). Free vibration analysis of stiffened shells by the finite element technique. European Journal of Mechanics-A/Solids, 23(1), 159-179.

[68]     Sanderson, T. J. O. (1988). "Ice Mechanics. Risks to Offshore Structures." Graham and Trotman, London, 253 p.

[69]     Sanderson, T. J. O. (1991). "Statistical analysis of ice forces." In Ice-Structure Interaction (pp. 439-457). Springer Berlin Heidelberg.Sapountzakis, E. J., & Katsikadelis, J. T. (2001). Analysis of prestressed concrete slab-and-beam structures. Computational mechanics, 27(6), 492-503.

[70]     Semnani, A., & Kamyab, M. (2008). Truncated cosine Fourier series expansion method for solving 2-D inverse scattering problems. Progress In Electromagnetics Research, 81, 73-97.

[71]     Semnani, A., & Kamyab, M. (2010). "Solving Inverse Scattering Problems Using Truncated Cosine Fourier Series Expansion Method." INTECH Open Access Publisher.

[72]     Shi, P. et al., (2015). Free Vibration Analysis of Curvilinearly Stiffened Cylindrical Shells. 56th AIAA/ASCE/AHS/ASC Structures, Structural Dynamics, and Material Conference, Jan 2015, Florida, AIAA, Reston.

[73]     Shimpi, R. P., & Patel, H. G. (2006). "A two variable refined plate theory for orthotropic plate analysis." International Journal of Solids and Structures, 43(22), 6783-6799.

[74]     Snieder, R. (1998). "The role of nonli    unearity in inverse problems." Inverse Problems, 14(3), 387.

[75]     Sodhi, D. S. (1991). "Ice-structure interaction during indentation tests." In Ice-structure interaction (pp. 619-640). Springer Berlin Heidelberg.

[76]     Sodhi, D. S. (2001). Crushing failure during ice–structure interaction. Engineering Fracture Mechanics, 68(17), 1889-1921.

[77]     Srinivas, S., & Rao, A. K. (1970). Bending, vibration and buckling of simply supported thick orthotropic rectangular plates and laminates. International Journal of Solids and Structures, 6(11), 1463-1481.

[78]     Starkey, J. M., & Merrill, G. L. (1989). "On the ill-conditioned nature of indirect force-measurement techniques." Journal of Modal Analysis, 4(3), 103-108.

[79]     Suominen, M., Kujala, P., von Bock und Polach, R., & Kiviranta, J. (2013). Measured ice loads and design ice loads. Analysis and Design of Marine Structures, 119-124.

[80]     Tarp-Johansen, N. J., Manwell, J. F., & McGowan, J. (2006, January). Application of design standards to the design of offshore wind turbines in the US. In Offshore Technology Conference. Offshore Technology Conference.

[81]     Timco, G. W., & Johnston, M. (2003). Ice loads on the Molikpaq in the Canadian Beaufort Sea. Cold Regions Science and Technology, 37(1), 51-68.

[82]     Tõns, T., Ralph, F., Ehlers, S., & Jordaan, I. J. (2015). Probabilistic Design Load Method for the Northern Sea Route. ASME 2015 34th International Conference on Ocean, Offshore and Arctic Engineering. American Society of Mechanical Engineers.

[83]     Ventsel, E., & Krauthammer, T. (2001). "Thin plates and shells: theory: analysis, and applications." Chapter 7.2 in Orthotropic and Stiffened Plates, CRC press.

[84]     Wang, Y., & Wang, Z. (1994). Periodic response of piecewise-linear oscillators using trigonometric collocation. Journal of sound and vibration, 177(4), 573-576.

[85]     Wang, X., & Rammerstorfer, F. G. (1996). Determination of effective breadth and effective width of stiffened plates by finite strip analyses. Thin-walled structures, 26(4), 261-286.

[86]     Ward, J. C., Harwood, C. M., & Young, Y. L. (2018). Inverse method for hydrodynamic load reconstruction on a flexible surface-piercing hydrofoil in multi-phase flow. Journal of Fluids and Structures, 77, 58-79.

[87]     Wells, J., Jordaan, I., Derradji-Aouat, A., & Taylor, R. (2011). Small-scale laboratory experiments on the indentation failure of polycrystalline ice in compression: Main results and pressure distribution. Cold Regions Science and Technology, 65(3), 314-325.

[88]     W. Jiang, A. Bennett, N. Vlahopoulos, M. Castanier, R. Thyagarajan, A Reduced-Order Model for Evaluating the Dynamic Response of Multilayer Plates to Impulsive Loads, SAE Int. Journal of Passenger Cars – Mechanical Systems 2016-01- 0307.

[89]     Wong, C. W., Zhang, W. S., & Lau, S. L. (1991). Periodic forced vibration of unsymmetrical piecewise-linear systems by incremental harmonic balance method. Journal of Sound and Vibration, 149(1), 91-105.

[90]     Xiang, Y., Kitipornchai, S., & Urn, M. K. (1994). Vibration of rectangular Mindlin plates with intermediate stiffeners. Journal of Vibration and Acoustics, 116, 529-535.

[91]     Yu, B. (2014). Offshore Wind Turbine Interaction with Floating Freshwater Ice on the Great Lakes (Doctoral dissertation, The University of Michigan).

[92]     Yue, Q., Guo, F., & Kärnä, T. (2009). Dynamic ice forces of slender vertical structures due
     to ice crushing. Cold Regions Science and Technology, 56(2-3), 77-83.

[93]     Ziemer, G., & Evers, K. U. (2016). Model Tests With a Compliant Cylindrical Structure to
Investigate Ice-Induced Vibrations. Journal of Offshore Mechanics and Arctic Engineering,
138(4), 041501.